SYNTHESIS OF UPCONVERTING NANOPARTICLES FOR TEMPERATURE SENSING APPLICATIONS

by

Gihan Sumith Joshua

A Thesis Submitted to the Faculty of the

BIOMEDICAL ENGINEERING GRADUATE INTERDISCIPLINARY PROGRAM

In Partial Fulfillment of the Requirements
For the Degree of

MASTER OF SCIENCES
WITH A MAJOR IN BIOMEDICAL ENGINEERING

In the Graduate College of

THE UNIVERSITY OF ARIZONA

2012

2012 STATEMENT BY AUTHOR

This thesis has been submitted in partial fulfillment of requirements for an advanced degree at the University of Arizona and is deposited in the University Library to be made available to borrowers under rules of the Library.

Brief quotations from this thesis are allowable without special permission, provided that accurate acknowledgment of source is made. Requests for permission for extended quotation from or reproduction of this manuscript in whole or in part may be granted by the copyright holder.

SIGNED: _____
Gihan Joshua

APPROVAL BY REPORT DIRECTOR

This report has been approved on the date shown below:

_____ 8/7/2012
Dr. Marek Romanowski Date

Acknowledgements

I would like to first thank my advisor, Dr. Marek Romanowski, for helping guide me through this research. His advice not just about my research methods and objectives, but discussion about my graduate career as a whole, plans for the future, among many other topics will always be remembered.

I would like to thank the rest of the members of my thesis committee, Dr. Marty Pagel, Dr. Terry Matsunaga, and Dr. Jeong-Jeol Yoon. I enjoyed the graduate courses that I took that were taught by each of these professors, and they all helped in various ways in bringing this thesis work to a completion.

I would like to thank all the members of our research group, both past and present, including Jacqueline Brauneis, Chris Gainer, Xenia Kachur, Shellie Knights, Sarah Leung, Gabe Orsinger, Saradadevi Thanikachalam, and Joshua Williams. Special mention should be given to Chris Gainer, who I collaborated closely with on the nanoparticle research as well as on a previous publication, as well as Christine Silken, a high school graduate that assisted me with my research during the summer of 2011.

I would like to thank Dr. Anthony Muscat and Pablo Mancheno, a graduate student in his research group. Pablo was instrumental in helping me with my research, by providing me with the functionalized glass slides as well as FTIR characterization, that took no short amount of time, and for that I am grateful. The discussion that I had with him and Dr. Muscat were always very thoughtful and useful, and often times they went out of their way to assist me with this research.

Finally, I would like to thank Dr. Channa de Silva, who originally got me interested in laboratory research and specifically this research involving nanoparticles. Even after he left the University of Arizona and I continued this work, he was very helpful in answering questions I had and discussing my research, and providing me with XRD characterization of the particles on his own time.

Dedication

I dedicate this thesis to Larissa, my parents, and all those who helped me to see this research to completion during the times that I lost sight of the finish line.

TABLE OF CONTENTS

TABLE OF CONTENTS - Continued

TABLE OF CONTENTS - Continued

TABLE OF CONTENTS - Continued

LIST OF FIGURES

LIST OF FIGURES - Continued

LIST OF FIGURES - Continued

LIST OF FIGURES - Continued

LIST OF FIGURES – Continued

LIST OF TABLES

APPENDICES

Abstract

Lanthanide-doped nanoparticles have been increasingly gaining attention as possible contrast agents due to their unique upconversion luminescence properties. The luminescence of certain emission bands from $NaYF_4:Er^{3+}/Yb^{3+}$ nanoparticles are also temperature dependent, and can be used as a ratiometric temperature sensor by monitoring the green-to-red emission ratio. The objective of this study was to reproducibly synthesize $NaYF_4:Er^{3+}/Yb^{3+}$ nanoparticles, use them to create a thin film on a glass surface, and visualize temperature changes on this coated surface. Nanoparticles were prepared via thermal decomposition at 300^{o} C, underwent an acid treatment process to remove the oleate ligands from their surfaces, and were introduced to glass slides that had been functionalized with carboxyl groups. The temperature of the coated glass slide was varied, and images taken using a CCD camera were used to construct the green-to-red emission ratio, which showed a linear trend with respect to increasing temperature.

Section 1

Introduction

1.1 – Origins of Upconverting Materials

The unique process of upconversion luminescence has been researched ever since its discovery back in the 1960s. Auzel and others first investigated this process of upconversion and anti-Stokes emission in bulk materials of rare earth-doped phosphors.[1] The study of bulk upconverting materials paved the way for the eventual discovery of lanthanide-doped nanoparticles that also possessed the same upconversion luminescence properties of their bulk counterparts. While many devices have emerged from the discovery of these bulk materials, such as lasers[2-3] and solar cells[13], materials on the nanoscale could be geared towards applications more relevant to the fields of biology and the emerging field of nanomedicine. Although nanoscale upconverting materials lack the upconversion efficiency seen in the bulk counterparts, their small scale allows for unique properties such as tunability of their emission by size variation, functionalization through surface modification techniques, as well as emerging use as advanced biological labels to replace fluorescent dyes.

1.2 – Process of Upconversion

The term upconversion is characterized by the conversion of long wavelength radiation to short-wavelength radiation, for example from the near infrared range (NIR) to the visible range. Upconversion is a nonlinear optical process, in contrast to linear optics in which the optical properties of a material are assumed to be independent of the

intensity of the incident light. The upconversion process can proceed by different pathways, all of which have been summarized in detail in numerous studies.[1,5,9] The process requires the presence of two or more metastable energy states to store the energy of absorbed pump photons. When the energies of these pump photons are combined, this can lead to the emission of a higher energy photon, hence 'upconversion'.

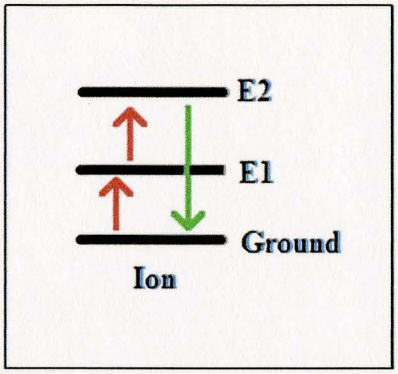

Figure 1: Diagram illustrating excited state absorption (ESA) process. Refer to the following energy levels for resulting discussion of upconversion processes.

There are four basic energy transfer processes that can cause the upconversion phenomenon: excited state absorption (ESA), cross relaxation (CR), energy transfer upconversion (ETU), and photon avalanche (PA).[5] Excited state absorption (ESA) occurs when an ion absorbs a pump photon which moves it to an excited state E1, and then subsequently absorbs another photon which moves the ion to an even higher excited state E2. When the ion returns to the ground state, it gives off radiation with energy corresponding to both excited state transitions (E2→Ground). Cross relaxation (CR) involves two ions that are both initially excited by a pump photon to the E1 state. One ion then transfers energy to the another, resulting in one ion that is moved to the E2 state, and one ground state ion. The ion at the E2 state then returns to the ground state, releasing a

photon. Energy transfer upconversion (ETU) involves three ions, two of which donate energy (referred to as sensitizers), and one of which receives energy and emits radiation (referred to as activators). In this mechanism, the two sensitizer ions absorb pump photons and reach the E1 state, and then both sensitizer ions transfer energy to the activator ion and return to the ground state, which excites the activator from the ground state to the E2 state. The activator then emits a photon and returns to the ground state. This type of energy transfer process between two ions was first characterized by Auzel in 1966.[6] The final process, photon avalanche (PA), is much more complex than the first three processes. During this process, many ions are populated to the E1 state via nonresonant ground state absorption. This population of the E1 state leads to a greater occurrence of ESA events. As the ions in the E1 state are excited to the E2 state and emit photons, energy is transferred to the ground state ions, which are excited to E2 and causes an "avalanche" effect where ions are continually being excited and returning to the ground state, emitting photons. ETU is by far to most efficient upconversion mechanism, because it favors resonant absorption, which leads to long luminescence lifetimes.[5] PA occurs only when incident pump photon intensity reaches a critical threshold, and has been characterized in detail in the literature.[1]

Quenching can occur via many processes and limits the efficiency of the upconversion process. Phonons allow for a competing energy transfer route to radiative emission through multi-phonon transitions to lower energy levels, and therefore ions with closely spaced energy levels are susceptible to quenching.[1] The probability of phonon

quenching decreases as the energy gap between levels increases, as multiple phonons are needed to bridge the same gap as a single photon. Quenching can also occur through radiative emission of lower energy photons, and via cross relaxation to impurities or other lanthanide ions that are present in the material. Because of this, the concentration of dopant ions must be precisely controlled to maintain a high upconversion efficiency. Efficient upconversion processes are only seen when trivalent lanthanide ions are used, due to their extremely long-lived intermediate energy states.

1.3 – Lanthanide-doped Nanoparticles

Upconverting nanoparticles are commonly composed of an inert host material doped with the sensitizer and activator ions. The dopant provides the luminescent centers while the crystal structure of the host lattice provides a matrix to bring these centers into an optimal position.[7-8]

Dopant and host materials must be carefully selected to control the energy transfer mechanisms that elicit the upconversion process. The choice of host lattice determines the distance between dopant ions, their relative spatial position, their coordination numbers, and the type of anions surrounding the dopant.[9] Host materials should be chemically stable, have low phonon energies to avoid energy loss via nonradiative transfer, and be size compatible with the trivalent lanthanide ions. The most popular host materials for these nanoparticles are predominantly $NaYF_4$ and LaF_3. These fluoride materials exhibit long lifetimes of the excited states due to the low phonon energies (ca. 350 cm^{-1}) of the crystal lattice.[10] Materials such as ZrO_2, Y_2O_3,$LuPO_4$, and $YbPO_4$ are

also used but to a lesser extent, due to their larger phonon energies than the fluoride materials. Lanthanide ions are chosen as the dopants in these nanoparticles due to their ladder-like energy levels that allow for metastable storage of pump photon energy.[1] The lanthanide dopants have long-lived energy states that act as energy reservoirs during the upconversion process. Some common ions that are chosen as the activator ions are Erbium (Er^{3+}) and Thulium (Tm^{3+}), due to their large gaps between energy states that deter non-radiative energy transfer. Holmium (Ho^{3+}) has also been used as an activator ion, because it has energy states that are almost evenly spaced, and upconversion occurs mainly through the absorption of multiple photons. To avoid the problem of cross relaxational quenching, which can dramatically lower the efficiency of the upconversion process, large quantities of the sensitizer ions are added to the host material, while the concentration of activator ions is kept relatively low. Ytterbium (Yb^{3+}) is by far one of the most commonly used sensitizer ions, because its energy levels are compatible with the energy level transitions of many lanthanide activator ions, such as Er^{3+}, Tm^{3+}, and Ho^{3+}, and it absorbs radiation in the NIR range very efficiently. The most efficient upconverting phosphor developed so far is $NaYF_4$ doped with Er^{3+} and Yb^{3+}, which was developed by two groups between 1972-1973.[11-12]

1.4 – $NaYF_4:Er^{3+},Yb^{3+}$ Nanoparticles

While the synthetic methods of bulk upconverting materials have been characterized since the 1960s, it has only been recently that techniques have been developed to synthesize the lanthanide-doped nanoparticles. Several methods have been developed for

both fluoride and oxide host materials, and these techniques have been further refined to address such issues such as monodispersity and crystal structure. As noted above, the most efficient upconverting phosphor developed to date has been $NaYF_4:Er^{3+},Yb^{3+}$, and as such there has been an intense focus in developing nanoparticles based on this material.

There have been many synthetic routes proposed to synthesize these nanoparticles including coprecipitation, hydrothermal, sol-gel, combustion, and flame synthesis.[5] One of the most successful and highly used synthetic routes is utilizing thermal decomposition of metal trifluoroacetates at high temperatures. It has been widely established that lanthanide metal trifluoroacetates will thermally decompose to produce the corresponding metal fluorides for this type of nanoparticle synthesis.[32-33] During that decomposition at high temperatures, oleic acid together with 1-ocatedecene, acting as a non-coordinating solvent, work together to yield monodisperse nanoparticles. Adequate synthetic controls must be introduced to avoid oxidation of the lanthanide metal precursors as they decompose, as well as the oleic acid. Additionally, fluorinated and oxyfluorinated carbon compounds are a byproduct of these types of syntheses[32-33], so this synthesis must be performed in a well-ventilated area, preferably a fume hood.

Both cubic-phase and hexagonal-phase $NaYF_4:Er^{3+},Yb^{3+}$ nanoparticles can be synthesized through this method. Hexagonal phase nanoparticles are generally more thermodynamically stable than cubic-phase nanoparticles and have greater upconversion efficiencies, but the synthetic routes often create mixed crystal phases with non-uniform

particle size distributions.[34] In many cases cubic phase nanoparticles must first be synthesized then annealed at high temperatures to convert to hexagonal phase, and often times this process does not proceed to completion.

In contrast, the synthesis of cubic phase nanoparticles can be performed with comparable ease. The Capobianco group has reported a synthesis of cubic phase $NaYF_4$ nanoparticles doped with both Er^{3+}/Yb^{3+} and Tm^{3+}/Yb^{3+}, via thermal decomposition of lanthanide trifluoroacetate precursors in the presence of oleic acid and 1-octadecene[19], which was adapted from an early reported synthesis of monodisperse LaF_3 triangular nanoplates.[35] The synthesized nanoparticles had a monodisperse size distribution, size uniformity, and luminescence emission spectra with sharp emission peaks.

One drawback of these and many types of synthetic methods to create these nanoparticles is that only small amounts (<1 gram), of nanoparticles can be produced per synthesis. This is due to the fact that the amount of lanthanide metal precursors has to be carefully controlled in conjunction with the volume of oleic acid and 1-octadecene, to provide the correct ratio of sensitizer to activator ions so that the upconversion process will occur as efficiently as possible (section 1.3). Efforts to scale up this synthetic process are currently being researched.

There are many advantages that upconverting nanoparticles possess that are advantageous in biological applications when compared to organic dyes or traditional fluorophores. Upconverting nanoparticles are excited in the near-infrared (NIR), range and the excitation source is quite often 980 nm NIR diode lasers. This excitation source is

relatively inexpensive when compared to the high energy pulse lasers that are required for organic dyes and quantum dots. And because the nanoparticles are excited in the NIR range, if used in a medical imaging application, there would be an absence of autofluorescence from tissues. This is due to the fact that living tissue has relatively low photon absorption in the NIR range (700-1000 nm) of the electromagnetic spectrum. This in turn leads to decreased light scattering when using upconverting nanoparticles, with high image contrast and sharp emission peaks present in the emission spectra. This also allows for deep light penetration into tissue, without phototoxicity or photobleaching occurring.

1.5 – Nanoparticle Coating and Functionalization Methods

One of the main drawbacks of many of the current synthetic methods for lanthanide-doped nanoparticles is the fact that after the synthesis has been completed, the nanoparticle surfaces are coated with ligands, often times being oleate ligands. [20-23] There are two main drawbacks to this surface ligand. First, because the oleate is bound to the surface of the nanoparticle through interaction between its carboxyl group and the trivalent lanthanide ions on the nanoparticle surfaces, its long hydrocarbon chain is protruding outwards. This renders the nanoparticles water-insoluble and they cannot be dispersed in polar media, which poses obvious drawbacks for use in biomedical applications. Secondly, the oleate coating has no functional groups that could be used for the conjugation of biomolecules, and thus limits the nanoparticles ability to be used in

applications such as targeted delivery studies. Therefore, surface modification is necessary for the implementation of these nanoparticles in biological applications.

To compensate for this oleate coating on the nanoparticles, a large variety of surface modification techniques have been proposed. One simple method that was proposed involves the use of β-cyclodextrin, to "draw" the nanoparticles into the water phase from the non-polar phase.[24] The cyclodextrin rings form a complex with the oleate ligand, with the oleate ligand associating with the relatively hydrophobic interior of the ring, while the hydrophilic exterior helps drive the nanoparticles into the aqueous phase. This has also been shown previously using oleate-stabilized iron oxide nanoparticles.[25]

Another popular method is to use a ligand exchange procedure, in which the oleate ligand on the nanoparticle surfaces is switched for one that is more water-soluble and that may have functional groups. The van Veggel group has shown many novel ligand-exchange strategy to replace the oleate ligand, such as polyvinylpyrrolidone (PVP) and PEG-phosphate[26-27]. The Haase group has also shown methods of ligand exchange using 1-hydroxyethane-1,1-diphosphonic acid (HEDP), and then subsequent silica coating that renders nanoparticles water-soluble with high colloidal stability demonstrated.[30]

Yet another popular method has been to coat the nanoparticles entirely with a shell of SiO_2 prepared via a sol-gel process, which many groups have produced with variable success.[28-30] Post-surface modification of the silica coating can be performed to attach functional groups, such as amine groups, for the conjugation of biomolecules.[30]

One of the most advantageous functionalization methods presented to date comes from the Capobianco group at Concordia University. They have recently developed a method to synthesize ligand-free, water dispersible lanthanide-doped nanoparticles by focusing on the removal of the oleate ligand from the nanoparticle surfaces.[31] Complete removal of the oleate ligand directly addresses the problem that many previous coating and functionalization methods attempted to address. The resulting nanoparticles are water dispersible, and have a unique advantage in that they can be directly functionalized through interactions with the trivalent lanthanide ions on the nanoparticle surfaces.

1.6 – Temperature Sensitivity

One unique aspect of upconverting lanthanide-doped nanoparticles that has been gaining attention in recent years is the fact that the luminescent emission from these nanoparticles is sensitive to changes in temperature. Many of the upconverting nanoparticles that can be synthesized exhibit narrow emission bands, each of which is sensitive to temperature. Taking the ratio of the intensity of two emission bands from these nanoparticles provided a "referenced signal for optical sensing of temperature".[14] This luminescent dependence on temperature varies within the physiological temperature range (20-50^{o}C), which is particularly appealing for biomedical applications.

Emission bands from upconverting nanoparticles, specifically $NaYF_4$:Er,Yb nanoparticles, exhibit temperature dependence that stems from the from the level transitions in the Er^{3+}/Yb^{3+} co-doped system. Increasing temperature also increases the

rate of nonradiative relaxation between transition states, and as a result, the luminescence intensities and lifetimes of various transitions decrease.[16]

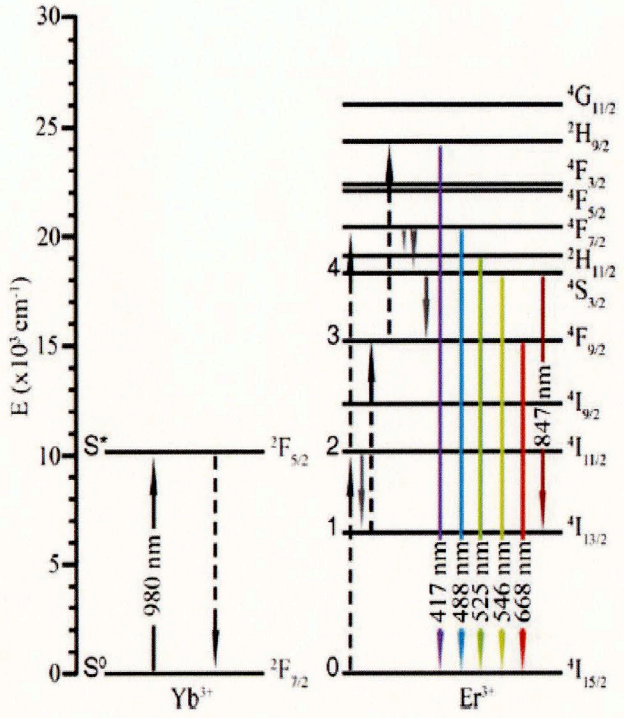

Figure 2. Energy level diagram of energy transfer system between Yb^{3+} and Er^{3+} in $NaYF_4$:Er^{3+},Yb^{3+} nanoparticles. Grey arrows represent routes for nonradiative decay, dashed arrows represent excitation and decay by energy transfer from Yb^{3+} to Er^{3+}. Reproduced with permission from reference 20, copyright J Mat. Chem. 2011.

The upconversion process specific to $NaYF_4$:Er^{3+},Yb^{3+} nanoparticles is shown in Figure 2 above. The Yb^{3+} ion is initially excited from $^2F_{7/2} \rightarrow {}^2F_{5/2}$, and then nonradiatively transfers a photon to the Er^{3+} ion at $^4I_{11/2}$, $^4F_{7/2,\ or}$ $^2H_{9/2}$. From the $^4F_{7/2}$ level, there can be nonradiative energy decay to either $^2H_{11/2}$ or $^4S_{3/2}$, and the nanoparticles can then emit a photon to produce green emission at 525nm or 546nm through both the $^2H_{11/2} \rightarrow {}^4I_{15/2}$ and $^4S_{3/2} \rightarrow {}^4I_{15/2}$ transitions. The $^4S_{3/2}$ and $^2H_{11/2}$ levels can also nonradiatively decay to the

$^4F_{9/2}$ level, and then emit a photon to produce red emission at 668 nm through the $^4F_{9/2} \rightarrow {}^4I_{15/2}$ transition. Yb^{3+} ions can also transfer photons to the $^4I_{11/2}$ level of Er^{3+} ions, which can then be further excited to the $^4F_{9/2}$ level. The $^4I_{11/2}$ level can also decay to the $^4I_{13/2}$ level, which can be excited back up to the $^4F_{9/2}$ level by an additional energy transfer from Yb^{3+}. Population of the $^2H_{9/2}$ level of Er^{3+} ions results in emission at 417nm from the $^2H_{9/2} \rightarrow {}^4I_{15/2}$ transition, although the emission from this pathway is usually at a much lower intensity than the other emission bands. When the nanoparticles are heated, the 521 nm emission band from $NaYF_4:Er^{3+},Yb^{3+}$ nanoparticles resulting from the $^2H_{11/2}$ to $^4I_{15/2}$ level transition is promoted with increasing temperature due to population of the $^2H_{11/2}$ level by thermal excitation and a quasithermal equilibrium with the $^4S_{3/2}$ state. The 668 nm emission that results from the $^4F_{9/2} \rightarrow {}^4I_{15/2}$ level transition can be populated via several different pathways, and thus this emission band does not exhibit as large a range of temperature dependence as the 521 nm emission band.Some research groups have designed experimental setups that allow for the isolation of the two green emission bands from $NaYF_4$:Er,Yb nanoparticles (band between 515-535 nm, and between 535-570 nm), that are both temperature dependent, and can construct a ratiometric temperature sensor by monitoring this green-to-green emission ratio.[15-16] Other groups have used the Er^{3+}/Yb^{3+} codoped system inside glass ceramics to monitor this same emission ratio and its dependence on temperature.[17-18]

1.7 Potential Applications Utilizing Temperature Sensitivity

$NaYF_4:Er^{3+},Yb^{3+}$ nanoparticles that exhibit temperature sensitive emission bands have been proposed for a wide array of applications, such as nanoscale thermometry and temperature monitoring of single cells[16]. They have also been proposed as a potential "noncontact" method of determining temperature, in place of commonly used "contact" methods, such as thermistors and thermoelements.[14] Luminescent temperature sensing methods in the visible and NIR regions can avoid many of the problems inherent with other "noncontact" temperature methods, such as IR thermometry.

One particular approach that utilizes these upconverting nanoparticles is to create a thin film coating using the particles onto a glass substrate. Many research groups have already attempted to make such upconverting films on various substrates, by either sol-gel processes[36], dip-coating methods[37], doping SiO_2 glass itself with the Er^{3+}/Yb^{3+} codoped system[17-18,38], or by patterning methods such as microcontact printing[39] or Langmuir-Blodgett techniques[40]. These films created on glass could have obvious applications for liquid crystal displays and solar cells[13]. Yet another application that has been proposed is their use as temperature sensitive paints.

Because the nanoparticles are temperature sensitive within the physiological range (20-50°C), there are obvious implications for use in conjunction with human cell work. One potential application specific to this research is to create a coating of the upconverting nanoparticles on the bottom of 96-well plates that are used for incubation of cell lines or during polymerase chain reaction (PCR), which relies on thermal cycling. This could

allow for precise temperature measurement and feedback of cells that are incubating, and during PCR cycles where temperatures need to be continually adjusted.

Another potential application along similar lines is to apply this nanoparticle coating to a microfluidic chip that has a microchannel. The coating could be used to monitor a continuous temperature distribution through the channel, or help provide fine control of temperature throughout specific parts of the channel. If such a coating can be produced and the temperature sensitivity of the nanoparticles monitored in a precise manner, there would be many potential applications in both the field of optics as well as biomedical applications.

There are many significant advantages of using this temperature sensitive nanoparticle coating over traditional thermometry methods. This temperature sensing ability of the nanoparticles occurs on the nanoscale, and thus is only limited by the detection limit of the experimental setup that is being used to detect the nanoparticles' emission. It has already been demonstrated that these nanoparticles can be used to internally monitor the temperature of Hela cells.[16] However, for many of the studies that have been undertaken, this ratiometric temperature measurement is obtained from the emission spectral data from the nanoparticles as they are heated. Few groups have attempted to construct this green-to-red emission ratio using emission images from the nanoparticles obtained by a ccd camera through respective green and red filters. The emission ratio could be constructed using average intensity measurements from the collected images. This would have one very distinct advantage over measuring the emission ratio using a spectrometer;

it would allow for the creation of a two-dimensional temperature distribution map, by dividing the green and red emission images. Using the upconversion emission from the nanoparticles to create a temperature distribution map opens the possibility for extremely unique applications. For the conceptual application of creating a coating on a 96-well plate, if that plate is used for cell incubation, this coating could be used to monitor a temperature distribution across a single cell. This could allow for the temperature distribution analysis during important events, such as cellular division. For such an application, accuracy and precision of the green-to-red emission ratio temperature measurement is paramount. In the earlier mentioned study of temperature monitoring of Hela cells, the Capobianco group was able to monitor the internal temperature of a Hela cell from 25°C to 45°C when it underwent thermally induced death, but they did not report on the accuracy or precision achieved with their system. In the case of using $NaYF_4:Er^{3+},Yb^{3+}$ nanoparticles, a temperature resolution limit has not yet been reported, but it is not unreasonable to aim for resolving 0.01°C temperature changes with this nanoparticle coating both accurately and precisely. The dynamic range of the green-to-red emission ratio with respect to temperature should be as high as possible to achieve such a resolution.

1.8 – Thesis Aims/Objectives

The objective of this research study is to develop a coating of upconverting nanoparticles onto a glass surface, for use as a novel ratiometric temperature sensor. The temperature sensitivity would be based on the temperature dependent emission from the

$NaYF_4:Er^{3+},Yb^{3+}$ nanoparticles, specifically the ratio of the 525nm and 668nm emission bands. There were two specific aims of this study vital to achieving the overall objective; the first was to successfully demonstrate the synthesis of α-phase $NaYF_4:Er^{3+},Yb^{3+}$ and α-phase $NaYF_4:Tm^{3+},Yb^{3+}$ nanoparticles in a controlled manner. This synthesis would be modified from previous reports in the literature, and would be demonstrated to be reproducible. Reproducibility would be determined by such factors as exhibiting a particle size range under the 30nm diameter threshold, cubic-phase crystal structure of the nanoparticles, the absence of coloration of subsequent particle dispersions, as well as quality of the upconversion luminescence exhibited from the synthesized nanoparticle samples. The second aim of this study was the incorporation of upconverting nanoparticles, specifically α-phase $NaYF_4:Er^{3+},Yb^{3+}$ particles onto a glass surface to form an upconverting glass surface. Ideally the coating would form a stable adhesion to the glass surface through some sort of functionalization or electrostatic interaction. Several methods were to be investigated for the achievement of this goal, such as electrophoretic deposition and functionalized glass wafers.

Once coated, the upconverting glass surfaces would be used in experimentation regarding the temperature-dependent emission from the nanoparticles. A linear dependence of the green-to-red emission ratio on temperature would be demonstrated within the physiological temperature range of 20°C-50°C, and the resulting calculated change in the green-to-red emission ratio (ΔGRR) or the change in the green-to-red emission ratio with

respect to temperature ($\Delta GRR/\Delta T$) should be able to be reproduced in subsequent experiments with the same coated glass sample.

Section 2

Materials and Methods

2.1 – Synthesis of α-phase $NaYF_4:Er^{3+},Yb^{3+}$ & $NaYF_4:Tm^{3+},Yb^{3+}$ Nanoparticles

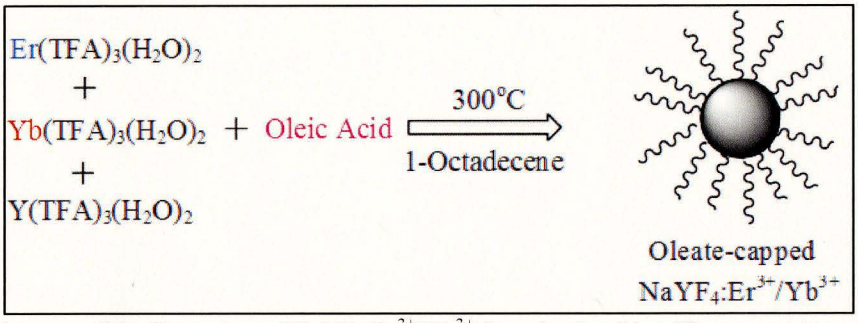

Figure 3: Diagram of the formation of $NaYF_4:Er^{3+}/Yb^{3+}$ from lanthanide trifluoroacetate precursors via high temperature synthetic method.

The synthesis of α-phase $NaYF_4:Er^{3+},Yb^{3+}$ & $NaYF_4:Tm^{3+},Yb^{3+}$ nanoparticles was adapted from a previous synthesis described in the literature[19]. The synthesis consists of first producing lanthanide trifluoroacetate precursors, and then using those dried precursors in a secondary reaction to produce lanthanide-doped nanoparticles. Lanthanide trifluoroacetate precursors were prepared using a mixture the corresponding lanthanide oxide powders and trifluoroacetic acid. The lanthanide oxides were used in the following molar ratios: 2% erbium oxide (Er_2O_3) or thulium oxide (Tm_2O_3) depending on the synthesis, 20% ytterbium oxide (Yb_2O_3), and 78% yttrium oxide (Y_2O_3). The following molar ratios correspond to roughly 9.8 mg Er_2O_3 (0.025 mmol), 98.5 mg Yb_2O_3 (0.25 mmol), and 220.2 mg (0.975 mmol) Y_2O_3 respectively. The powders were mixed together in a 50 mL one-neck round bottom flask, and to this 10 mL 50% trifluoroacetic acid (CF_3CO_2H) was added. The solution of trifluroacetic acid was produced by mixing 5 mL

99.99% trifluoroacetic acid and 5 mL H_2O that had been filtered through a Barnstead Nanopure Diamond water filtration system. The resulting solution in the flask was fitted to a reflux column and was stirred vigorously in an oil bath on top of a VWR Series 800 hotplate/stirrer set at 80°C for over 12 hours in a fume hood. (Figure 4)

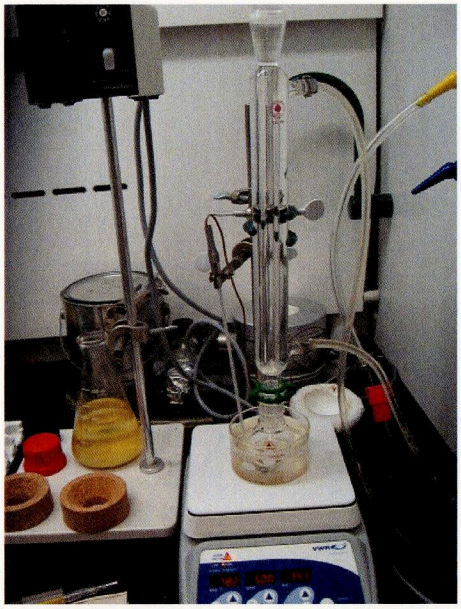

Figure 4: Setup for initial synthetic reaction to produce lanthanide trifluoroacetate precursors

After the initial reaction had come to completion, indicated by a clear solution, the solution was removed from the oil bath and allowed to cool to room temperature in the fume hood. The solution was then transferred via pipette to a 50 mL polypropylene centrifuge tube and underwent a lyophilization process. The solution was converted to a solid via submersion in a dry ice/acetone bath, for 30 minutes. Afterwards, the centrifuge tube was moved to a freeze dryer, where it was dried *in vacuo* for 72 hours

Once the lanthanide trifluoroacetate precursors were adequately dried in the fume hood, they were transferred to a 100 mL flask for the secondary synthetic reaction. (Figure 5)

To this flask 0.3400 grams (2.5 mmol) of sodium trifluoroacetate, 20 mL of 1-octadecene (90%), and 20 mL of oleic acid (90%) were added. The flask was transferred to the fume hood where it was fitted with a mercury thermometer, reflux column, and adapter for alternating vacuum and argon. The flask was set in a heating jacket with a Glas-Col PowerTrol controller on top of a VWR stirplate, and was slowly heated to 100°C over a period of 30 minutes with magnetic stirring. During this 30 minute period of thermocycling, the solution was purged periodically with dry argon and then the vacuum line, every 5 minutes. After the initial thermocycling, the solution attained a clear yellow color and was placed under light argon atmosphere and was heated to 300°C at a rate of 10°C/min. At approximately 260°C small gas bubbles were observed within the solution indicating the decomposition of the metal trifluoroacetate precursors. At approximately 280-300°C there was a burst of nucleation, which resulted in the solution becoming turbid, exhibiting a cloudy yellow color. Once the solution reached 300-310°C, it was held at this temperature for a period of 1 hour, and then allowed to cool back to room temperature within the fume hood.

Figure 5: Experimental setup for secondary synthetic reaction to produce lanthanide-doped nanoparticles. The three-neck round bottom flask is set within the heating jacket, on top of the stirplate. The left neck of the flask is supporting the mercury thermometer, middle neck is attached to the reflux column, and the right neck is used for both the vacuum and argon lines.

The nanoparticles were precipitated out of solution by the addition of 80 mL acetone, and isolated via centrifugation at 6000 rpm (4629 rcf) using an Eppendorf Centrifuge 5804R. The resulting pellet was washed twice with ethanol and dried in the fume hood, before being either dispersed in a volume of 5-10 mL of chloroform, or dried even further in the freeze dryer for subsequent experimentation.

2.2 – Experimental Controls Implemented for Nanoparticle Synthesis

During the course of optimizing the above mentioned synthetic procedure, issues arose regarding reproducibility of the nanoparticle samples, specifically with respect to resulting nanoparticle size distribution, coloration of the nanoparticle samples dispersed in chloroform, and the absence of the observed burst of nucleation between 280-300^{o}C. In order to prevent this, the following experimental controls were implemented into the synthesis to help improve nanoparticle consistency:

1. The ultraviolet light in the fume hood was kept off for the entirety of the secondary synthetic reaction.
2. In addition to the argon purging that occurs during the first 30 minutes of the secondary synthetic reaction, 2 additional argon purges were performed before the reaction was started.
3. A new batch of oleic acid was purchased and used for the synthetic reactions, and was kept in a refrigerator under argon atmosphere when not in use.
4. No vacuum grease was used in the experimental setup, specifically at the interface between the reflux column and the 100 mL 3-neck round bottom flask.
5. White rubber adapters were used for both the mercury thermometer and the argon needle, and were replaced at the first sign of any brown discoloration.

2.3 – Characterization of α-phase $NaYF_4:Er^{3+},Yb^{3+}$ & $NaYF_4:Tm^{3+},Yb^{3+}$ Nanoparticles

The size of the synthesized nanoparticles was determined via dynamic light scattering by using a Malvern Zetasizer Nano-ZS90. Two nanoparticle samples, $NaYF_4:Er^{3+},Yb^{3+}$ and $NaYF_4:Tm^{3+},Yb^{3+}$ were analyzed via X-ray diffraction to determine their crystal structures. This was performed by Dr. Channa de Silva, a colleague and assistant professor at the University of Western Carolina.

Luminescence spectra were obtained from certain samples using a 980nm diode laser and power supply, an Ocean Optics QE65000 back-thinned CCD array spectrometer, and Ocean Optics SpectraSuite software.

2.4 – Oleate Removal Procedure for α-phase $NaYF_4:Er^{3+},Yb^{3+}$ Nanoparticles

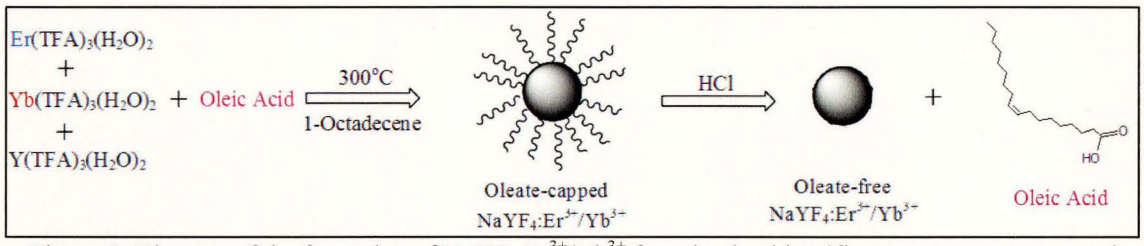

Figure 6: Diagram of the formation of $NaYF_4:Er^{3+}/Yb^{3+}$ from lanthanide trifluoroacetate precursors via high temperature synthetic method, and the subsequent oleate removal procedure to yield oleate free nanoparticles are free oleic acid.

The synthesis of oleate free α-phase $NaYF_4:Er^{3+},Yb^{3+}$ was adapted from a previous synthesis described in the literature[31]. Oleate-capped $NaYF_4:Er^{3+},Yb^{3+}$ that were previously synthesized and dried (100 mg) were dispersed in 20 mL H_2O that had been filtered through a Barnstead Nanopure Diamond water filtration system. The pH of the solution was initially adjusted to 3.5 by adding a solution of 0.1 M HCl, monitored using a SevenEasy Mettler Toledo pH meter. Afterwards, the reaction was stirred overnight for a period exceeding 12 hours. After the completion of the reaction, the sample was transferred to a 50 mL round bottom flask, where the oleic acid was removed from solution via liquid-liquid extraction with hexane 3 times. Each extraction required 30 mL of hexane to be used and the solutions to be combined in a 50 mL round bottom flask. The first 2 hexane extractions were performed for a period of 12 hours, and the final extraction was set and allowed to reach equilibrium for a period of 72 hours. Afterwards the nanoparticles were precipitated with the addition of acetone, isolated via centrifugation at 6000 rpm (4629 rcf), and were dispersed in either nanopure H_2O or acetone.

2.5 – Characterization of Oleate-free α-phase $NaYF_4:Er^{3+},Yb^{3+}$ Nanoparticles

The size of the nanoparticle samples was determined via dynamic light scattering by using a Malvern Zetasizer Nano-ZS90 and a number-weighted particle size distribution. Zeta potential measurements of certain samples were also collected using the same instrument. Removal of the oleate ligand from the nanoparticle surfaces was confirmed via FTIR characterization performed by Pablo Mancheno, a colleague in the Department of Chemical & Environmental Engineering at the University of Arizona in Dr. Anthony Muscat's research group. pH monitoring of certain samples was performed using a SevenEasy Mettler Toledo pH meter. Luminescence spectra were obtained from certain samples using a 980nm diode laser, an Ocean Optics QE65000 back-thinned CCD array spectrometer, and Ocean Optics SpectraSuite software.

2.6 – Procedure for the Creation of Carboxylated SiO_2 Glass Surfaces

The creation of all carboxylated SiO_2 glass surfaces was performed by Pablo Mancheno in the Department of Chemical & Environmental Engineering at the University of Arizona. The procedure was developed by Pablo, and adapted from related endeavors that had been previously reported in the literature.[42-43] The glass surfaces were typically microscope slides that had been cut down to smaller sizes using a diamond tipped pen. The glass surfaces were initially cleaned using acetone, methanol, and deionized water. The glass was placed in a solution of each solvent for a period of 5 minutes, and

underwent sonication in a sonic bath. Afterwards the glass was rinsed with deionized water and dried using nitrogen.

At this point the glass underwent chemical oxidation in piranha solution, a strong oxidizing agent that is used extensively in the semiconductor industry, to create hydroxyl groups on its surface. The glass was placed in a solution of pirahna that was composed of a 3:1 solution of 30 mL sulfuric acid (H_2SO_4), and 10 mL hydrogen peroxide (H_2O_2). The glass in solution was heated at 80°C for 10 minutes using a hot water bath, and afterwards it was again rinsed with deionized water and dried using N_2.

After the glass surfaces were hydroxylated, a self-assembled monolayer (SAM) deposition of vinyl tetrachloride silane (VTCS) was performed on the surface. The glass was placed in a solution of VTCS and acetone at a ratio of 1:1000 respectively, and was kept in solution for a period of 24 hours, and then dried using N_2 gas.

Finally, using a permanganate-periodate oxidation reaction, the carbon-carbon double bonds of the deposited VTCS molecules were oxidized to form carboxylic groups on the glass surface. The permanganate-periodate solution was made up of 1 mL $KMnO_4$ (5 mM), 1 mL $NaIO_4$ (195 mM), 1 mL K_2CO_3 (18 mM), and 7 mL H_2O. The glass was placed in the solution for 24 hours. Afterwards the glass was rinsed with 20 mL each of the following solvents: $NaHSO_3$ (0.3 M), H_2O, 0.1 M HCl, H_2O, and ethanol. Figure 5 depicts the overall process of creating the carboxylic functionalization on the glass surfaces.

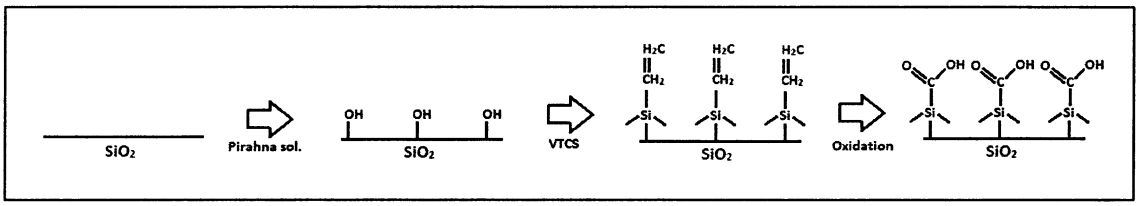

Figure 7: Depiction of process to create carboxyl functionalization on SiO_2 glass surfaces

Experimentation was performed regarding the surface quality of the SiO_2 glass slides. Initially, the microscope slides that were used were simply cut using the diamond tipped pen and then underwent the carboxylation procedure. A cross-hatch pattern was created on the surface of some of the glass samples using a diamond tipped pen that underwent carboxylation. In later experiments, sand-blasted microscope slides were cut down to size using a diamond tipped pen and underwent the carboxylation process.

2.7 – Coating Procedure – Oleate-free Nanoparticles onto Carboxylated SiO_2 glass samples

Initial glass coating experiments were performed using oleate-free α-phase $NaYF_4:Er^{3+},Yb^{3+}$ nanoparticles and the carboxylated SiO_2 glass samples. The nanoparticles were dispersed in either water, acetone, or isopropyl alcohol at known concentrations, and were then pipetted onto the SiO_2 glass samples in a fume hood. Typically, 200 μL of the nanoparticle solution was pipetted onto each glass sample. The sample was then allowed to dry overnight in the fume hood for a period exceeding 12 hours, after which time the glass surface had become visibly cloudy instead of transparent. This type of coating procedure was performed on glass samples that did not have a cross-hatch pattern, that did have a cross-hatch pattern, and those that had been initially sandblasted before undergoing the carboxylation procedure.

Presence of upconverting nanoparticles on the carboxylated glass samples were confirmed using 980nm excitation from the diode laser, and also by collection of luminescence spectra from certain coated glass samples.

A glass sample was also produced using a standard microscope slide and a sample of oleate-capped $NaYF_4:Er^{3+},Yb^{3+}$ dispersed in chloroform, for comparison. 200 μL of the nanoparticle solution was pipetted onto the slide surface and was dried in the fume hood overnight.

2.8 – Coating Procedure – Dipping Method

One set of carboxylated glass samples was coated by a "dipping" method, in which the glasses were dipped into a stirred solution of the oleate-free nanoparticles in water. For this experiment, only sand-blasted carboxylated glass samples were used. Each glass was dipped into a solution of oleate-free nanoparticles, in which 100 mg of particles had been dispersed in 20 mL of nanopure H_2O, with a measured pH of 5.26, and a measured zeta potential of 20.6 mV. Four glass samples were coated, and were dipped in the solution for the following times; 10 seconds, 1 minute, 2 minutes, and 48 hours. The samples were then tested for the presence of upconverting nanoparticles via 980 nm excitation from the diode laser, and images were taken using an Olympus MVX10 microscope, ImageX nano-TGI imaging system, and ImageX nano-TGI software.

2.9 – Coating Procedure – Electrophoretic Deposition of Oleate-free Nanoparticles onto ITO Glass Slides

The procedure of depositing the nanoparticles onto indium tin oxide (ITO) glass slides was adapted from a previous paper described in the literature[41]. ITO slides were cleaned via a 5 minute sonication in acetone, methanol, and nanopure water respectively, before being dried in the fume hood. Once dry, two slides were clamped together and separated by a plastic spacer. The width of the spacer was set at 1 inch. Oleate-free nanoparticles (100 mg) were then dispersed in 80 mL of water or isopropyl alcohol and the solution was pH adjusted using 0.1 M HCl. The Bio-Rad PowerPac Basic power supply was then hooked up to the ITO slides, and the slides were placed in the nanoparticle solution in a beaker. Two successful trials were performed, once with the power supply set at 200 V and run for 2 minutes, and once with the power supply set at 200 V and run for 2 minutes and 37 seconds. Figure 8 illustrates the experimental setup used for all EPD experimentation.

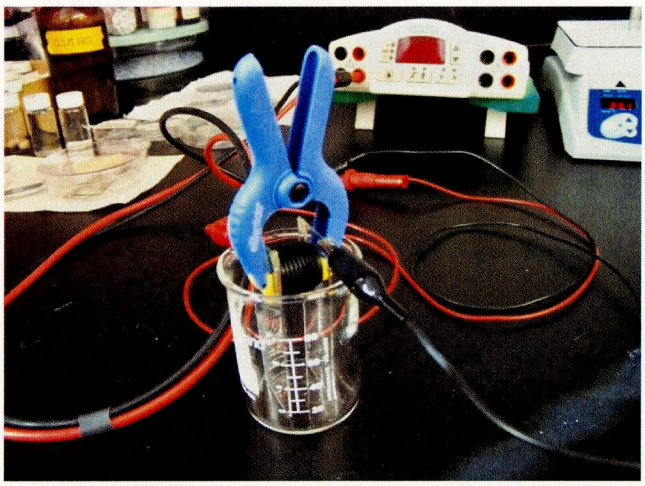

Figure 8: Experimental setup for the electrophoretic deposition experiments. Two ITO slides were clamped together around the 1 inch spacer, and placed in the beaker containing the nanoparticle solution (not shown here) The electrical leads from the power supply were then connected to each of the ITO slides.

2.10 – Laser & Microscope Setup

The laser and microscope setup that was used for the temperature sensitivity experimentation using the coated glass samples underwent numerous changes during the course of this research. Initially, an Olympus MVX10 MacroView fluorescence microscope was placed onto the optical table, and laser excitation was provided by a tunable optical parametric oscillator (OPO) pumped by a Nd:YAG laser tuned to 980nm, with a 3 ns pulse width, and 20 Hz pulse repetition rate. The laser spot was directed onto the microscope stage plate using a set of mirrors.

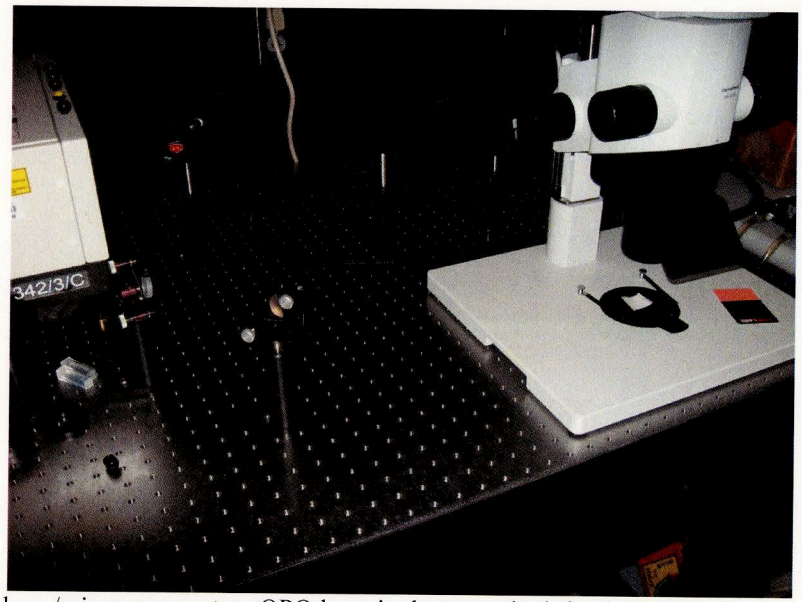

Figure 9: Initial laser/microscope setup. OPO laser is shown at the left, along with the mirrors directing the beam path and the MVX10 microscope, on the right.

Images corresponding to the specific green and red emission bands were collected using an ImageX nano-TGI imaging system, and the ImageX nano-TGI software. To isolate both the green and red emission bands, two specific microscope filters were used; a

Chroma GFP filter for the 521nm emission band, specifically the ET525/50m filter, and a Chroma D655/40m filter for the 668nm emission bands.

To achieve a more uniform laser spot size on the stage plate, the setup underwent several modifications. First, the stage plate of the microscope was removed, and the microscope itself was bolted to the optical table by use of a smaller modified base plate procured from Thor Labs. The stage itself was then replaced with a VWR Series 800 Hotplate/Stirrer, which would be used for temperature variation of the coated glass samples. An oil bath was placed onto the hot plate, out of view of the objective lens, in which the hot plate's thermometer was placed for temperature feedback during the temperature experiments. Finally, a dichroic mirror (Edmunds Hot Mirror 45 Degree AOI, 50.0mm Square) was positioned between the Olympus MV Plapo 1X objective lens of the microscope and the hotplate, to direct the laser beam onto the stage to achieve a more uniform laser spot size. (Figures 10-11)

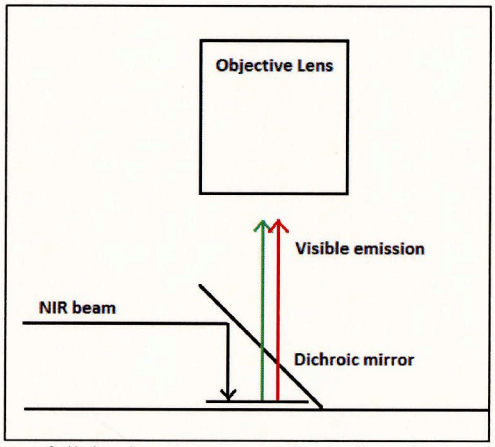

Figure 10: Depiction of dichroic mirror setup in conjunction with microscope setup

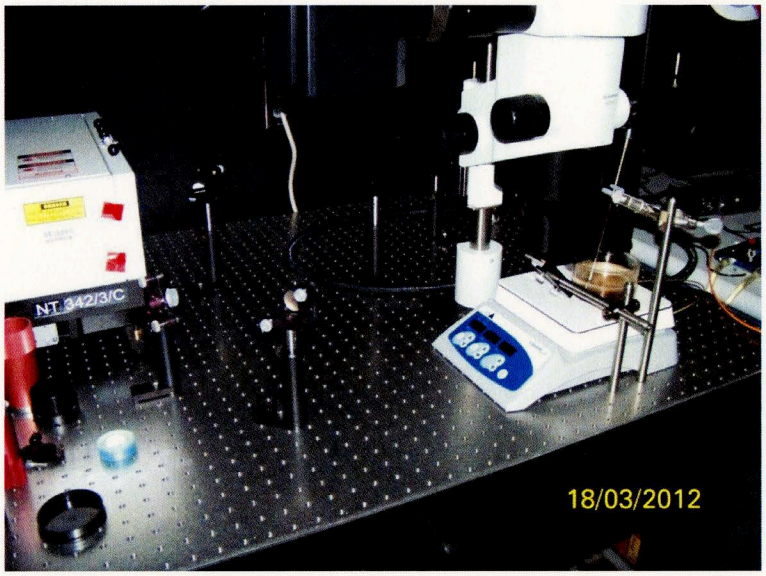

Figure 11: Laser/microscope setup 2 where the microscope has been mounted to the optical table, the baseplate is replaced with the hotplate, and the dichroic mirror is positioned to direct the 3ns laser beam onto the hotplate.

For the final laser/microscope setup, the OPO, mirrors, and dichroic mirror were removed completely and replaced with a 980 nm diode laser and power supply. The beam was directed onto the hotplate by use of an optical fiber, which had a lens on the end of it to produce a broader, well-defined laser spot size. The oil bath on the hotplate's surface was also removed, and the hotplate thermometer was set to rest on the surface of the plate. To avoid any reflection of the NIR beam off of the glossy surface of the hot plate, a series of black surfaces were used as an effective stage plate. First, the black stage plate from the MVX microscope was placed on top of the hotplate, and then a piece of black metal to increase thermal conductivity. When it became apparent that the heat dissipation through these materials was taking a lengthy amount of time, they were replaced by using black PVC electrical tape that was rated for up to 80^{o}C, which was placed on the surface of the

hot plate under the 1X objective lens. The thermometer was then placed on a corner of the electrical tape for better temperature feedback (Figures 12-13).

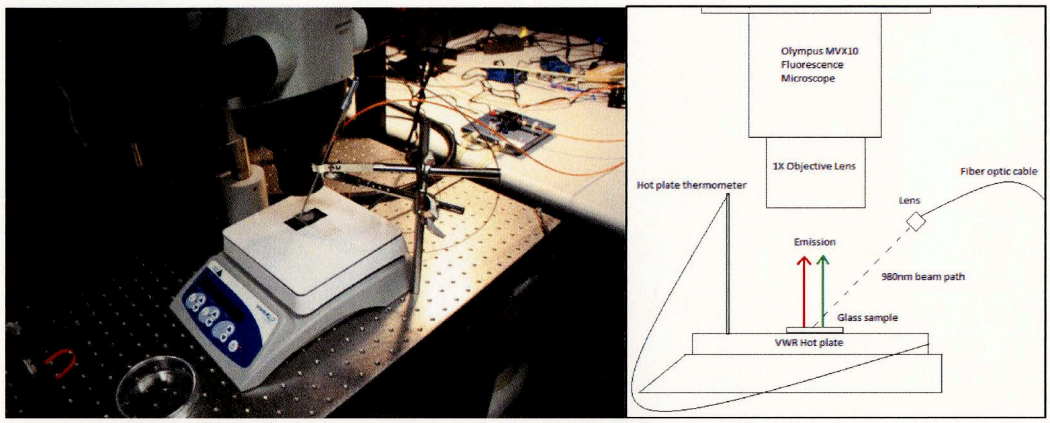

Figure 12: Left: Final laser/microscope setup where the diode laser/optical fiber is providing excitation source, stage plate has been replaced with PVC tape, and the hot plate thermometer is directly on the PVC tape. Right: Schematic of final laser/microscope setup

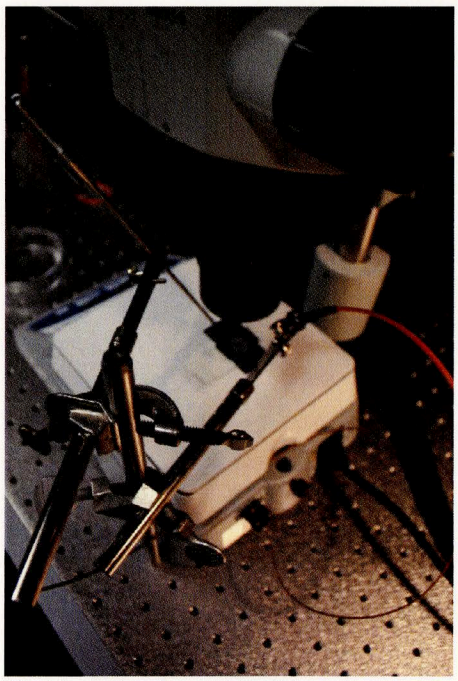

Figure 13: Alternate view of final laser/microscope setup

2.11 – Temperature Sensitivity Experimentation – Emission Ratio Curves using Oleate-capped Nanoparticles in Chloroform

Before experimentation using the coated glass samples and their temperature sensitivity, the emission ratio curves of the temperature sensitivity of $NaYF_4:Er^{3+},Yb^{3+}$ nanoparticles in chloroform was constructed. For this experiment, 1 mL of the nanoparticle dispersion (Sample 106A, see Table 1) was pipetted into a square glass cuvette and was capped. The cuvette was placed in a water-cooled cuvette holder (Figure 14) that was attached to a water circulator. The water circulator was used to vary the sample temperature between 10-50°C, in 5°C increments.

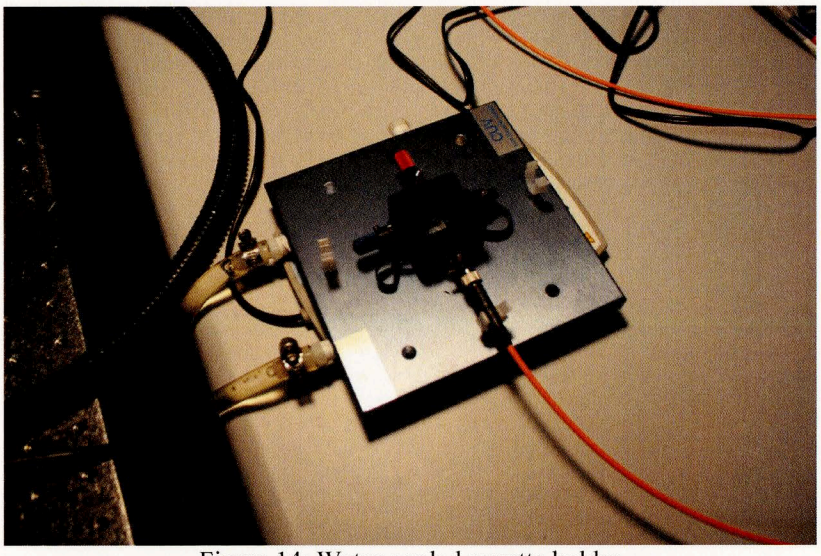

Figure 14: Water-cooled cuvette holder

The sample was excited via 980nm excitation from a diode laser, and luminescence spectra were obtained using an Ocean Optics QE65000 back-thinned CCD array spectrometer and Ocean Optics SpectraSuite software. Using the spectral data and the intensities of the emission peaks at 521nm, 541nm, and 668nm at each temperature

interval, the following ratios were constructed to demonstrate the temperature dependence of the nanoparticles' emission; 521nm/541nm, 521nm/668nm, and 541nm/668nm.

2.12 – Temperature Sensitivity Experimentation – Coated Glass Samples

The temperature sensitivity experiments were performed using the above mentioned final laser and microscope setup, along with the hotplate as the stage. The glass samples were positioned on the hot plate, under the 1X objective lens of the microscope, and were brought into focus using the ImageX nano-TGI software. The temperature of the glass sample was varied between a specific temperature range, usually between 10-50°C, in intervals of 5°C using the hot plate. Secondary confirmation of the temperature of the glass sample was performed through use of a laser thermometer. At each temperature interval, a small section of the glass was excited by a laser spot created by the 980nm diode laser, fiber optic, and lens. The diode laser power supply was set using a pulse width of 100 μs, and 1350 mA intensity. The CCD camera itself had a delay of 100 μs and was set to be triggered by the diode laser. For every 1 millisecond of exposure time, there was a 100 μs laser pulse, followed by the camera shutter being open for a gate width of 800 μs, before being closed again for 100 μs before the next laser pulse. (Figure 15) This was done to limit the amount of NIR excitation light that would be collected in the resulting images.

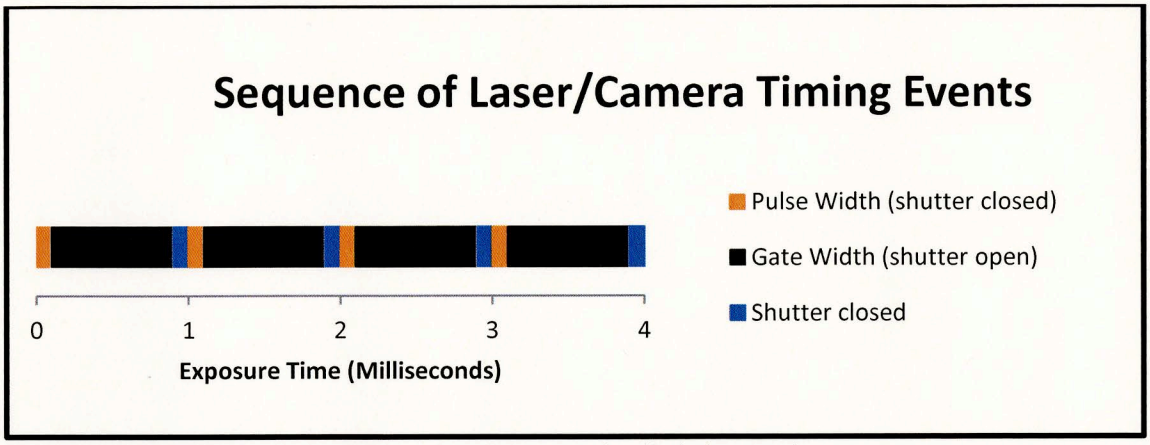

Figure 15: Sequence of timing events for diode laser and camera system

At each temperature interval, a set of images was collected through both constructed green and red filter cubes respectively, that would correspond with both the desired green and red emission bands. A set of background images were also taken through each filter and background subtraction was performed on collected images.

Using the ImageX nano-TGI software, for each image in each set, an average intensity measurement was taken over an area of the image corresponding to the laser spot size. Since only a small area of the slide was illuminated using the NIR laser beam, the area used to calculate the average intensity measurements was specific to each experiment, but was kept consistent for all calculated values for each experiment. After all of the values had been recorded and background subtraction had been performed, the intensity measurements for the green and red emission were averaged and the standard deviation was calculated. The ratio of the green to red emission was calculated and a plot of the Green-to-Red emission ratio vs. temperature was created. Plots of the average green and red emission individually vs. temperature was also constructed using the averaged

emission intensity data. Error bars were constructed for all plotted points using 1 standard deviation, and standard error was also calculated for all points.

2.13 – Temperature Sensitivity Experimentation – Creation of Nanoparticle Coating on 25 mL glass flask

To demonstrate a practical application of the temperature sensitivity of the nanoparticle coating, a nanoparticle coating was created on a 25 mL glass flask for a subsequent temperature sensitivity experiment. To create the coating, 200 μL of sample OAR10-12 (see Table 2) was pipetted onto the flask label area, consisting of a durable white enamel material, and was allowed to dry in the fume hood overnight. Once dry, there was a well-defined coating of nanoparticles over the label area on the flask.

To demonstrate the temperature sensitivity of this flask coating, the flask was filled with 25 mL of 1-octadecene, the heat transfer solvent used in the nanoparticle syntheses, and a stir bar was added. The flask was placed on top of the VWR hot plate in the laser/microscope setup, and the diode laser fiber optic and lens was focused on the nanoparticle coating on the flask. A Sper Scientific 4 Channel datalogging thermometer and attached thermocouple were used to read the actual temperature of the solvent as the nanoparticle coating on the glass was a significant distance away from the hot plate surface itself. The thermometer had been previously calibrated and the temperature readings displayed good consistency with the temperatures that were set on the hot plate. The temperature of the solvent was varied between 10-50°C, in intervals of 5°C using the hot plate and stir bar. Collection of images corresponding to the green and red emission

from the flask coating was done in the same manner as the coated glass samples. Figure 16 depicts the experimental setup using the flask coating.

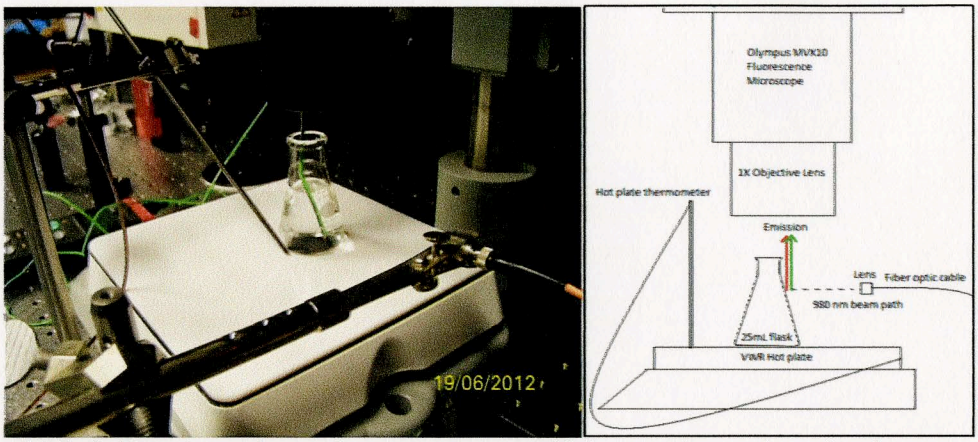

Figure 16: Left: Experimental setup for temperature sensitivity experimentation using the nanoparticle coating on the 25 mL flask. Right: Schematic of experimental setup

2.14 – Temperature Sensitivity Experimentation – 2D Temperature Distribution

Once all of the experimentation regarding the construction of the Green-to-Red emission ratio for all of the coated glass samples was completed, a final temperature experiment was carried out to determine whether a 2D temperature distribution map could be created from the respective images taken through both the green and red filters. For this experiment, glass sample GE14 was placed atop an aluminum cylinder on the hot plate and was heated to 37°C. The cylinder had a 0.286 cm diameter and a length of 0.400 cm, and the spot size created by the diode laser was slightly larger than the diameter of the cylinder itself, and was aligned to the same position. Images were collected using the same procedure as the previous temperature sensitivity experiments; the 980 nm diode laser provided the excitation source and was directed to the sample using an attached fiber optic and lens.

Images were taken of the aluminum cylinder in room light, the laser spot size aligned with the cylinder location, and an image of the GE14 sample on the cylinder. Once the slide had reached 37°C, images were taken through both the green and red filter cubes, and background subtraction was also performed. Then, the images themselves were divided using the ImageX software, to provide a Green-to-Red ratio emission profile across the entire sample, specifically the area in which the nanoparticles on the slide were being excited. For comparison, the slide was also taken off of the aluminum cylinder and allowed to reach 37°C while resting directly on the hot plate. At this point, images were again taken through the green and red filter cubes, and the Green-to-Red ratio emission map across the sample was again created.

Section 3

Results

3.1 – Synthesis & Characterization of α-phase $NaYF_4:Er^{3+},Yb^{3+}/Tm^{3+},Yb^{3+}$ Nanoparticles

Once the nanoparticles had been successfully synthesized and dispersed in chloroform, emission spectral data from many of the samples were obtained. For the $NaYF_4:Er^{3+},Yb^{3+}$ samples, the main emission peaks in the green and red spectra regions were expected to be at 525nm, 546nm, and 668nm, as previously reported by our research group.[20] The main emission peaks are present in the newly synthesized samples (see Table 1), but their positions have small variations from the expected values.

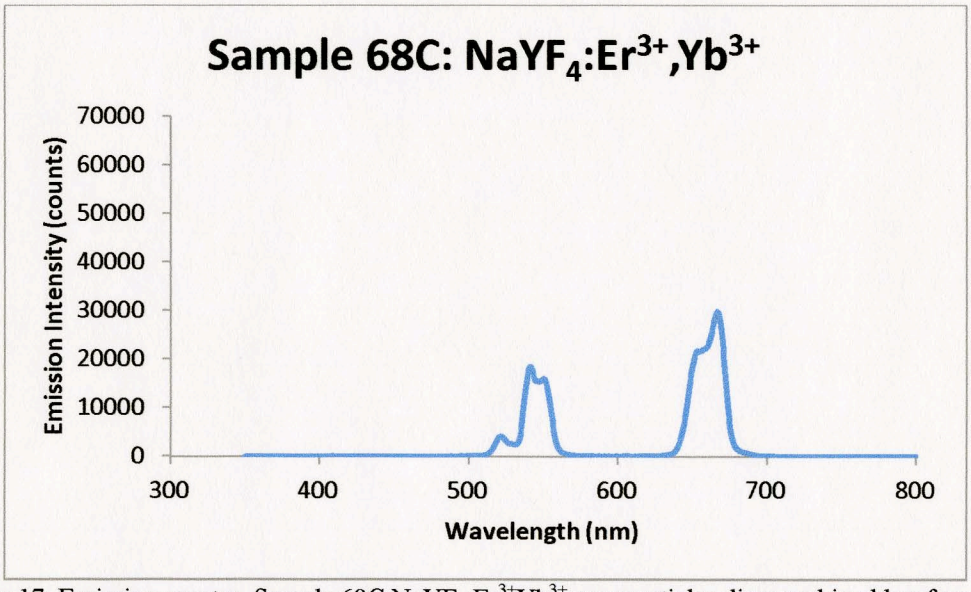

Figure 17: Emission spectra, Sample 68C $NaYF_4:Er^{3+}Yb^{3+}$ nanoparticles dispersed in chloroform, 60s integration time.

Sample 68C was synthesized **before** the controls were implemented into the nanoparticle synthesis procedure, and had an average particle diameter of 5.182 nm. Its emission

spectra at room temperature shows well defined peaks at 521 nm, 541 nm, and 667 nm. Using a pulse width of 100 µs, 10.00% duty cycle, 1000 mA intensity, and a 60 second integration time, the maximum intensity for the 521 nm emission was 4176 counts, the maximum intensity for the 541 nm peak was 18564 counts, and the maximum intensity for the 667 nm emission was 29884 counts.

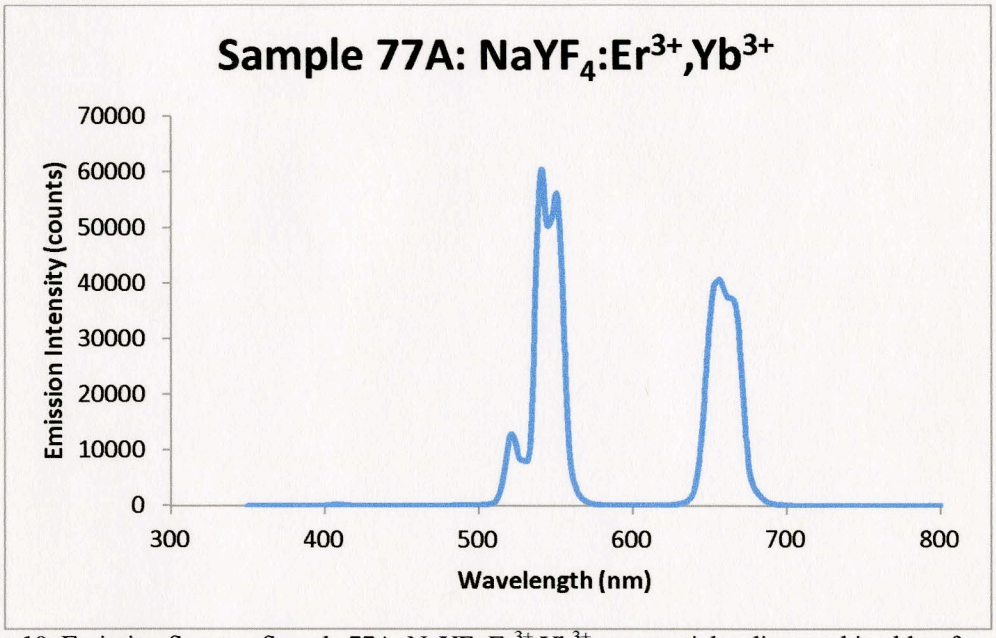

Figure 18: Emission Spectra, Sample 77A, $NaYF_4:Er^{3+},Yb^{3+}$ nanoparticles dispersed in chloroform, 60s integration time.

Sample 77A was synthesized **after** the controls were implemented into the nanoparticle synthesis procedure, and had an average particle diameter of 37.19 nm. Its emission spectra at room temperature shows well defined peaks at 521 nm, 541 nm, and 656 nm. Using a pulse width of 100 us, 10.00% duty cycle, 1000 mA intensity, and a 60 second integration time, the maximum intensity for the 521 nm emission was 12889 counts, the maximum intensity for the 541 nm peak was 60601 counts, and the maximum intensity for the 656 nm emission was 40786 counts.

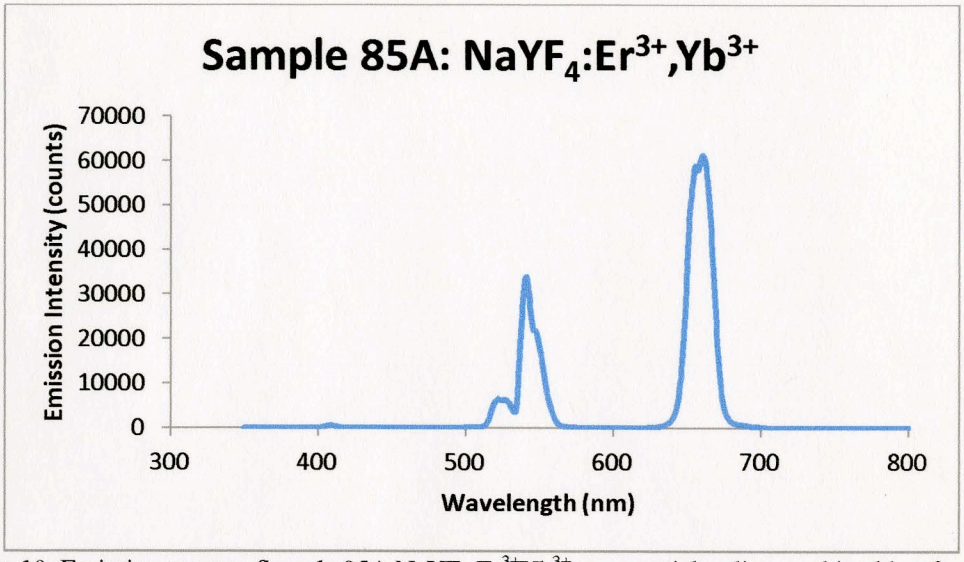

Figure 19: Emission spectra, Sample 85A $NaYF_4:Er^{3+}Yb^{3+}$ nanoparticles dispersed in chloroform, 1s integration time.

Sample 85A was synthesized after the controls were implemented into the nanoparticle synthesis procedure, and had an average particle diameter of 12.66 nm. Its emission spectra at room temperature shows well defined peaks at 522 nm, 541 nm, and 660 nm. Using a pulse width of 1.0 us, 10.00% duty cycle, 1000 mA intensity, and a 1 second integration time, the maximum intensity for the 522nm emission was 6538 counts, the maximum intensity for the 541 nm peak was 33998 counts, and the maximum intensity for the 660 nm emission was 61294 counts.

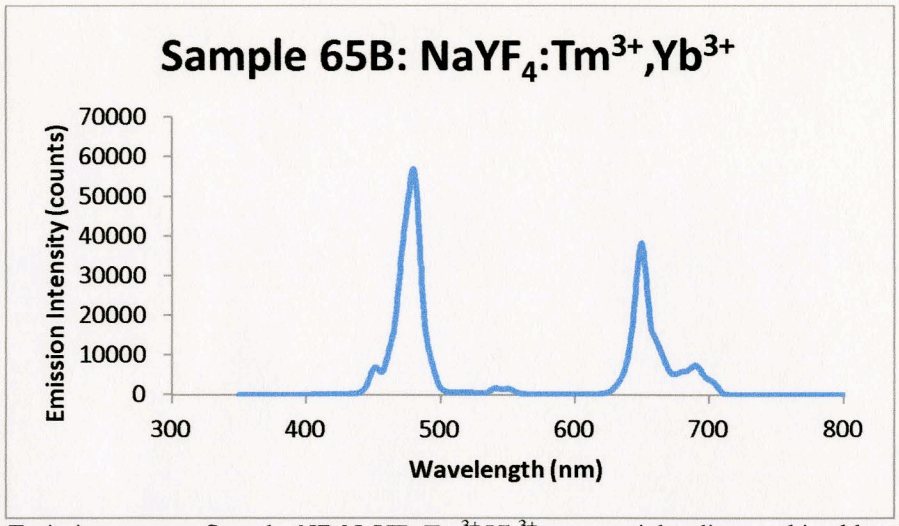

Figure 20: Emission spectra, Sample 65B $NaYF_4:Tm^{3+},Yb^{3+}$ nanoparticles dispersed in chloroform, 20s integration time. Emission band at 800nm not visible due to 700 nm shortpass excitation filter used.

Sample 65B was synthesized before the controls were implemented into the nanoparticle synthetic procedure, and had an average particle diameter of 10.55 nm. Its emission spectra at room temperature shows well defined peaks at 479 nm and 649 nm, with smaller peaks visible at 451 nm, 541 nm, and 689 nm. Using a pulse width of 100 us, 10.00% duty cycle, 1000 mA intensity, and a 20 second integration time, the maximum intensity for the 451 nm emission was 7070 counts, the maximum intensity for the 479 nm peak was 57061 counts, the maximum intensity for the 541 nm emission was 1717 counts, the maximum intensity for the 659 nm emission was 38370 counts, and the maximum intensity for the 689nm emission was 7565 counts. There should be an emission peak at 800 nm, which is usually of the most interest with thulium-doped nanoparticles, but this peak was not visible in the spectra due to the 700nm shortpass excitation filter that was used.

XRD Characterization of both $NaYF_4:Er^{3+},Yb^{3+}$ and $NaYF_4:Tm^{3+},Yb^{3+}$ nanoparticle samples was performed by Dr. Channa de Silva at Western Carolina University. This was done mainly to confirm the cubic-phase crystal structure of the synthesized nanoparticles, both erbium-doped and thulium-doped.

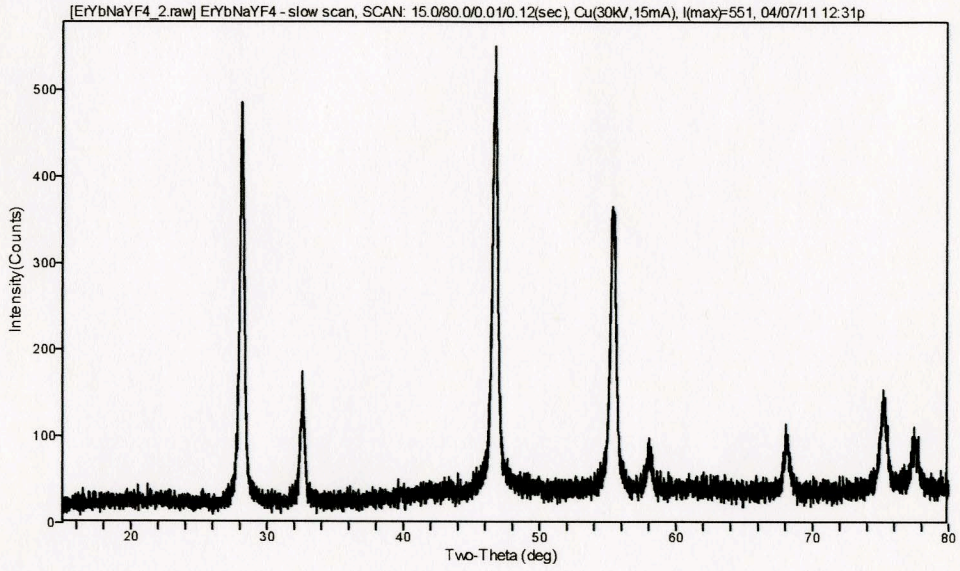

Figure 21: XRD Characterization of $NaYF_4:Er^{3+},Yb^{3+}$ nanoparticles

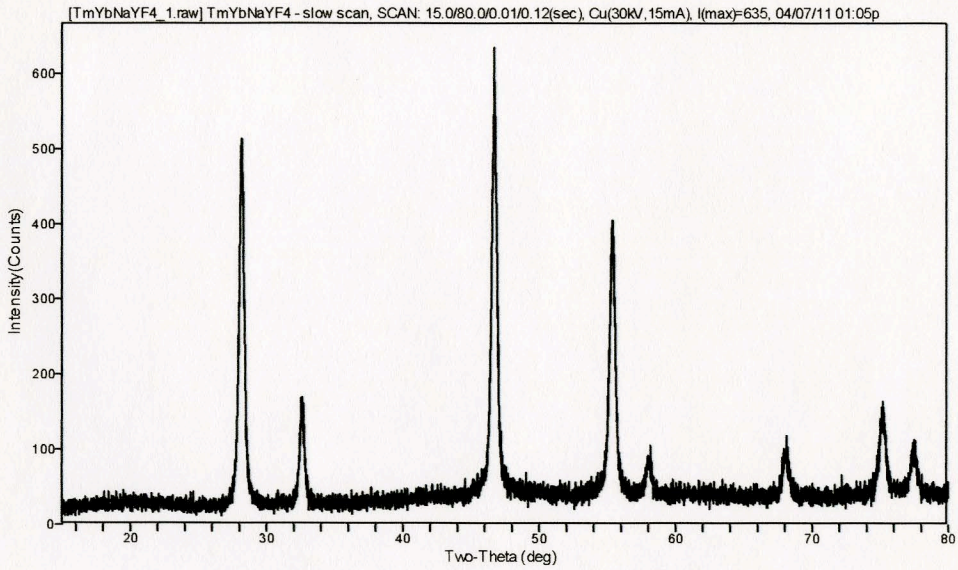

Figure 22: XRD Characterization of $NaYF_4$:Tm^{3+},Yb^{3+} nanoparticles

The XRD patterns for both analyzed samples, shown in Figures 21-22, have well defined peaks, which indicate the high crystallinity of the synthesized nanoparticles. The peak positions and intensities from the XRD patterns also match closely with the calculated line pattern for cubic α-$NaYF_4$ for both samples[19], as shown in Figure 23 below.

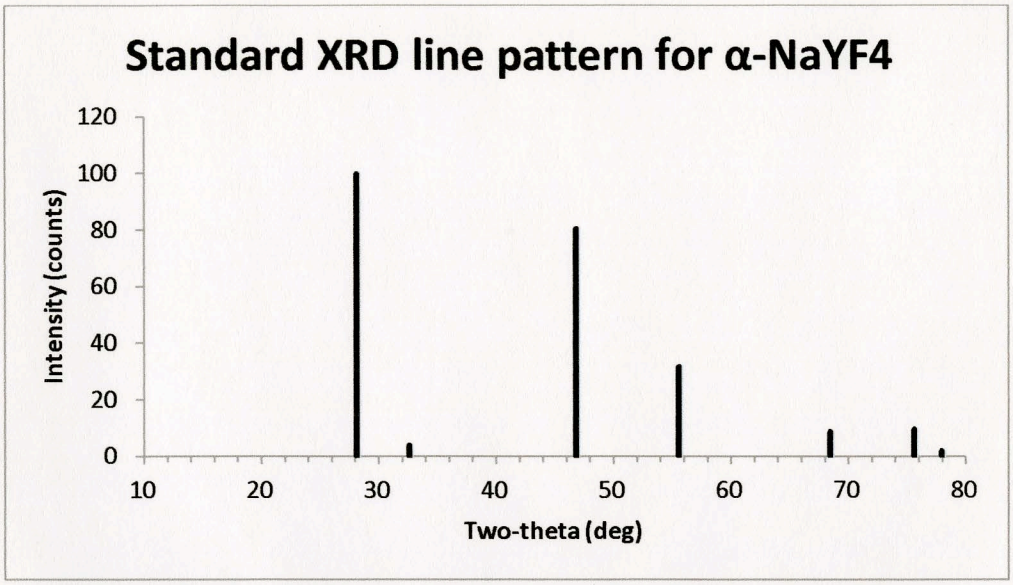

Figure 23: Standard XRD pattern of pure cubic NaYF4 (JCPDS card No. 77-2042)

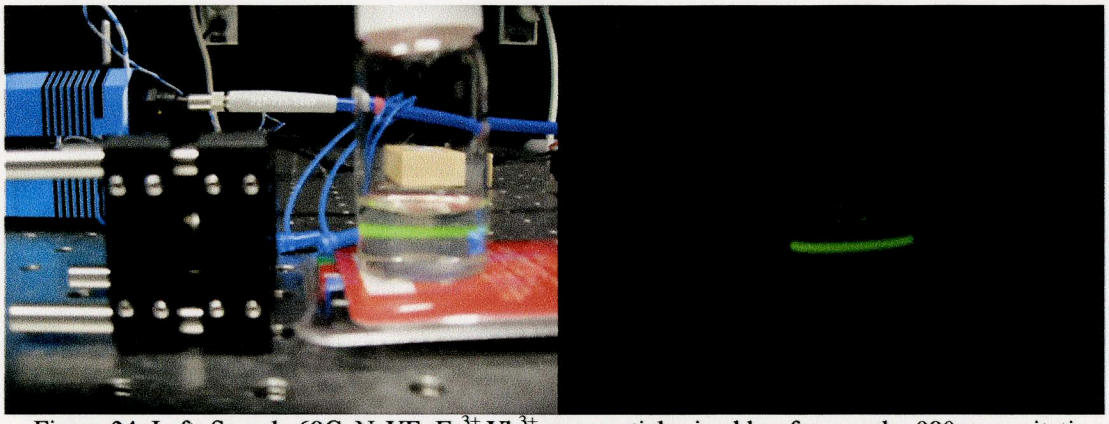

Figure 24: Left: Sample 68C, $NaYF_4:Er^{3+},Yb^{3+}$ nanoparticles in chloroform under 980nm excitation in room light Right: Same sample under 980nm excitation in dark room

As shown in figure 24, $NaYF_4:Er^{3+},Yb^{3+}$ nanoparticles dispersed in chloroform exhibited bright upconversion luminescence under excitation with a 980 nm diode laser, and appeared green in color. This upconversion could be visibly seen in both room light and in darkness.

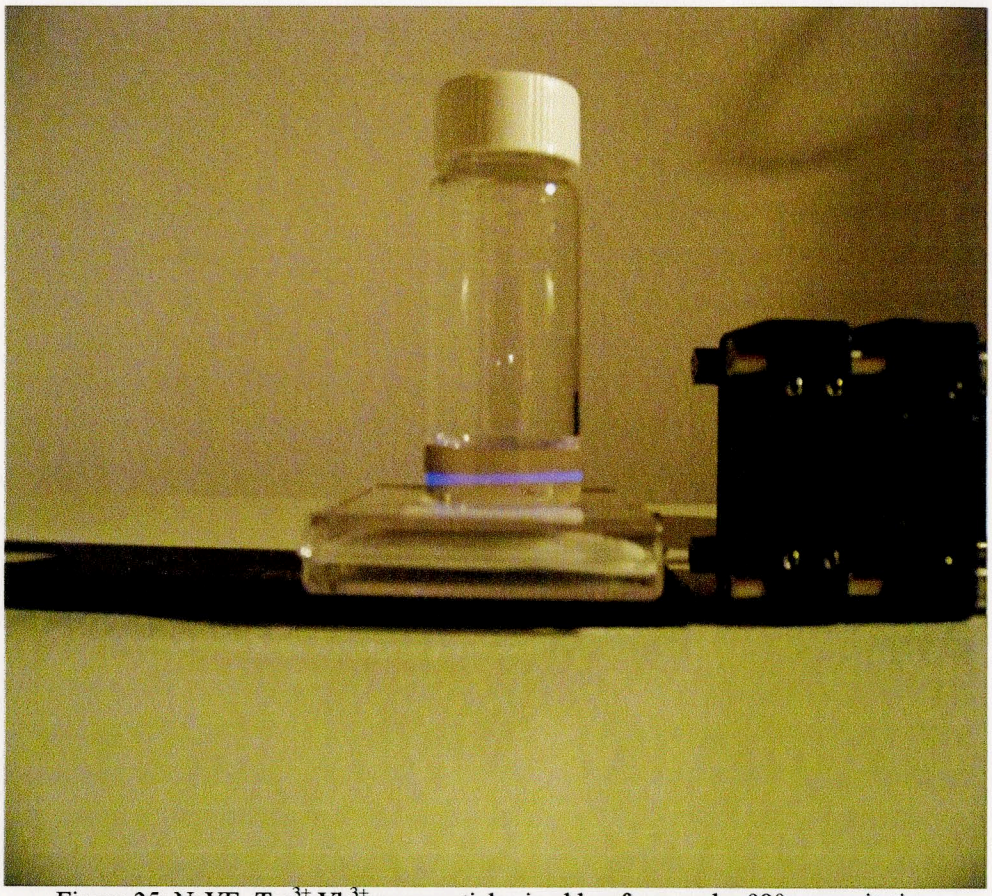

Figure 25: $NaYF_4:Tm^{3+},Yb^{3+}$ nanoparticles in chloroform under 980nm excitation

Only certain samples of $NaYF_4:Tm^{3+},Yb^{3+}$ nanoparticles dispersed in chloroform exhibited visible upconversion luminescence under excitation with a 980nm diode laser. However, the spectral data collected from these samples did indicate the presence of emission peaks, indicating that the upconversion process was occurring. Figure 25 is of one of the thulium-doped samples brightly upconverting in room light conditions. While this blue colored emission could be observed in dark room conditions, it was difficult to capture an image using a digital camera that depicted this.

Sample Name	Type	Dispersant	Diameter (nm)	Peak Width (nm)
$NaYF_4$:Tm,Yb	$NaYF_4$:Tm,Yb	Chloroform	10.55	2.597
Sample 59B	$NaYF_4$:Er,Yb	Chloroform	11.57	3.514
Sample 59C	$NaYF_4$:Er,Yb	Chloroform	39.53	10.26
Sample 61A	$NaYF_4$:Er,Yb	Chloroform	35.86	10.41
Sample 61B	$NaYF_4$:Er,Yb	Chloroform	105.5	37.57
Sample 61C	$NaYF_4$:Er,Yb	Chloroform	34.19	9.347
Sample 63B	$NaYF_4$:Er,Yb	Chloroform	5.139	1.43
Sample 65B	$NaYF_4$:Tm,Yb	Chloroform	10.55	2.597
Sample 64C	$NaYF_4$:Er,Yb	Chloroform	80.36	39.2
Sample 64A	$NaYF_4$:Er,Yb	Chloroform	5.714	0.982
Sample 64B	$NaYF_4$:Er,Yb	Chloroform	19.82	4.8
Sample 868A	$NaYF_4$:Er,Yb	Chloroform	53.94	28.47
Sample 68C	$NaYF_4$:Er,Yb	Chloroform	5.182	1.207
Sample 73C	$NaYF_4$:Er,Yb	Chloroform	2.691	0.392
Sample 74A	$NaYF_4$:Er,Yb	Hexane	18.63	4.932
Sample 76A	$NaYF_4$:Er,Yb	Chloroform	47.18	18.83
Sample 76B	$NaYF_4$:Er,Yb	Chloroform	122.9	39.13
Sample 77A	$NaYF_4$:Er,Yb	Chloroform	37.19	10.22
Sample 78A	$NaYF_4$:Er,Yb	Chloroform	8.986	2.274
Sample 81A	$NaYF_4$:Er,Yb	Chloroform	11	3.176
Sample 82A	$NaYF_4$:Er,Yb	chloroform	54.61	7.49
Sample 85A	$NaYF_4$:Er,Yb	Chloroform	12.66	4.091
Sample 86A	$NaYF_4$:Er,Yb	Chloroform	75.35	16.84
Sample 87A	$NaYF_4$:Er,Yb	Chloroform	12.77	3.035
Sample 90A	$NaYF_4$:Er,Yb	Chloroform	18.44	5.594
Sample 91A	$NaYF_4$:Er,Yb	Chloroform	22	6.298
Sample 91B	$NaYF_4$:Er,Yb	Chloroform	7.125	1.928
Sample 105C	$NaYF_4$:Er,Yb	Chloroform	15.92	3.808
Sample 106A	$NaYF_4$:Er,Yb	Chloroform	18.99	4.567
Sample 106C	$NaYF_4$:Er,Yb	Chloroform	18.31	4.16
Sample 107A	$NaYF_4$:Er,Yb	Chloroform	16.4	4.036
Sample 109A	$NaYF_4$:Er,Yb	Chloroform	28.48	5.464

Table 1: List of nanoparticle samples synthesized and particle sizing data

Table 1 lists all the nanoparticle samples synthesized during the course of this research, in chronological order, along with the initial particle sizing data results. It is important to

note that the experimental controls were enacted in full for the synthesis of Sample 81A, and onwards.

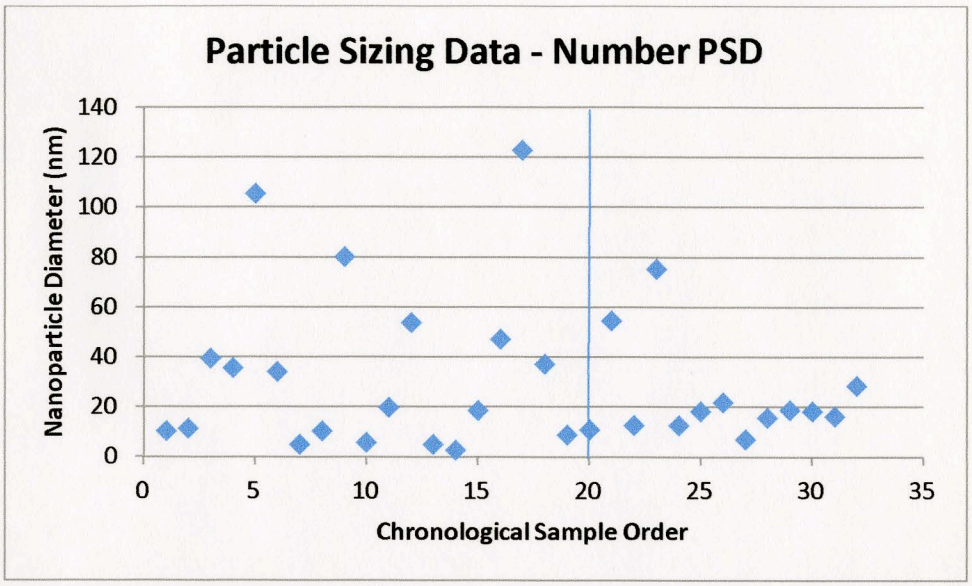

Figure 26: Particle sizing data for all synthesized nanoparticle samples using a number-weighted particle size distribution, nanoparticle diameter vs. chronological sample order. The line at '20' indicates when the experimental controls were added into the synthetic procedure.

Figure 26 was created using the available particle sizing data for the synthesized nanoparticle samples that was listed in Table 1 above. Before experimental controls were introduced to the synthetic procedure, the average particle diameter range varied drastically between synthesized samples, between 2.691-122.9 nm. Only 47.37% of those samples fell below the desired 30 nm particle diameter threshold. After the experimental controls were introduced to the synthesis the average particle diameter range decreased significantly to 7.125-28.58 nm, with two outlier samples with particle diameters of 54.61 and 75.35 nm. After the experimental controls were introduced, 12 out of 14 synthesized

samples, or 85.71% of the samples had average particle diameters under the desired 30 nm diameter threshold.

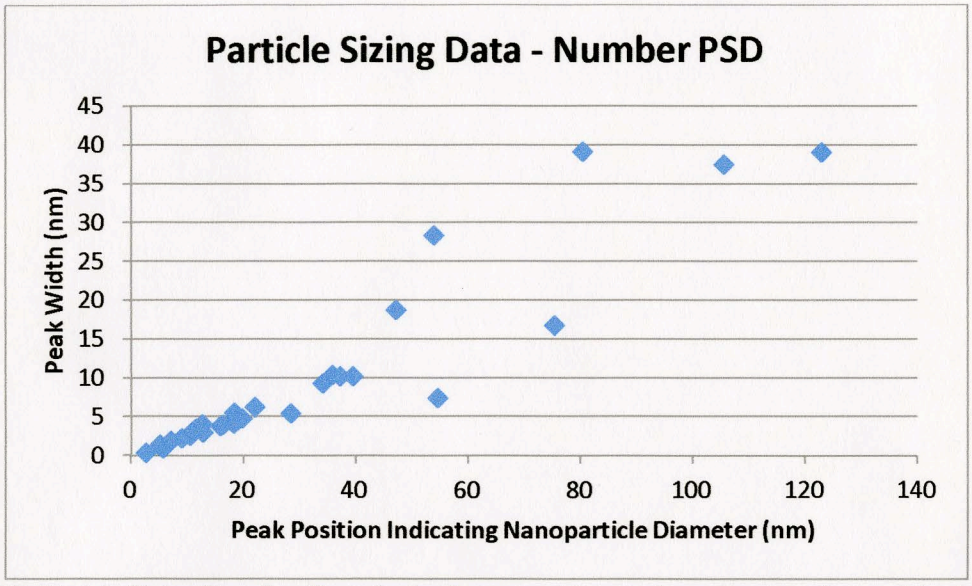

Figure 27: Particle Sizing Data for all synthesized nanoparticle samples using a number-weighted particle size distribution, peak width vs. nanoparticle diameter.

Comparing the peak width vs. main peak position for all the particle sizing number psd data, it can be seen that most of the synthesized nanoparticle samples fell within a specific range; 78.13% of all nanoparticle samples had measured nanoparticle diameters below 40.0 nm, with corresponding peak widths below 11.0nm.

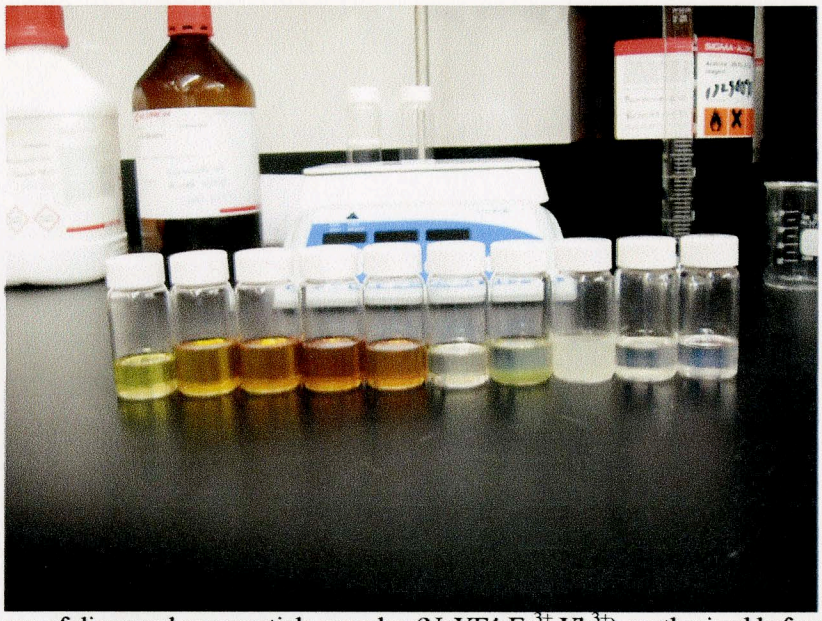

Figure 28: Images of dispersed nanoparticle samples ($NaYF4:Er^{3+},Yb^{3+}$) synthesized before controls were implemented.

Figure 28 depicts various nanoparticle samples dispersed in chloroform, synthesized before the experimental controls were added to the synthetic procedure. It can be clearly seen that in addition to the particle diameter variation, there is significant coloration in many of the synthesized samples that varies from sample to sample. Sample coloration ranges from clear, to cloudy white/yellow, to dark orange solutions.

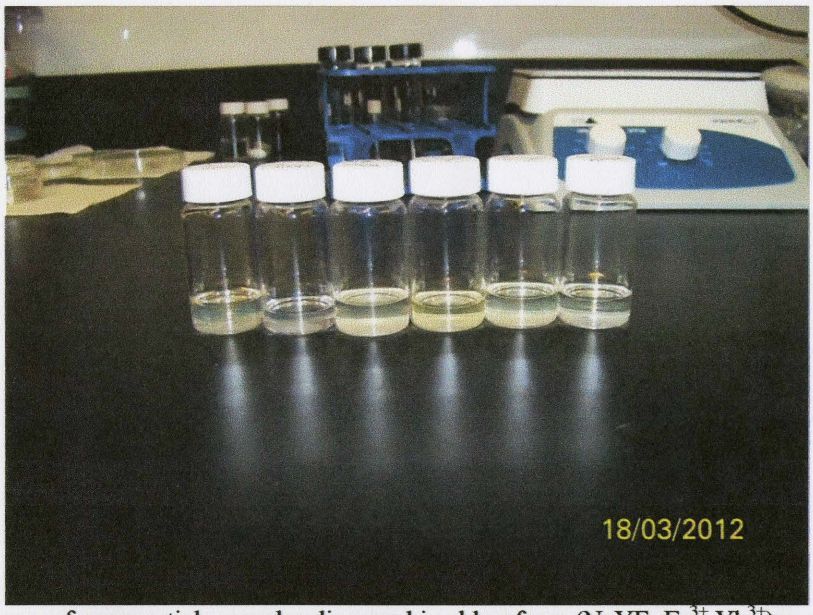

Figure 29: Images of nanoparticle samples dispersed in chloroform ($NaYF_4$:Er^{3+},Yb^{3+}) synthesized after controls were implemented.

In sharp contrast, dispersed nanoparticle samples synthesized after experimental controls were added to the synthetic procedure exhibit little to no sample coloration, and appear clear.

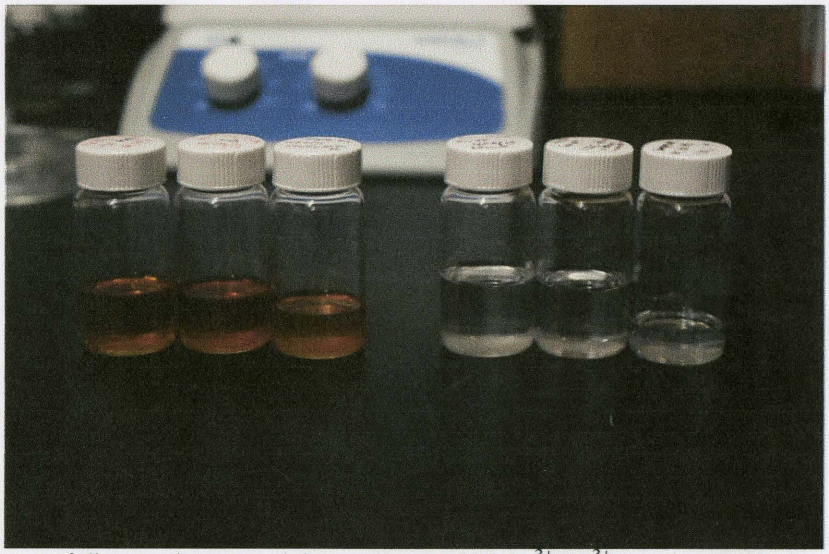

Figure 30: Images of dispersed nanoparticle samples ($NaYF_4$:Er^{3+},Yb^{3+}) synthesized before controls were implemented (left), and after controls were implemented (right).

A visual comparison between nanoparticle samples created before the experimental controls were added and after the controls were added clearly illustrate the absence of sample coloration in the newly synthesized samples (Figure 30).

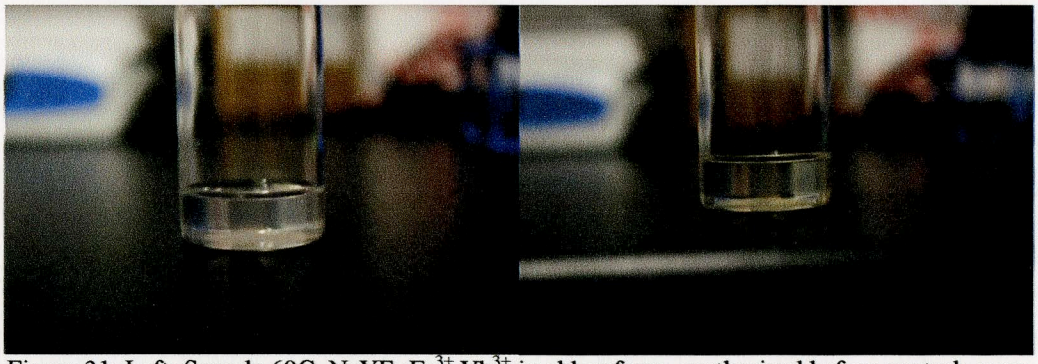

Figure 31: Left: Sample 68C, $NaYF_4:Er^{3+},Yb^{3+}$ in chloroform, synthesized before controls were implemented Right: Sample 109A, $NaYF_4:Er^{3+}$ in chloroform, synthesized after controls were implemented.

However, not all samples synthesized before the experimental controls were implemented exhibited this coloration. Sample 68C, shown on the left of figure 31, had an average particle diameter of 5.182 nm, smaller than any of nanoparticle samples synthesized after the controls were implemented. When compared to sample 109A, synthesized after controls were implemented which had an average particle diameter of 28.48 nm, it can be seen that both samples are clear and absent of any significant coloration.

3.2 - Oleic Acid Removal Experiments

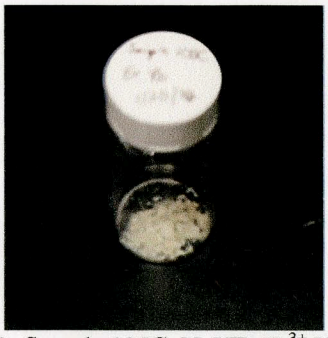

Figure 32: Sample 105C: $NaYF_4:Er^{3+},Yb^{3+}$ dried

Nanoparticle samples that underwent oleic acid removal processes first had to be isolated and dried in a freeze dryer. Figure 32 depicts the nanoparticles in this dried form.

Trial	NP Sample Used	Original Sample Diameter (nm)	Dispersant	OA-free Sample Diameter (nm)	Peak Width (nm)
OAR1	77A	37.19	Water	-	-
OAR2	77A	37.19	Water	-	-
OAR3	82A	54.61	Water	-	-
OAR4	82A	54.61	Water	147.9	68.92
OAR5	82A	54.61	Water	539.4	96.12
OAR6	82A	54.61	Water	168.3	66.33
OAR7	85A	12.66	Water	86.44	19.93
OAR8	85A	12.66	Water	510.2	113.6
OAR8	85A	12.66	IPA	297.5	52.86
OAR9	85A	12.66	IPA	106.5	29.04
OAR10	90A	18.44	Water	-	-
OAR11	90A	18.44	Water	-	-
OAR12	90A	18.44	Water	155	37.97
OAR10-12	90A	18.44	Water	221.4	96.42
OAR13	106A	18.99	Water	376.8	130.9
OAR14	106A	18.99	Water	308.6	73.89
OAR15	106A	18.99	Water	414.1	73.03
OAR16	106A,105C	18.99, 15.92	Water	545.3	137.7

Table 2: Table listing information for all oleic acid removal (OAR) samples that were synthesized

Table 2 above provides a table of every oleic acid removal (OAR) sample that was synthesized during the course of this research and available particle sizing data. In addition, the information for the original oleate-capped nanoparticle samples that were used along with their sizing data is also provided. Unfortunately for some of the early samples (OAR1-3), particle sizing data was not obtained. For OAR10, OAR11, and OAR12, these samples underwent the oleate removal process individually with the intent to combine all the samples once the process was completed. That is why sizing data is present for OAR12, and the combination of OAR10-12, but not for samples OAR10 or OAR11 individually. Certain samples were also dispersed in multiple solvents; for example 2 entries are present for OAR8, because it was initially dispersed in water but then redispersed in IPA for the electrophoretic deposition.

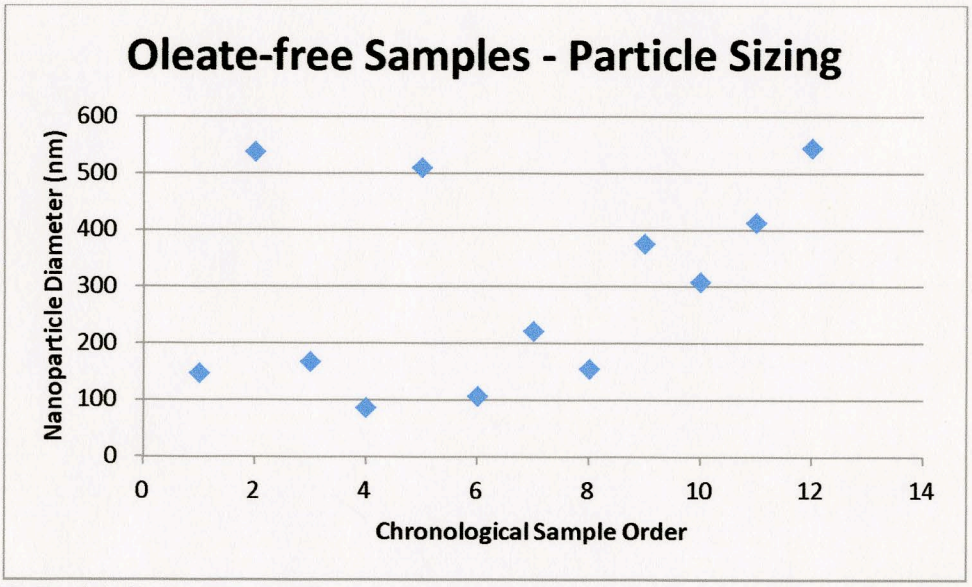

Figure 33: Particle Sizing Data for all synthesized oleate-free nanoparticle samples, nanoparticle diameter vs. chronological sample order.

Figure 33 was created using the available particle sizing data for the OAR samples that was listed in Table 2 above. The average particle diameter varied drastically between samples, with a range between 86.44-545.3 nm. Considering that the oleate removal process was performed specifically on nanoparticle samples with an average diameter of either below 20 nm or around 60 nm, these results are in sharp contrast to the particle sizing data for the original oleic acid coated nanoparticles. It is also important to note that when multiple particle sizing measurements were taken consecutively of the same sample, that there were sometimes significant variation between sizing measurements of the same sample. This seems to indicate that some of the larger particles were constantly falling out of suspension during particle sizing, producing inaccurate results.

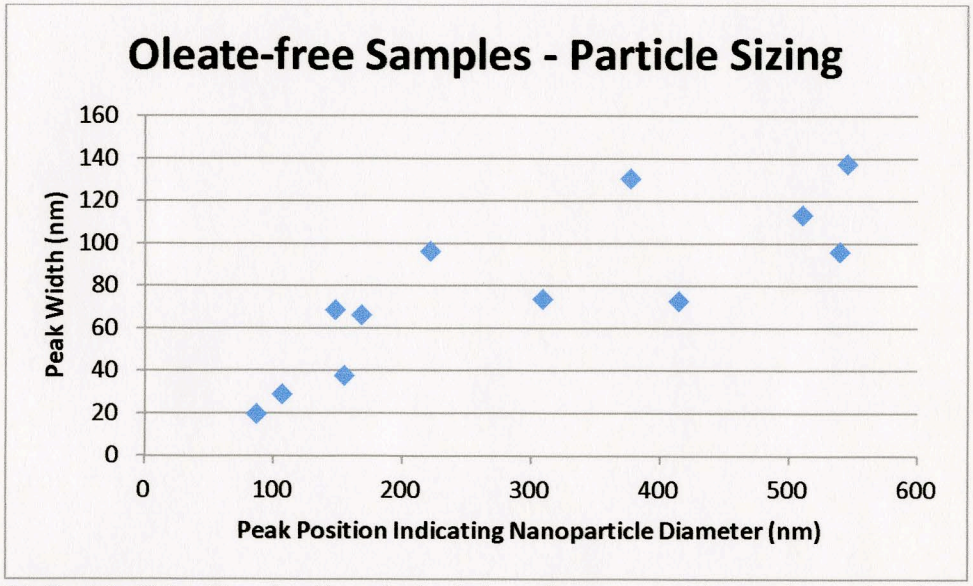

Figure 34: Particle Sizing Data for all synthesized oleate-free nanoparticle samples, peak width vs. main peak position.

Comparing peak width vs. main peak position for all particle sizing data for the oleate-free samples, it can be seen that the majority of the samples do not fall within any specified range (Figure 34).

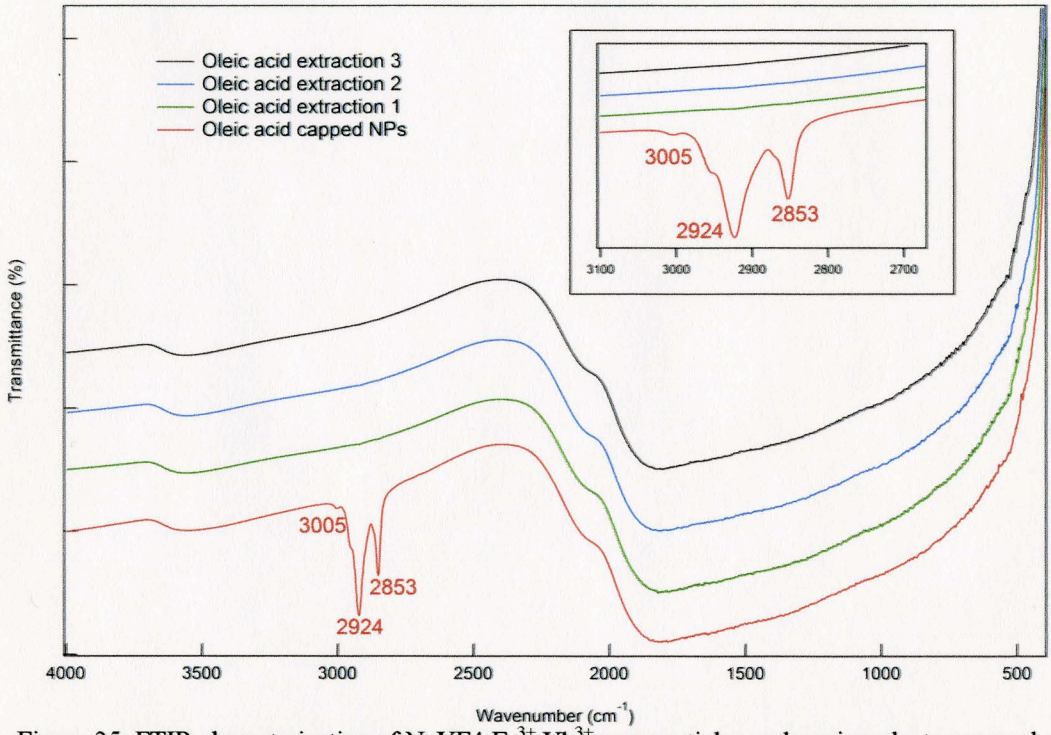

Figure 35: FTIR characterization of NaYF4:Er^{3+},Yb^{3+} nanoparticles undergoing oleate-removal process

To demonstrate the removal of the oleic acid from the surfaces of the nanoparticles, FTIR characterization was performed on one of the nanoparticle samples that underwent the oleate removal process, at each extraction step. Figure 35 shows that the synthesized oleic acid coated nanoparticles exhibit two peaks at 2853 cm^{-1} and 2924 cm^{-1}. These peaks represent CH_2 bond stretching and are indicative of the oleic acid on the nanoparticle surfaces. However, following the oleate-removal process, it can be seen that these peaks are absent even after the first hexane extraction after the oleate removal

process is performed, and are absent in the spectra for the second and third hexane extraction steps as well. This data suggests that after the simple acid treatment of the nanoparticles, it appears that the majority (<99%) of the oleic acid is removed from the nanoparticle surfaces.

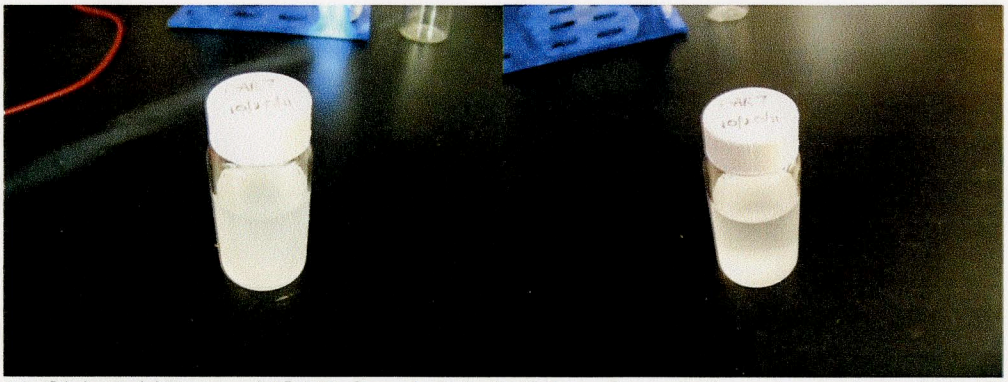

Figure 36: Oleic Acid Removal (OAR) Sample 7. Left: Taken after agitation using sonicator bath. Right: Picture taken 10 minutes later.

Consistent with the particle sizing data, when the oleate-free nanoparticles are dispersed in water, the resulting solution is cloudy and light scattering is clearly evident. In contrast with the oleic acid capped nanoparticles, the oleate-free nanoparticles fall out of solution after varying periods of time, and require agitation via mechanical shaking or sonication to achieve dispersion. Even with sonication, the nanoparticles will again fall out of solution given enough time. Figure 36 shows one such oleic acid removal (OAR) sample. The left panel shows the sample directly after agitation with the sonicator, and the right panel shows the sample 10 minutes after that sonication has taken place. It can be clearly seen that after 10 minutes, most of the nanoparticle sample has settled on the bottom of the glass vial, even though the solution is still somewhat cloudy in appearance.

Figure 37: Oleic Acid Removal (OAR) samples 14, 15, and 16 after being agitated by sonicator bath.

This cloudy dispersion was evident in many of the dispersed oleate-free nanoparticle samples.

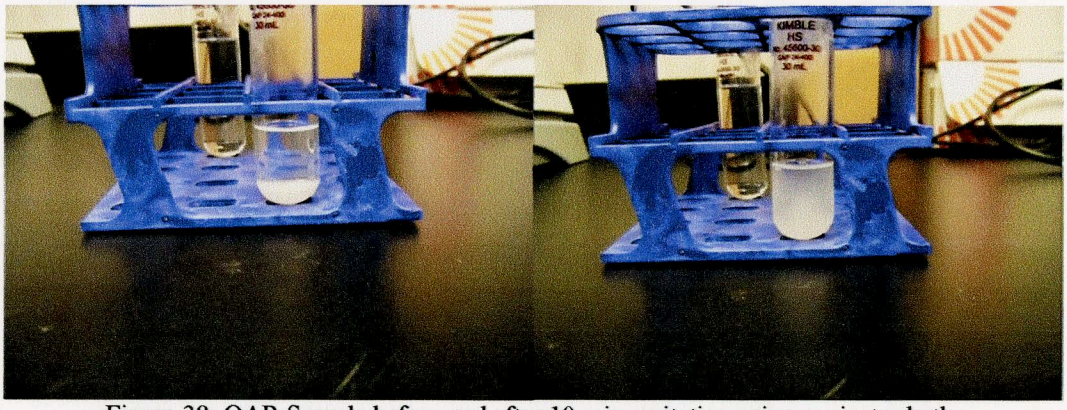

Figure 38: OAR Sample before and after 10 min. agitation using sonicator bath.

However given a significant enough length of time, nanoparticles that had undergone the oleate-removal process would settle to the bottom of the centrifuge tube or vial, as seen in Figure 38. Agitation with the sonicator bath would result in a dispersion of these particles throughout the medium, but would not result in a stable colloidal solution.

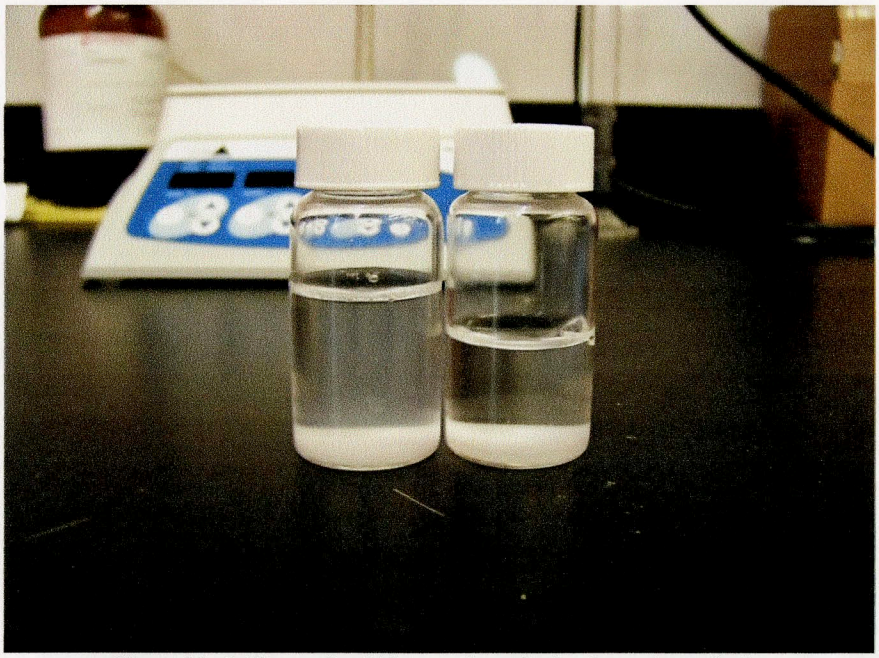

Figure 39: OAR samples 24 hours after agitation by sonicator bath.

Given a full 24 hours to equilibrate after sonication, most of the OAR samples have the majority of the nanoparticles settled on the bottom of the vial, while the supernatant appears clear (Figure 39).

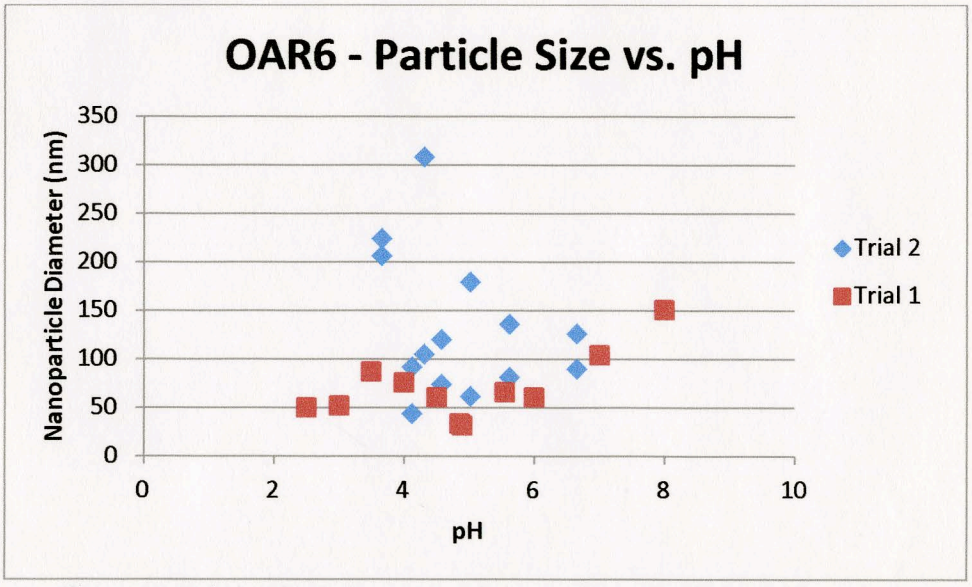

Figure 40: Relationship between particle size and sample pH for OAR6 sample

For OAR sample 6, the relationship between particle size and pH was investigated. (Figure 40) The pH was varied between 2.5 and 8.0, and the nanoparticle solution was sized at each pH interval. The initial trial shows particle size increasing at pH 3.5 and between pH 4.86 and 8.0. The particle size ranges between 31.22-150.2 nm diameter. However, an earlier sizing measurement of sample OAR6 at pH 4.0 puts the particle diameter at that pH at 163.8nm. A subsequent trial with sample OAR6 sample was performed in the pH range from 3.35-6.65, with 2 sizing measurements taken at each pH interval. The particle diameters in this trial ranged between 44.22-308.3 nm diameters. It appears as though in this trial the particle size is decreasing with increasing pH, however there are large inconsistencies between the two particle sizing measurements at each pH interval that call into question the accuracy of these results. For example at pH 4.30, back to back sizing measurements of OAR6 yield particle sizes of 308.3nm and 105.3nm respectively.

As stated previously, there was sometimes significant variation between sizing measurements of the same sample. This seems to indicate that some of the larger particles were constantly falling out of suspension during particle sizing, producing inaccurate results. This large variation in the particle sizing measurements of the same sample makes it difficult to determine whether there exists a clear dependence between particle size and pH.

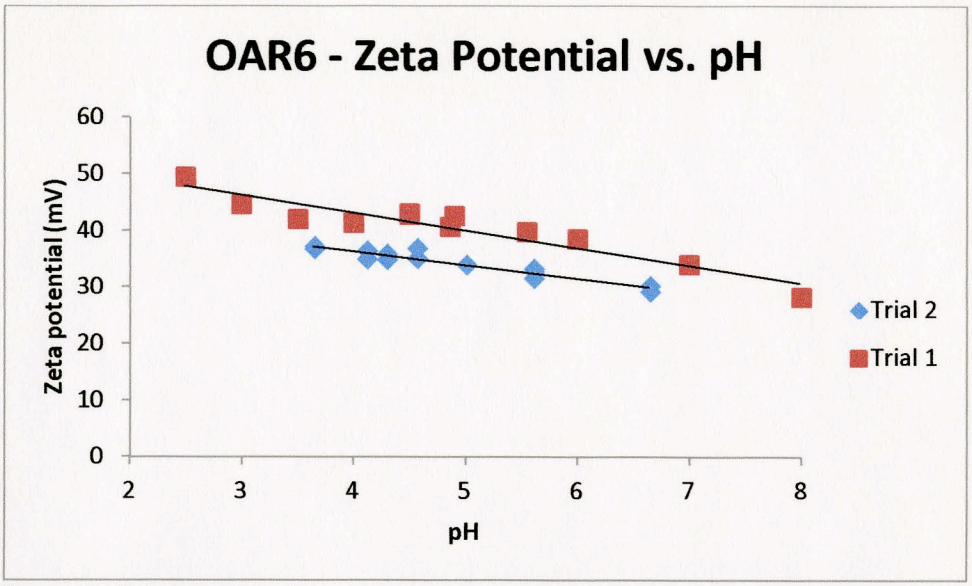

Figure 41: Relationship between measured zeta potential and sample pH for OAR6 sample

For the same OAR sample 6, the relationship between zeta potential and pH was also investigated (Figure 41). The pH was again varied between 2.5-8.0 for trial 1, and 3.35-6.65 for trial 2. For the first trial, the zeta potential varied between 49.4 mV at pH 2.5 and 28.2 mV at pH 8.0. For the second trial, the zeta potential varied between 37.2 mV at pH 3.65 and 29.2 mV at pH 6.65. Even though the zeta potential results of both trials vary slightly, they both depict the same trend of decreasing zeta potential with increasing solution pH.

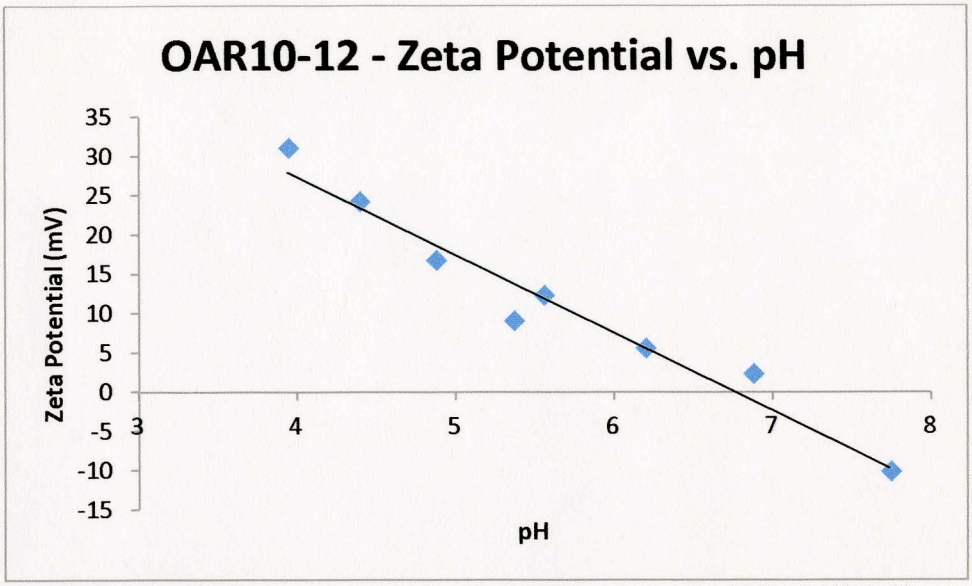

Figure 42: Relationship between measured zeta potential and sample pH for OAR10-12 sample

The relationship between zeta potential and pH was also investigated for sample OAR10-12 (Figure 42), which was used in subsequent coating experiments involving the sand blasted slides and the flask coating. The pH was varied between 3.95-7.75 for this trial. The zeta potential varied between 31.1 mV at pH 3.95 and -10.1 mV at pH 7.75. The linear dependence of the sample's zeta potential on pH depict the same trend as the previously tested sample OAR6, of decreasing zeta potential with increasing solution pH. However, these results for the first time show that the zeta potential can be driven into the negative range at basic pH levels, which is somewhat in line with the work using oleate-free nanoparticles shown by the Capobianco research group[31].

3.3 – Electrophoretic Deposition Experiments

Figure 43: Top Left: Coated ITO slide produced from EPD Trial 2. Top Right: Coated ITO slide produced from EPD Trial 3 Bottom Left: Upconversion luminescence created using small laser spot on EPD Trial 2 slide. Bottom Right: Upconversion luminescence created using small laser spot on EPD Trial 2 slide. Blue coloration of upconversion on slide was an artifact of camera used to capture image.

Using the electrophoretic deposition (EPD) method, two ITO slides were produced with a coating of oleate-free nanoparticles during the 2nd and 3rd EPD trials, using sample OAR8 dispersed in isopropyl alcohol (IPA). Both of these slides are depicted in the top left and right panels of Figure 43. The procedure for the EPD experimentation was modified from the previous report in the literature, in which the optimal conditions for particle deposition onto ITO glass were running the power supply at 200V for 120 seconds, using a 2.5 cm separation distance between the two ITO slides[41]. For both coated slides, the power supply was run at 200V, and the ITO slides acting as the anode and cathode were separated by a 1 inch spacer, producing the following electric field strength,

$$E = (200\ V)/(0.0254\ m) = 7874\ V/m$$

Based on the previous results which showed that the oleate-free nanoparticles had a positive zeta potential at low (acidic) pH conditions, small amounts of 0.1M HCl was added to the solutions to attempt to increase the positive zeta potential of the particles, even though a pH of the isopropyl alcohol solution could not be determined. The concept was to drive the positively charged, oleate-free particles towards the ITO glass that was acting as the cathode when the voltage was induced.

Trial	Sample Used	Dispersant	Sample Diameter (nm)	Volume	pH adjust.	Zeta Potential (mV)
EPD - Trial 1	OAR8	Water	510.2	80mL	4.0	+30.5
EPD - Trial 2	OAR8	IPA	297.5	80mL	n/a	+29.4
EPD - Trial 3	OAR8	IPA	297.5	80mL	n/a	+29.4
EPD - Trial 4	OAR9	IPA	106.5	80mL	n/a	+24.8

Table 3: Information for electrophoretic deposition experiments that were performed.

Table 3 lists data for all EPD trials performed. For EPD trial 1 a current could not be induced through the solutions and the power supply would not run. After reviewing the literature, the subsequent trials were performed with the nanoparticles dispersed in IPA instead of H_2O. Using IPA as the dispersant worked for EPD Trials 2 and 3, but unfortunately a current could not be induced during EPD Trial 4.

For the slide created during EPD Trial 2, the power supply was run continuously for 120 seconds, and for EPD trial 3, the power supply was run continuously for 157 seconds. However, as can be seen from figure 41, the coating on both of these ITO glasses were irregular and inconsistent. In addition to this, while both of the slides exhibited

upconversion luminescence under NIR excitation, the luminescence was dim in comparison to the observed luminescence from the coated carboxylated glasses. This can be seen in the above pictures of both coated ITO slides exhibiting upconversion luminescence. When these glasses were imaged using the final laser/microscope setup for the temperature sensitivity experiments, there was little to no observed luminescence through either the green or red filters. As a result, the focus for the creation of upconverting glasses was shifted to the carboxylated glass experiments, and experimentation with ITO glass and electrophoretic deposition was halted.

3.4 - Carboxylated Glass Deposition Experiments

For the creation of upconverting glasses using the deposition of oleate-free nanoparticles onto carboxylated glass, solutions of oleate-free nanoparticles in water, acetone, and IPA were pipetted onto the glasses at specified volumes. Regardless of dispersant, the oleate-free samples were typically dispersed in volumes of 20 mL, giving an average concentration of,

0.100 g / 0.020 L = 5 g/L

Trial	Sample used	Dispersant	Amount	Carboxylated	Surface
GE1	OAR3	Acetone	100uL	No	Normal
GE2	OAR4	Water	dip method	No	Normal
GE3	Sample 85A	Chloroform	dip method	No	Normal
GE4	OAR6	Acetone	excess	Yes	1 Scratched, 1 Normal
GE5	OAR6	Acetone	excess	Yes	1 Scratched, 1 Normal
GE6	Sample 91B	Chloroform	170uL	Yes	Crosshatch
GE7	OAR7	Water	200uL	Yes	Crosshatch

GE8	OAR7	Water	200uL	Yes	Crosshatch
GE9	OAR9	IPA	200uL	Yes	Normal
GE10	OAR9	IPA	200uL	Yes	Crosshatch
GE11	OAR12	Water	400uL	Yes	Normal
GE12	OAR12	Water	400uL	Yes	Crosshatch
GE13	OAR10-12	Water	200uL	Yes	Sand Blasted
GE14	OAR10-12	Water	200uL	Yes	Sand Blasted
GE15	OAR10-12	Water	200uL	Yes	Sand Blasted
GE16	OAR13	Water	dip method	Yes	Sand Blasted
GE17	OAR13	Water	dip method	Yes	Sand Blasted
GE18	OAR13	Water	dip method	Yes	Sand Blasted
GE19	OAR13	Water	dip method	Yes	Sand Blasted

Table 4: Information for all carboxylated glass deposition experiments that were performed.

Table 4 above depicts all the data for the glass experimentation (GE) coatings that were produced during the course of this experimentation. The initial trials (GE1-GE3) of the coating experimentation were performed with glass slides that had undergone no carboxylation procedure. GE1 was coated via pipetting a solution onto the bare glass, while GE2 and GE3 were coated using a "dipping method", in which the glasses were submerged in the nanoparticle solutions for 24 and 72 hours respectively. While these initial coatings on the glass did produce an upconversion luminescent signal under NIR excitation with the diode laser, the coatings could be easily washed off with small volumes of water delivered via pipette. After this washing there was a dramatic decrease or loss of upconversion signal from the glasses.

The first signs of success came with samples GE4 and GE5, which were coated using sample OAR6 in Acetone. For both trials, 2 glass surfaces were used for each experiment; one that had a crosshatch pattern and was then carboxylated, and one that

had just been carboxylated. An excess amount of the OAR6 solution was pipetted onto the two glass surfaces in each trial, and allowed to dry in the fume hood. When checked with the NIR diode laser, there was a visible upconversion luminescence signal. These glasses also underwent washes with H_2O delivered via pipette, and while it appeared the coating had been removed from portions of the glass, there was still a visible upconversion signal when excitation was provided by the NIR diode laser.

For the remaining experiments, all the glass surfaces that were used for experimentation underwent the carboxylation procedure, with some being etched with a cross-hatch pattern beforehand. The nanoparticle solutions were pipetted onto the surfaces at specific volumes, and were all allowed adequate time to dry in the fume hood.

Figure 44 shows examples of both the unscratched and scratched carboxylated glasses that were coated; Sample GE10 sample and Sample GE12 were scratched in a cross-hatch pattern, while sample GE11 was unscratched.

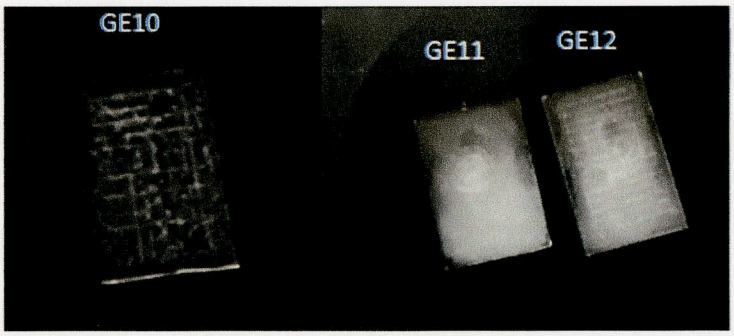

Figure 44: Left: Carboxylated & scratched glass slide Sample GE10, coated using 200μL of OAR9 sample. Right: Sample GE11 on the left, coated using 400μL OAR12 sample. Sample GE12 on the right, coated using 400μL OAR12 sample.

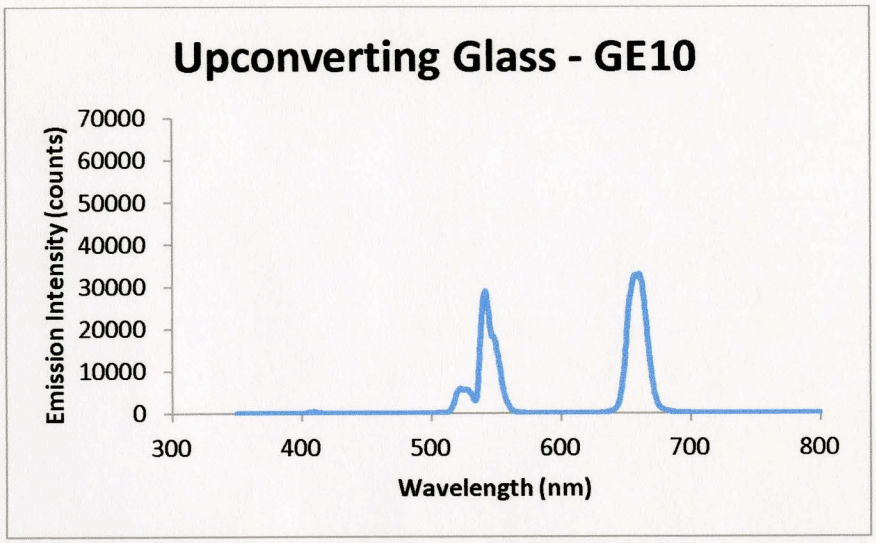

Figure 45: Left: Emission spectra from Glass Sample GE10 exhibiting upconversion luminescence, consistent with that of NaYF4:Er^{3+},Yb^{3+} nanoparticles. 10s integration time.

Many of the upconverting glasses made by this method exhibited bright upconversion under 980nm excitation. The spectral data shown in Figure 45 is from GE10, and is consistent with the spectral data for $NaYF_4$:Er^{3+},Yb^{3+} nanoparticles. GE10 was used extensively in the temperature sensitivity experimentation that followed.

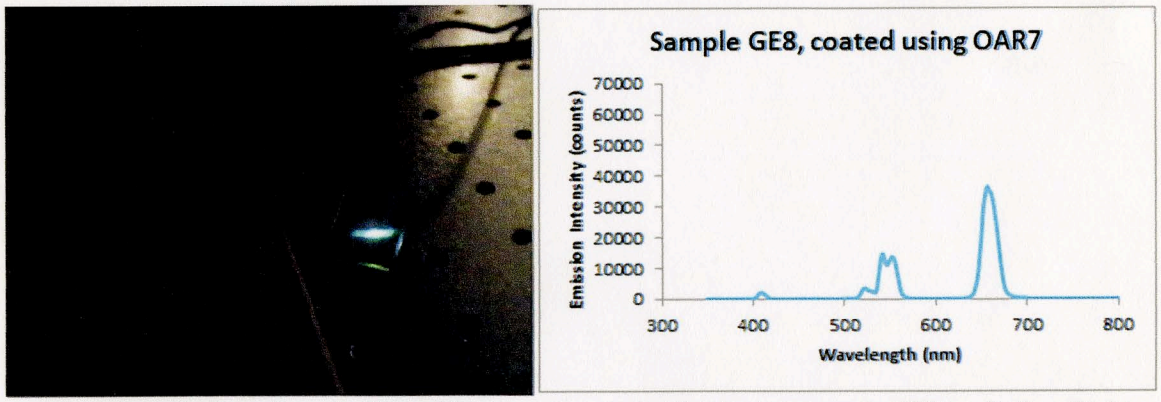

Figure 46: Left: Glass Sample GE8 exhibiting upconversion luminescence under NIR excitation. Right: Spectral data obtained from glass sample GE8, consistent with that of NaYF4:Er^{3+},Yb^{3+} nanoparticles. 100 ms integration time.

Figure 46 depicts Glass Experimentation (GE) sample 8, being held in front of the 980nm diode laser. Spectral data was also obtained from GE8, and is consistent with the spectral data shown in Figure 19 for the original oleate-capped $NaYF_4:Er^{3+},Yb^{3+}$ nanoparticle sample 85A. However, while these glasses exhibited bright upconversion luminescence, the nanoparticle coating was non-homogeneous and appeared irregular under visual inspection.

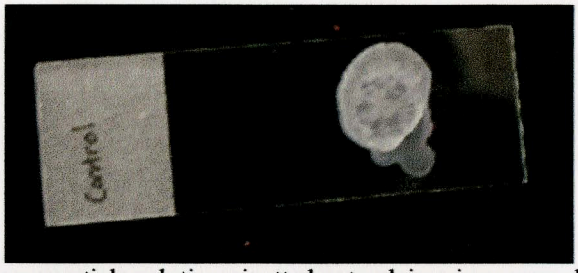

Figure 47: Oleate-capped nanoparticle solution pipetted onto plain microscope slide. Created using 200 uL of Sample 68C $NaYF_4:Er^{3+},Yb^{3+}$ nanoparticles solution

In contrast to nanoparticle coatings created using the oleate-free particles, a coating on a plain glass slide (non-carboxylated) was created using a solution of oleic-acid capped nanoparticles in chloroform. This slide was also used in later temperature sensitivity experimentation, to see whether the oleate coating on the particles caused a marked difference in the Green-to-Red emission ratio observed with varying temperature.

Figure 48: Coated Glass Samples that were initially sand blasted. From Left to Right: Sample GE13, GE14, GE15. All samples were created by using 200uL of sample OAR10-12 solution. However, GE14 was

created using the OAR10-12 solution once the particles had settled on the bottom of the vial, thus creating a layer of NPs on the glass surface at a much high concentration.

In response to the irregular and nonuniform coating of the previous carboxylated slides, sections of microscope slides that had been sand blasted underwent the carboxylation procedure and subsequent nanoparticle coating in the final set of experiments. (Figure 48) Upon visual inspection, the coating on these carboxylated glasses appear to be more homogeneous than their earlier counterparts, and these coated slides exhibited upconversion luminescence under 980nm NIR excitation.

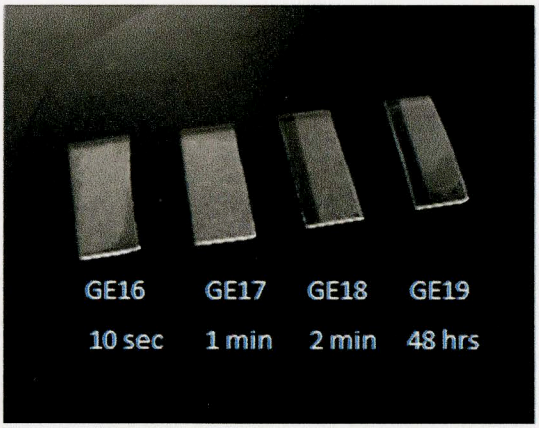

Figure 49: Coated Glass Samples that were initially sand blasted, and were coated using the dipping method. From Left to Right: Sample GE16, GE17, GE18, GE19. All glasses were coated using Sample OAR13, using different deposition times

In contrast to the procedure of creating the nanoparticle coating on the carboxylated glasses via pipette, a set of 4 sandblasted carboxylated glasses were created via a 'dipping' method, where the glasses were dipped into a solution of the oleate-free nanoparticles that was slowly agitated using a stirbar. This experiment was performed to see how well the oleate-free nanoparticles would bind to the carboxylated surface in its presence without being introduced directly to the surface via pipette, which was to be a good indicator of the charged nanoparticles' affinity for the surface functionalization on

the glass samples. Figure 49 above shows the 4 glasses created by this method. Each glass was introduced to the nanoparticle solution for a different length of time; from left to right, 10 seconds, 1 minute, 2 minutes, and 48 hours. However, when these glasses were tested for upconverting nanoparticles on their surfaces with a 980 nm diode laser, no visible upconversion luminescence was observed. Additionally, when images of these glasses were taken using the final laser/microscope setup, no upconversion luminescence was observed. Therefore, these glasses were not used in the subsequent temperature sensitivity experimentation.

3.5 - Temperature Sensitivity - Emission Ratio Curves Using Oleate-capped Nanoparticles in Chloroform

Before the temperature sensitivity experiments involving the nanoparticle-coated glass slides, the emission ratio curves using $NaYF_4:Er^{3+},Yb^{3+}$ in chloroform were constructed for comparison. Through the use of a spectrometer and a temperature-regulated cuvette holder, the dependence on temperature of the three main emission peaks from the particles (521 nm, 541 nm, 668 nm) was demonstrated.

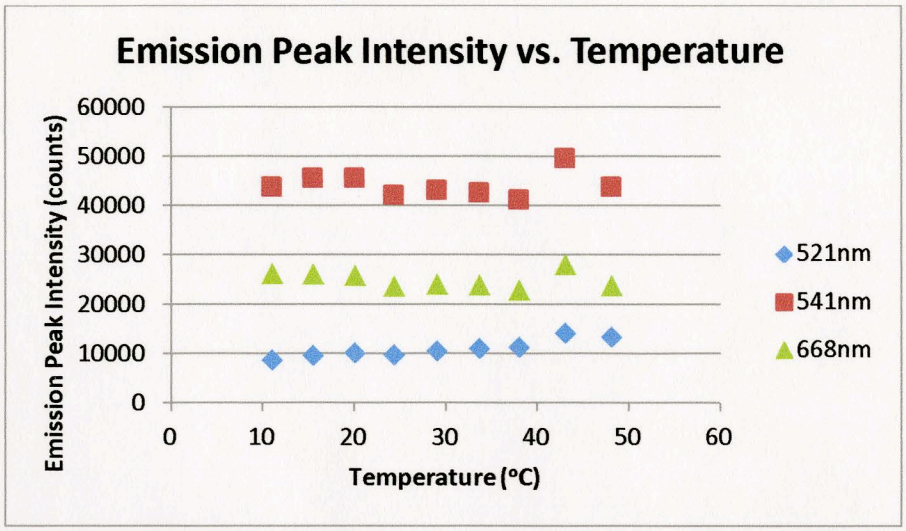

Figure 50. Emission peak intensity dependence on temperature in the range from 10-50°C for the 3 main emission bands in $NaYF_4:Er^{3+},Yb^{3+}$ dispersed in chloroform.

Figure 50 depicts the emission peak intensity of the three emission bands of interest in $NaYF_4:Er^{3+},Yb^{3+}$ nanoparticles as a function of temperature. The emission peak intensity for the 521 nm emission ranged between 8741 and 14242 counts, with the high of 14242 counts at 43°C. The emission peak intensity for the 541nm emission ranged between 41296 and 49637 counts, with the high of 49637 counts at 43°C. The emission peak intensity for the 668 nm emission ranged between 22867 and 28013 counts, with the high of 28013 counts at 43°C. Both the 541 nm and 668 nm emission bands exhibit decreasing emission intensity between 11°C to 38°C, and then increasing emission intensity up to 48.1°C. In contrast, the 521 nm emission band appears to exhibit increasing emission intensity throughout the entire temperature range from 11°C to 48.1°C.

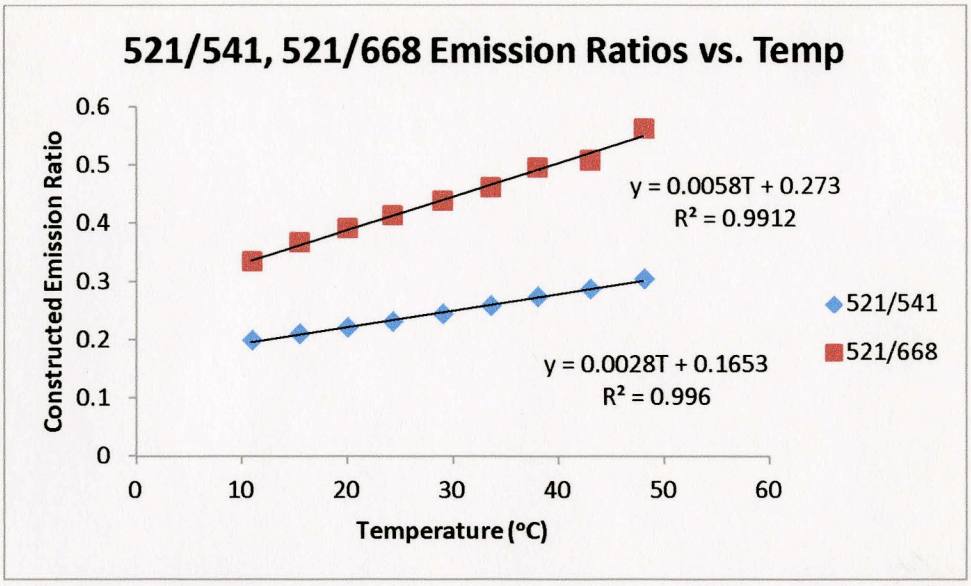

Figure 51. Temperature dependence of the 521 nm/541 nm and 521 nm/668 nm emission band ratios from $NaYF_4:Er^{3+},Yb^{3+}$ dispersed in chloroform.

When the emission ratios for 521 nm/541 nm and 521 nm/668 nm were constructed, there is a well-defined linear relationship between the emission ratios and increasing sample temperature. (Figure 51) For the 521 nm/668 nm ratio, the ratio increased from 0.334 at 11°C to 0.562 at 48.1°C, for an overall ratio change of 0.228. A linear trend line fit to this data resulted in an R^2 value of 0.9912. For the 521 nm/541 nm emission ratio, the ratio increased from 0.199 at 11°C to 0.304 at 48.1°C, for an overall ratio change of 0.105. A linear trend line fit to this data resulted in an R^2 value of 0.996.

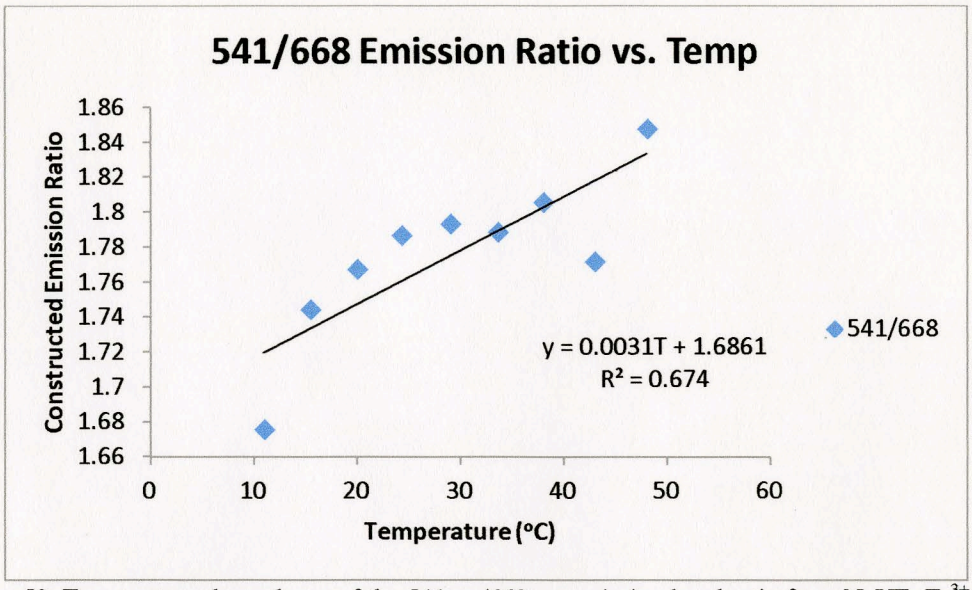

Figure 52. Temperature dependence of the 541nm/668nm emission band ratio from $NaYF_4:Er^{3+},Yb^{3+}$ nanoparticles dispersed in chloroform.

When the emission ratio for the 541 nm/668 nm emission ratio was constructed, the linear dependence on temperature of this ratio is not as well demonstrated. (Figure 52) The 541 nm/668 nm ratio increased from 1.676 at 11°C to 1.848 at 48.1°C, for an overall ratio change of 0.172. A linear trend line fit to this data resulted in an R^2 value of 0.674.

3.6 - Temperature Sensitivity Experiments – Filter Data

For the temperature sensitivity experiments, the objective was to isolate the 521 nm and 668 nm emission bands, and to use those to create the Green-to-Red emission ratio. Two UM-F/XL filter cubes were assembled in conjunction with the Olympus MVX10 microscope to achieve this objective. Each filter cube was comprised of a 900DSCP dichroic mirror and an emission filter. Excitation filters were not necessary as the laser beam was not being directed through the microscope and down onto the stage plate, in contrast to a typical epifluorescence microscopy setup.

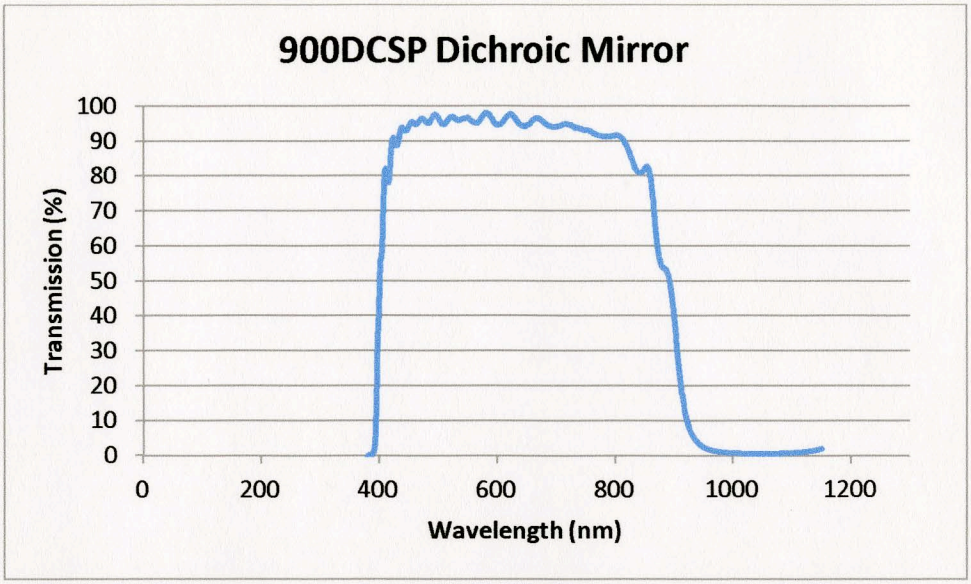

Figure 53: Transmission data for the 900DCSP Dichroic mirror in both filter cubes.

Figure 53 presents the Transmission data for the 900DCSP dichroic mirror, present in both filter cubes. The dichroic allows over 90% transmission between 422 nm – 815 nm, and drops to effectively 1% transmission at 980 nm. Since the main emission bands of interest are all within this range (521nm, 541 nm, and 668 nm), this dichroic was ideal for the experimental setup.

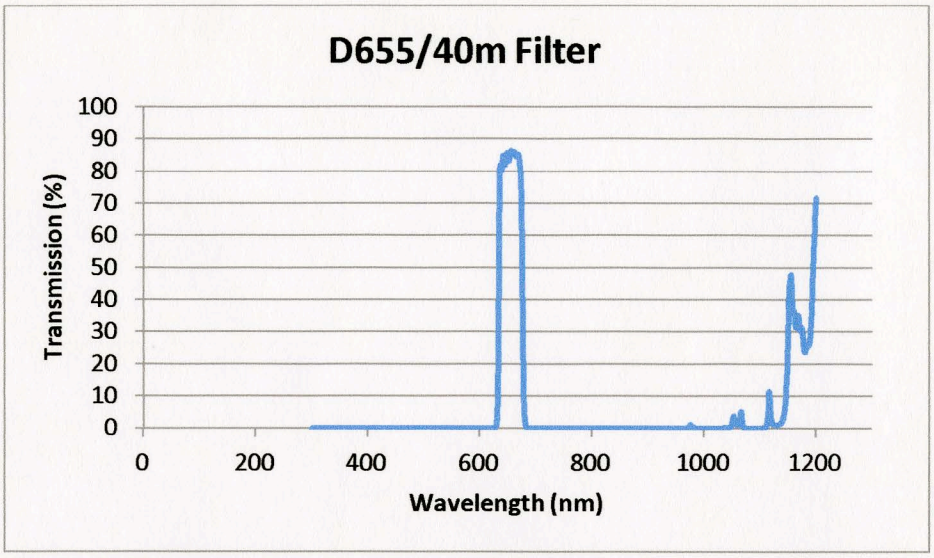

Figure 54: Transmission data for the D655/40m emission filter in the red filter cube.

For the red filter cube, a D655/40m emission filter was chosen to isolate the 668 nm emission band. The transmission data for the filter is shown in Figure 54. The filter allows over 80% transmission over the range of 636 nm – 673 nm, which allows for the capture of the 668 nm emission band. The filter only allows 0.63% transmission at 980 nm.

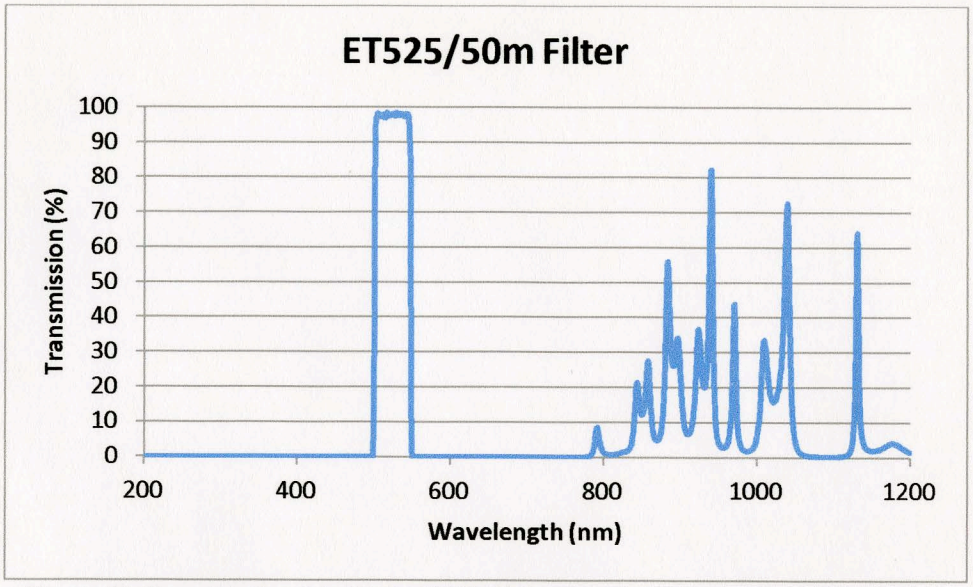

Figure 55: Transmission data for the ET525/50m emission filter in the red filter cube.

For the green filter cube, a ET525/50m emission filter from a GFP filter cube was chosen to isolate the 521 nm emission band. The transmission data for the filter is shown in Figure 55. The filter allows over 80% transmission over the range of 501 nm – 547 nm. Unfortunately the filter transmits varying percentages of light between the range from 800 nm – 1000 nm, with 2.84% transmission at 980nm.

In the following experiments, sets of multiple images were gathered through each filter cube at specific temperature intervals. It was observed that while the measured emission intensities from the coated glass samples through the red filter cube were all within a narrow range, the emission intensities measured through the green filter cube were much more widely distributed, and varied drastically between individual images in each set. There were two main possibilities for this wide distribution of emission intensities, that both deal with the ET525/50m emission filter. The first possibility deals with the transmission range of the emission filter, from 501 nm – 547 nm. While the filter does

decrease the transmission to effectively 0% at 551 nm, this would still allow for the partial transmission of the 541 nm emission band from the $NaYF_4:Er^{3+},Yb^{3+}$ nanoparticles. As was shown in Figures 49-50, the 541nm/668nm ratio does not exhibit a good linear dependence in comparison to the 521nm/668nm ratio. Thus, by using this filter, the green emission that was measured through the green filter cube would be some combination of 521nm and 541nm emission light. The second possibility deals with the increased transmission in the 800 nm – 1000 nm range, specifically at 980 nm. The green filter only allowed for transmission increase in 980nm emission of 2.24% over the red filter. While this increase in transmission percentage is seemingly insignificant, it would be more than enough to overwhelm the weaker upconversion luminescence signal from the nanoparticles on the glass sample.

To correct for the deficiencies of the green filter cube, whenever a set of images were acquired at a specific temperature interval, only the 6 smallest intensity values that were calculated were used. This was done for images taken through both the green and red emission cubes to calculate the Green-to-Red emission ratio.

	Original data set		Corrected	
Trial	**Green**	**Red**	**Green**	**Red**
1	7441	3788	7441	3788
2	7487	3835	7487	3835
3	7856	3840	7856	3840
4	7946	3849	7946	3849
5	7980	3861	7980	3861
6	8368	3863	8368	3863
7	8407	3866		
8	8440	3885		
9	8559	3889		

10	8626	3889		
11	8666	3889		
12	8762	3899		
13	10396	3944		
14	10753	3990		
15	12235	4037		
16	12338	4103		
Average	9016.3	3901.7	7846.3	3839.3
StDev	1507.7	78.1	314.5	25.1
StError	376.9	19.5	128.4	7.2

Table 5: Emission intensity data through both the green and red emission cubes for Sample GE14, at 35.1°C. Excel calculations of the average emission intensity, standard deviation, and standard error are also shown.

An example of this correction is shown in Table 5, performed for sample GE14 at 35.1°C. When using all 16 intensity values from all images collected in each data set, the green emission intensity ranges between 7441-12338 counts. The average emission intensity is 9016.3 counts, which has a standard deviation of 1507.7 (16.7%) and a standard error of 376.9 (4.18%). In comparison, the red emission intensity ranges between 3788-4103 counts. The average emission intensity is 3901.6, which has a standard deviation of 78.1 (2.00%) and a standard error of 19.5 (0.50%).

In contrast, when using only the lowest 6 intensity values, the green emission intensity ranges between 7441-8368 counts. The average green emission intensity is 7846.3 counts, which has a standard deviation of 314.5 (4.01%) and a standard error of 128.4 (1.64%). The red emission intensity ranges between 3788-3863 counts. The average red emission intensity is 3839.3 counts, with a standard deviation of 25.1 (0.65%) and a standard error of 7.2 (0.19%).

When comparing the average intensity values for the red emission between the two different sized data sets, there is only a 1.60% change in using the lowest 6 emission intensity values rather than 16 values. The standard deviation of the data set decreases by 67.9%, while the standard error decreases by 62.9%.

For the green emission, there is a 13.0% change in using the lowest 6 emission intensity values for the average green emission value rather than 16 values. The standard deviation of the data set decreases by 79.1%, and the standard error decreases by 66.0%.

3.7 – Temp. Sensitivity Experiment 1 – Sample GE10, using OPO Laser Triggered by Pulse Generator

The first temperature sensitivity experiment was performed using Sample GE10, and the 3 ns OPO laser, directed down onto the microscope stage plate using a set of mirrors and a dichroic mirror directly in front of the microscope objective lens to direct the beam down onto the stage plate. A 100 μs delay was set using the pulse generator so that the 980 nm excitation light would not be present in the collected images. The temperature of the slide was varied from 20°C to 45°C, with images taken at 5°C temperature intervals. For this trial, only 1 image was taken through each of the green and red filter cubes for each temperature interval, using an exposure time of 60 seconds. No background subtraction was performed on the images. An area of 10625 pixels was used to measure the average emission intensity from the upconverting glass at each temperature interval. Since the emission from the glass did not encompass the entire field of view, the pixel area used was positioned over a specific area of interest where the emission was present.

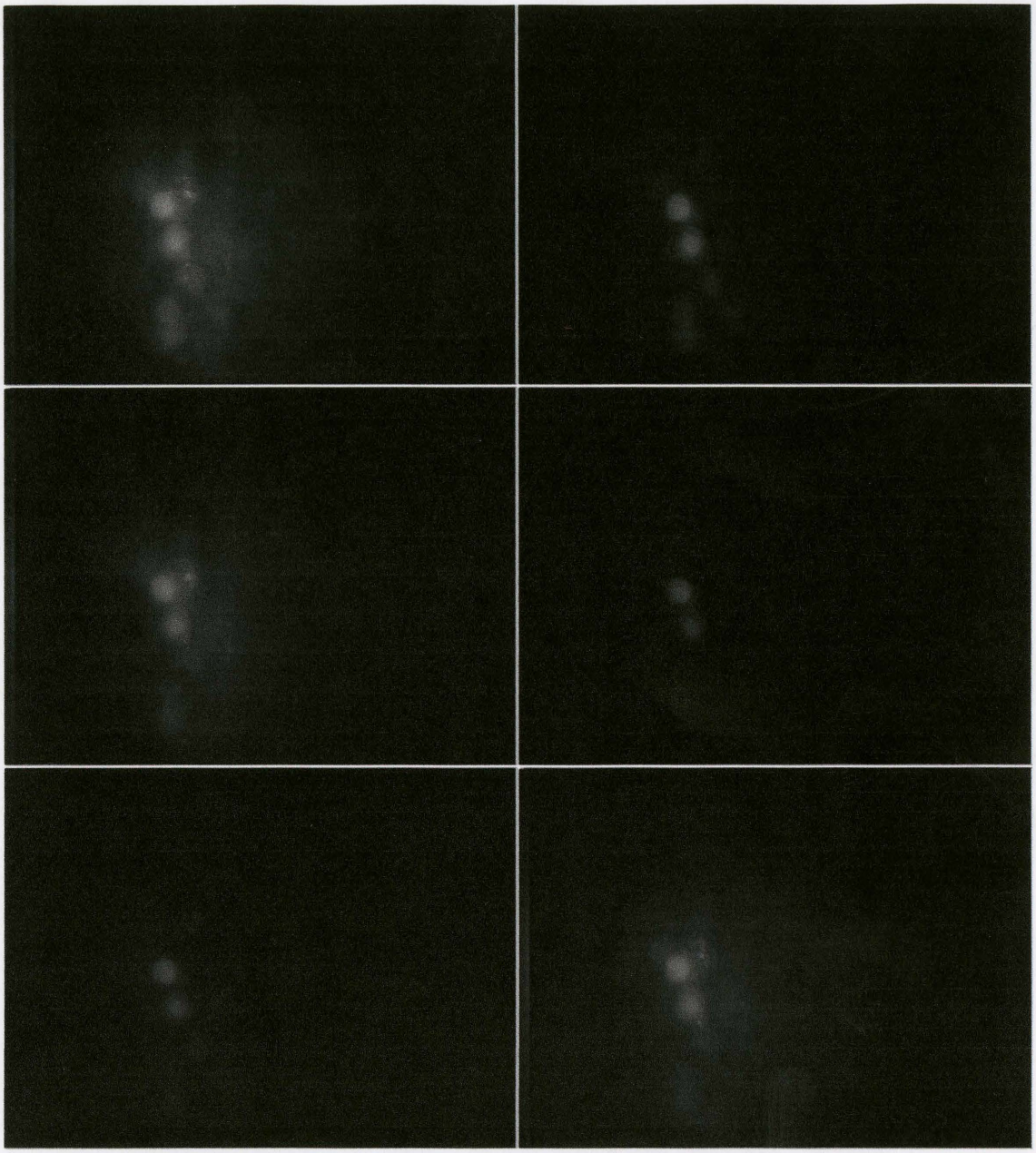

Figure 56: Images taken during initial temperature sensitivity trial using GE10. Top left: Image through GFP filter at 20°C. Top Right: Image through D660 filter at 20°C. Middle left: Image through GFP filter at 30°C. Middle Right: Image through D660 filter at 30°C. Bottom Left: Image through GFP filter at 40°C. Bottom Right: Image through D660 filter at 40°C.

Figure 56 depicts some of the images that were obtained using this laser/microscope system. As can be clearly seen above, the images corresponding to both the green and red

emission from the glass sample were out of focus and unclear. This was partly due to the fact that the microscope objective lens was impeded by the dichroic mirror in front of it, and could not be adjusted properly.

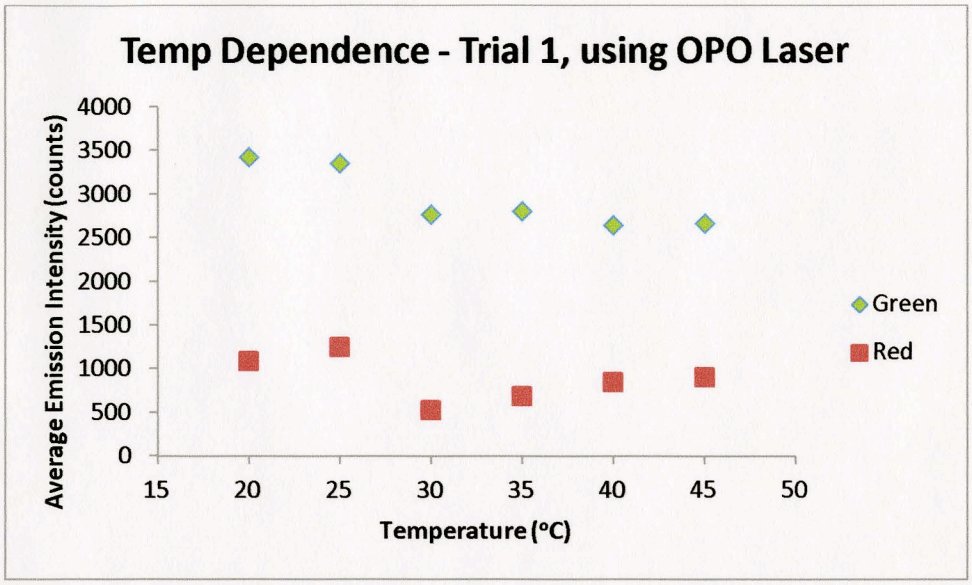

Figure 57. First experimental trial to determine temperature dependence of coated glass surfaces. This figure depicts the average emission intensity of the green and red emission bands with respect to temperature. Sample GE10 was used.

Figure 57 depicts the average emission intensity of both the green and red emission with varying temperature. The green emission decreased from 3427 counts at 20°C to 2666 counts at 45°C. The red emission initially increases between 20°C-25°C, from 1087 to 1249 counts, and then sharply drops to 524 counts at 30°C. It eventually increases to 904 counts at 45°C.

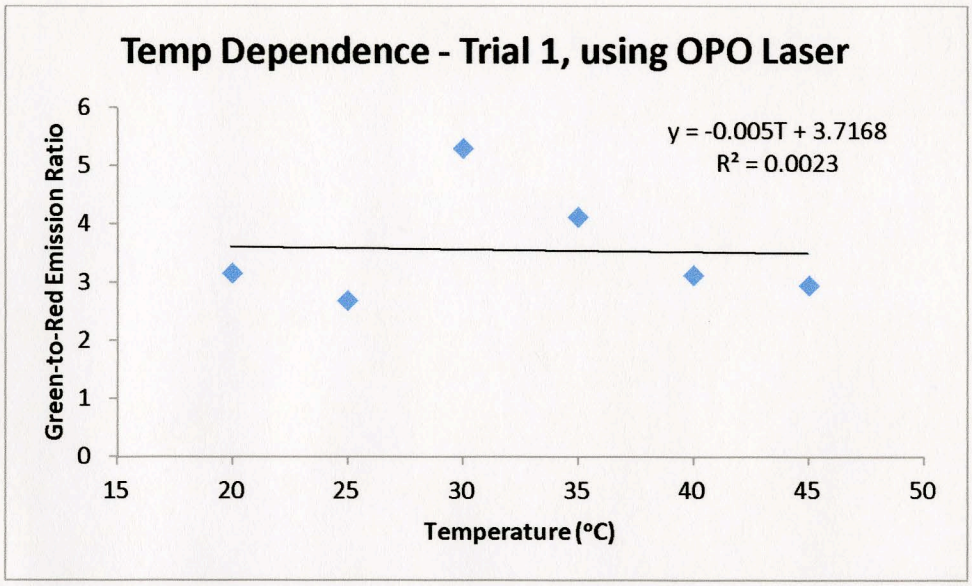

Figure 58. First experimental trial to determine temperature dependence of coated glass surfaces. This figure depicts the ratiometric temperature dependence of the green-to-red emission ratio from the nanoparticles on the glass surface. Sample GE10 was used. During this trial, the CCD camera was triggered using a pulse generator, and the OPO was used as the excitation source

When the Green-to-Red Emission ratio is constructed, there is no linear dependence shown. The ratio initially decreases from 3.152 at 20°C to 2.688 at 25°C, and then increases sharply to 5.290 at 30°C. It then decreases to 2.950 at 45°C. A linear trend line fit to this data resulted in an R^2 value of 0.0023, indicative of no linear relationship demonstrated by the data.

3.8 - Temperature Sensitivity Experiment 2 – Sample GE10, using Diode Laser

The second temperature sensitivity experiment was performed using Sample GE10, and the 980 nm diode laser. The laser beam was directed to the sample using a fiber optic cable with attached lens. The camera was triggered by the laser pulse, using a pulse width of 100 μs and 1350 mA intensity, so that the 980 nm excitation light would not be present in the collected images. The temperature of the slide was varied from 20.8°C to 60°C,

with the aim of taking images at 5°C temperature intervals. For this trial, the 6 lowest emission intensities from the image sets were used from each of the green and red filter cubes for each temperature interval, using an exposure time of 20 seconds. No background subtraction was performed on the images. An area of 10625 pixels was used to measure the average emission intensity from the upconverting glass at each temperature interval. Since the emission from the glass did not encompass the entire field of view, the pixel area used was positioned over a specific area of interest where the emission was present.

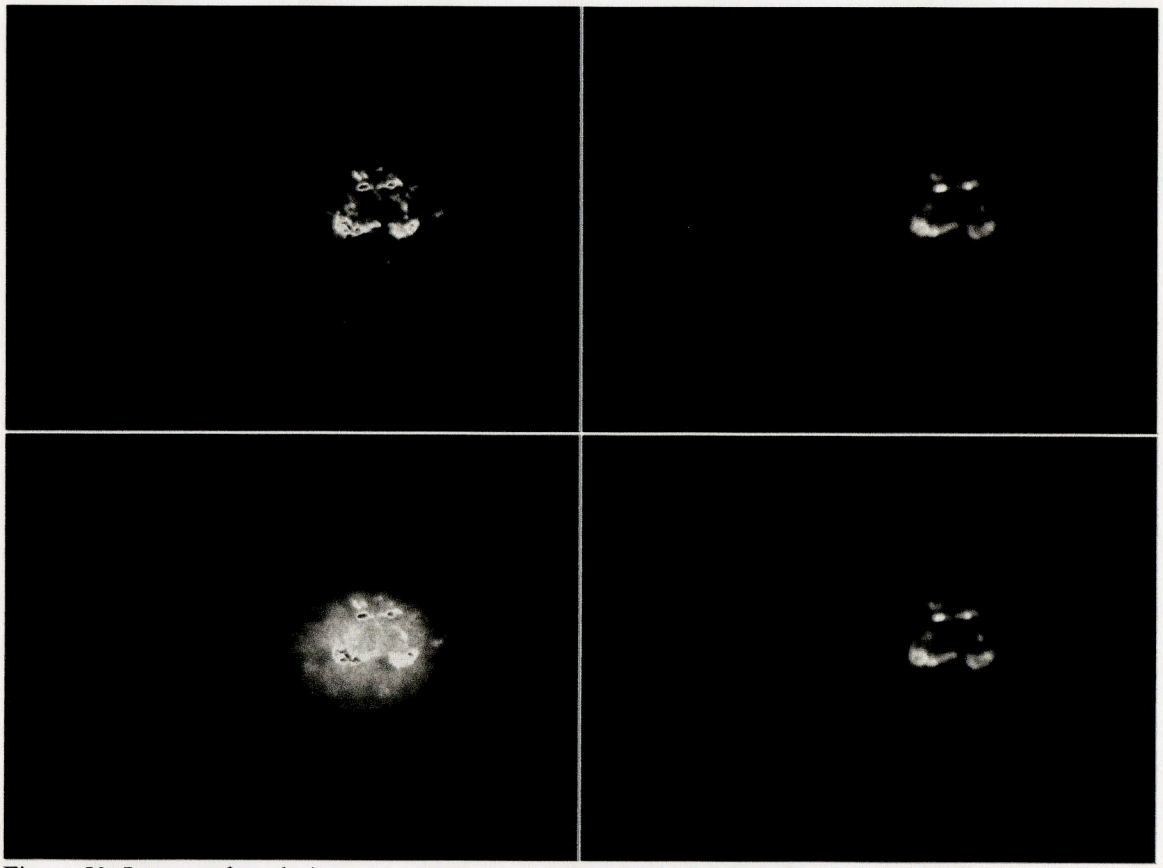

Figure 59: Images taken during temperature sensitivity trial 2 of GE10. Top left: Image through GFP filter at 20.8°C. Top Right: Image through D660 filter at 20.8°C. Bottom Left: Image through GFP filter at 35°C. Bottom Right: Image through D660 filter at 35°C.

Figure 59 depicts some of the images that were obtained during the temperature sensitivity trial. The images corresponding to both the green and red emission from the glass sample appear to be better focused than the experiment. This was partly due to the fact that the microscope objective lens was no longer impeded by the dichroic mirror, and the laser beam was directed straight towards the upconverting glass sample using the fiber optic and lens.

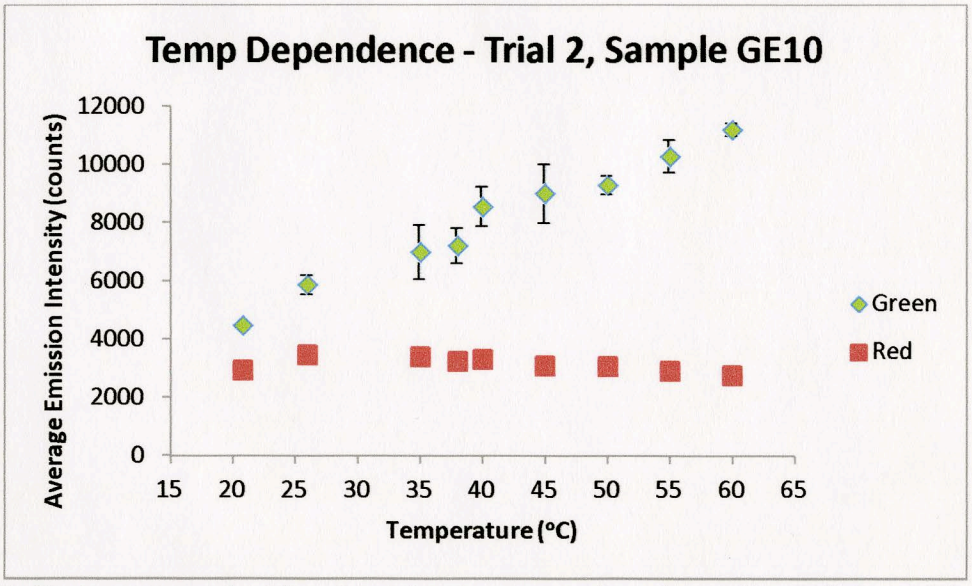

Figure 60. First experimental trial to determine temperature dependence of coated glass surfaces. This figure depicts average emission intensity from both green and red emission bands for each temperature interval. Sample GE10 was used for this experiment.

Figure 60 depicts the average emission intensity of both the green and red emission from the sample with varying temperature. An overall increasing trend that was observed for the average green emission intensity, from 4461.2 counts at 20.8°C to 11191.8 counts at 60°C, for an overall intensity change of 6730.6 counts. The largest standard deviation was calculated to be 1010.4 counts at 45°C, with a standard error of 412.5 counts. The red

emission initially increases between 20.8°C-26°C, from 2908 counts to 3434.2 counts, and then decreases to 2728.8 counts at 60°C. The largest standard deviation was calculated to be 92.9 counts at 55°C, with a standard error of 37.9 counts.

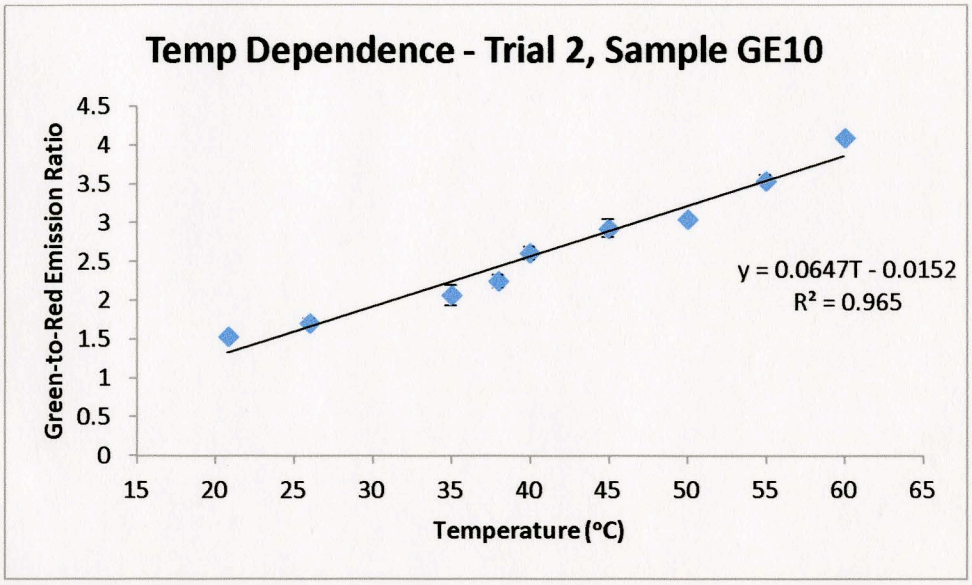

Figure 61. Second experimental trial to determine temperature dependence of coated glass surfaces. This figure depicts the ratiometric temperature dependence of the green-to-red emission ratio from the nanoparticles on the glass surface. Sample GE10 was used for this experiment.

When the Green-to-Red Emission ratio was constructed, there was a clear linear dependence shown. The ratio increases from 1.534 at 20.8°C to 4.101 at 60°C, for an overall ratio change of 2.567. The largest standard deviation was calculated to be 0.135 at 35°C, with a standard error of 0.055. A linear trend line fit to this data resulted in an R^2 value of 0.965, indicative of a linear relationship.

3.9 - Temperature Sensitivity Experiment 3 – Sample GE10

The third temperature sensitivity experiment was performed using Sample GE10, and the 980 nm diode laser. The laser beam was again directed to the sample using a fiber optic

cable with attached lens, but the position of the lens had changed. The camera was triggered by the laser pulse, using a pulse width of 100 μs and 1350 mA intensity, so that the 980 nm excitation light would be at a minimum in the collected images. The temperature of the slide was varied from 20.6°C to 50°C, with the aim of taking images at 5°C temperature intervals. For this trial, the 6 lowest emission intensities from the image sets were used from each of the green and red filter cubes for each temperature interval, using an exposure time of 30 seconds. Background subtraction was performed on all of the images to improve accuracy. An area of 16906 pixels was used to measure the average emission intensity from the upconverting glass at each temperature interval. The pixel area was adjusted to accommodate for a larger laser spot size since the fiber optic lens position had changed. Since the emission from the glass did not encompass the entire field of view, the pixel area used was positioned over a specific area of interest where the emission was present.

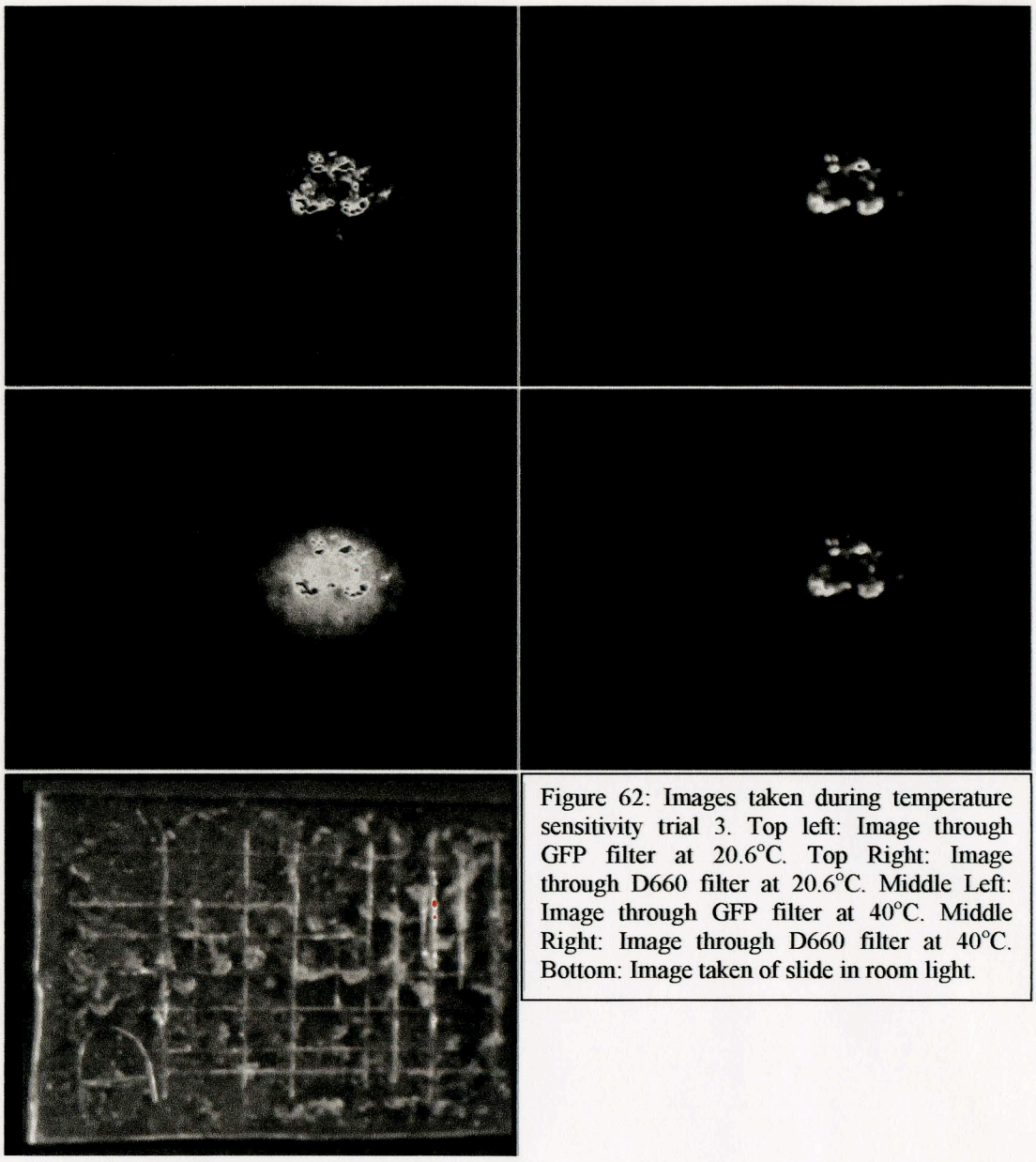

Figure 62: Images taken during temperature sensitivity trial 3. Top left: Image through GFP filter at 20.6°C. Top Right: Image through D660 filter at 20.6°C. Middle Left: Image through GFP filter at 40°C. Middle Right: Image through D660 filter at 40°C. Bottom: Image taken of slide in room light.

Figure 62 depicts some of the images that were obtained during the temperature sensitivity trial. The images corresponding to both the green and red emission from the glass sample again appear to be better focused than the initial temperature sensitivity

experiment. An image of sample GE10 under the microscope in room light conditions was also taken, using no filter and a 1 second exposure time.

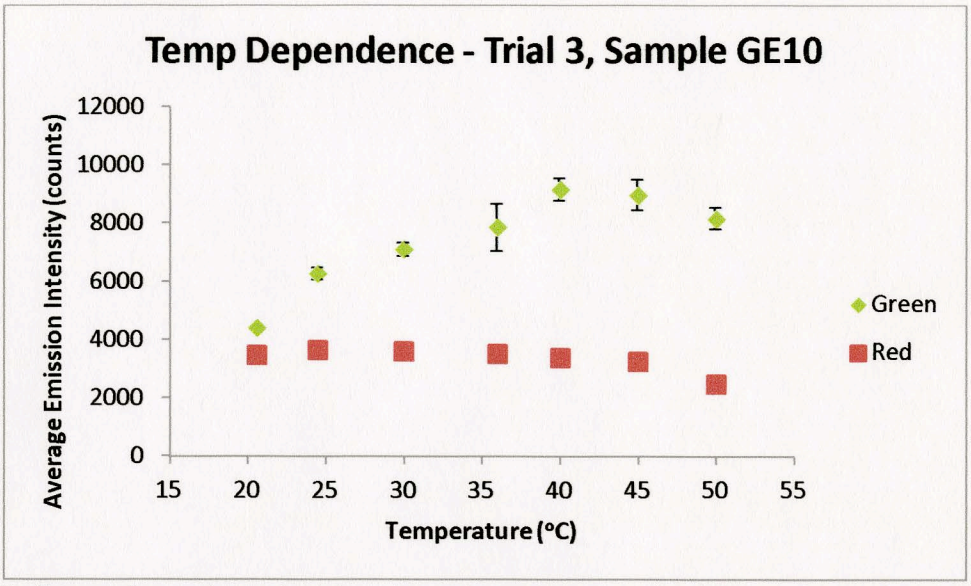

Figure 63. Repeated experimental trial to determine temperature dependence of coated glass surfaces, sample GE910 was again used in this trial. This figure depicts average emission intensity from both green and red emission bands for each temperature interval.

Figure 63 depicts the average emission intensity of both the green and red emission from the sample with varying temperature. For the green emission, the average intensity increased from 4393.8 counts at 20.6°C to 9161 counts at 40°C, and then decreased to 8163.5 counts at 50°C. The largest standard deviation was calculated to be 818.8 counts at 36°C, with a standard error of 334.3 counts. For the red emission, the average intensity stayed relatively constant, from 3450.7 counts at 20.6°C to 3239.4 counts at 45°C. The average intensity did decrease at 50°C to 2464.0 counts. The largest standard deviation was calculated to be 58.8 counts at 30°C, with a standard error of 24.0 counts.

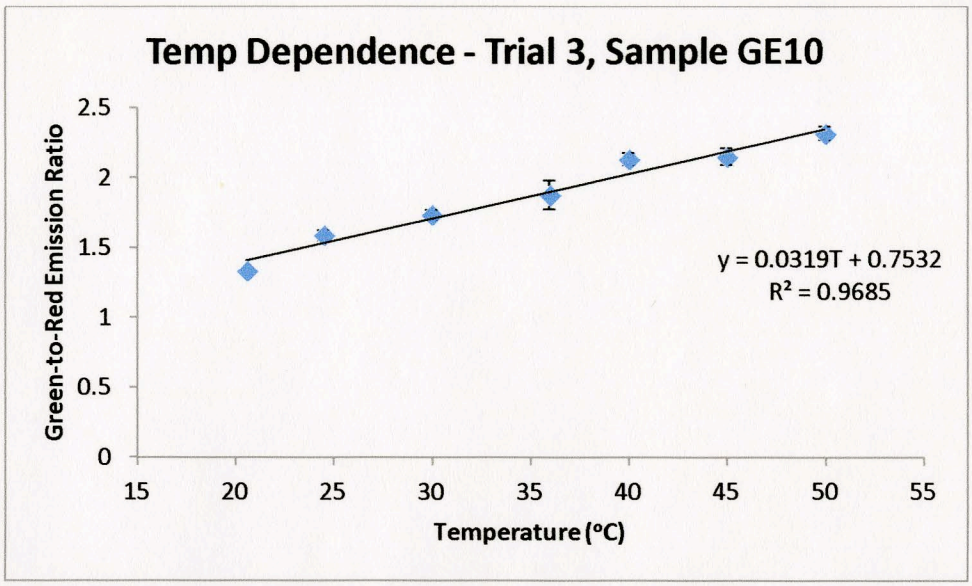

Figure 64. Repeated experimental trial to determine temperature dependence of coated glass surfaces, sample GE10 was again used in this trial. This figure depicts the ratiometric temperature dependence of the green-to-red emission ratio from the nanoparticles on the glass surface.

When the Green-to-Red Emission ratio was constructed, there was a clear linear dependence shown. The ratio increases from 1.334 at 20.6°C to 2.315 at 50°C, for an overall ratio change of 0.981. The largest standard deviation was calculated to be 0.105 at 36°C, with a standard error of 0.043. A linear trend line fit to this data resulted in an R^2 value of 0.9685, indicative of a linear relationship.

3.10 - Temperature Sensitivity Experiment 4 – Sample GE14

The fourth temperature sensitivity experiment was performed using Sample GE14, and the 980 nm diode laser. The laser beam was again directed to the sample using a fiber optic cable with attached lens, but the position of the lens had changed. The camera was triggered by the laser pulse, using a pulse width of 100 µs and 1350 mA intensity, so that the 980 nm excitation light would be at a minimum in the collected images. The

temperature of the slide was varied from 20.5°C to 50°C, with the aim of taking images at 5°C temperature intervals. For this trial, the 6 lowest emission intensities from the image sets were used from each of the green and red filter cubes for each temperature interval, using an exposure time of 10 seconds. Background subtraction was performed on all of the images to improve accuracy. An area of 10625 pixels was used to measure the average emission intensity from the upconverting glass at each temperature interval. The pixel area was adjusted to accommodate for a smaller laser spot size since the fiber optic lens position had changed. Since the emission from the glass did not encompass the entire field of view, the pixel area used was positioned over a specific area of interest where the emission was present.

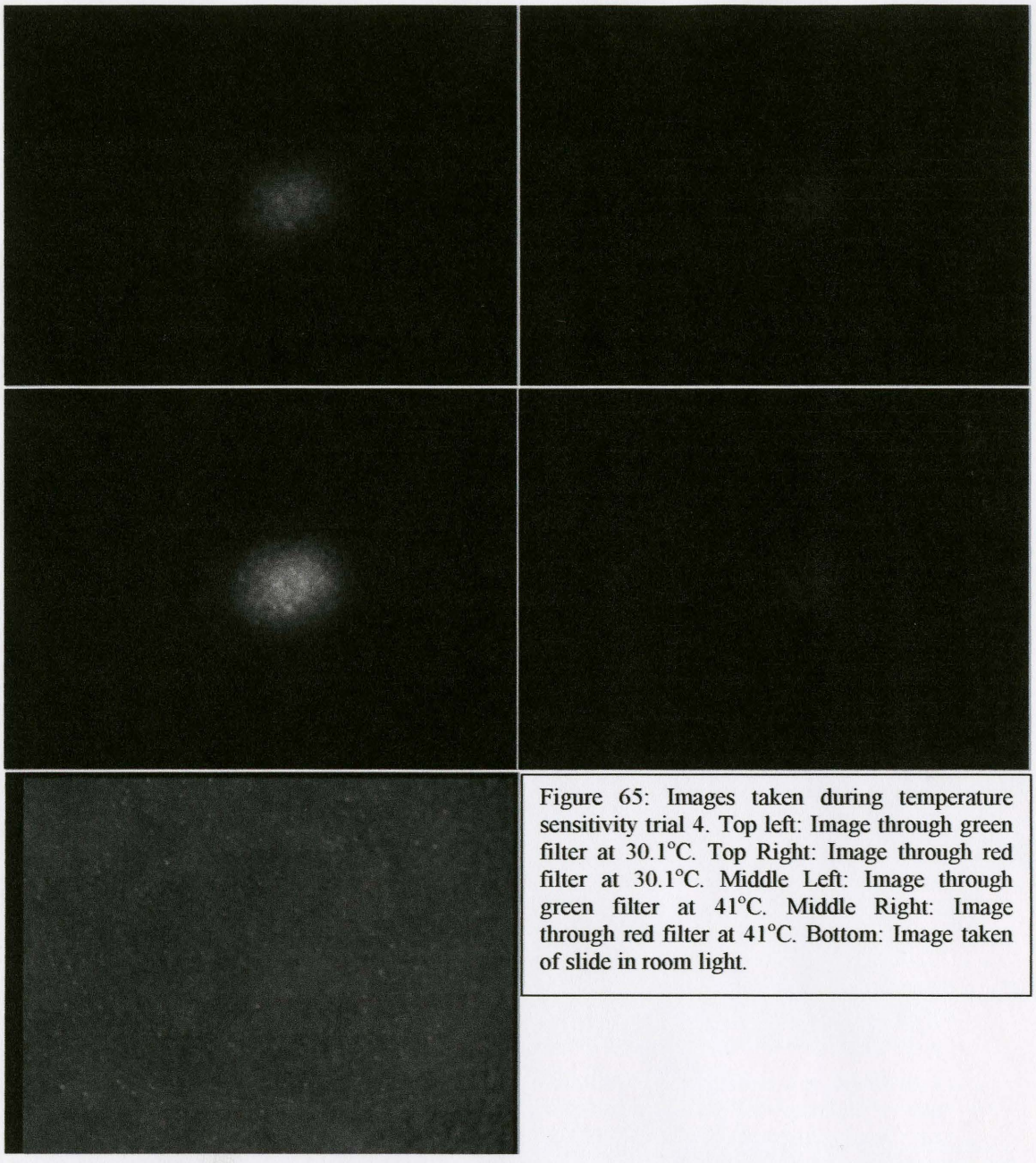

Figure 65: Images taken during temperature sensitivity trial 4. Top left: Image through green filter at 30.1°C. Top Right: Image through red filter at 30.1°C. Middle Left: Image through green filter at 41°C. Middle Right: Image through red filter at 41°C. Bottom: Image taken of slide in room light.

Figure 65 depicts some of the images that were obtained during the 4th temperature sensitivity trial. The images corresponding to both the green and red emission from the glass sample again appear to be better focused than the initial temperature sensitivity

experiment. An image of sample GE14 under the microscope in room light conditions was also taken, using no filter and a 1 second exposure time. The coating on the glass surface appears to be visually more uniform.

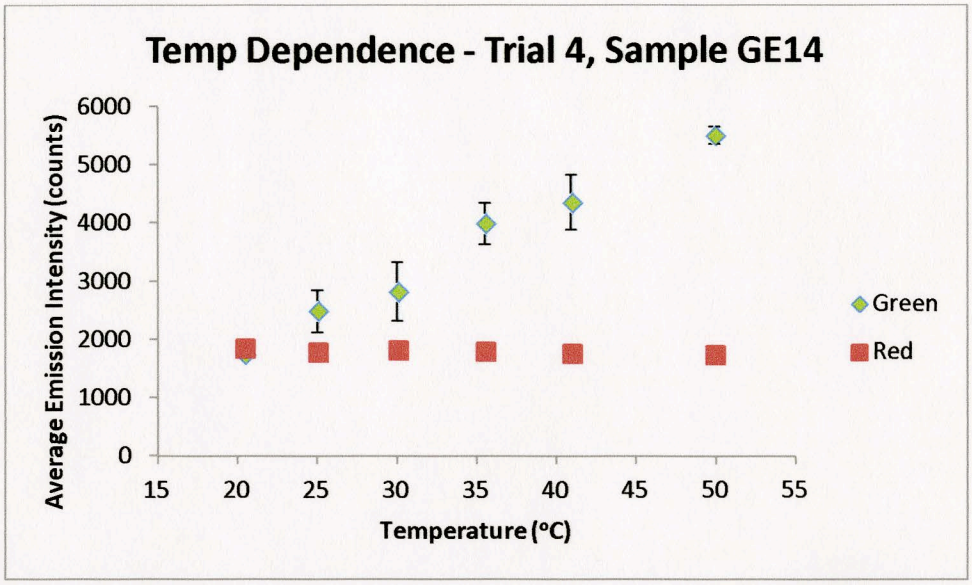

Figure 66. Experimental Trial to determine temperature dependence of coated glass surfaces that had initially been sand-blasted. Sample GE14 was used in this trial. This figure depicts average emission intensity from both green and red emission bands for each temperature interval.

Figure 66 above depicts the average emission intensity of both the green and red emission from the sample with varying temperature. For the green emission, the average intensity increased over the entire range of temperatures, from 584.3 counts at 20.5°C to 4342.3 counts at 50°C. The largest standard deviation was calculated to be 501.0 counts at 30.1°C, with a standard error of 204.5 counts. For the red emission, the average intensity decreased slightly over the temperature range, from 719.3 counts at 20.5°C to 605.7 counts at 50°C. The largest standard deviation was calculated to be 8.20 counts at 50°C, with a standard error of 3.35 counts.

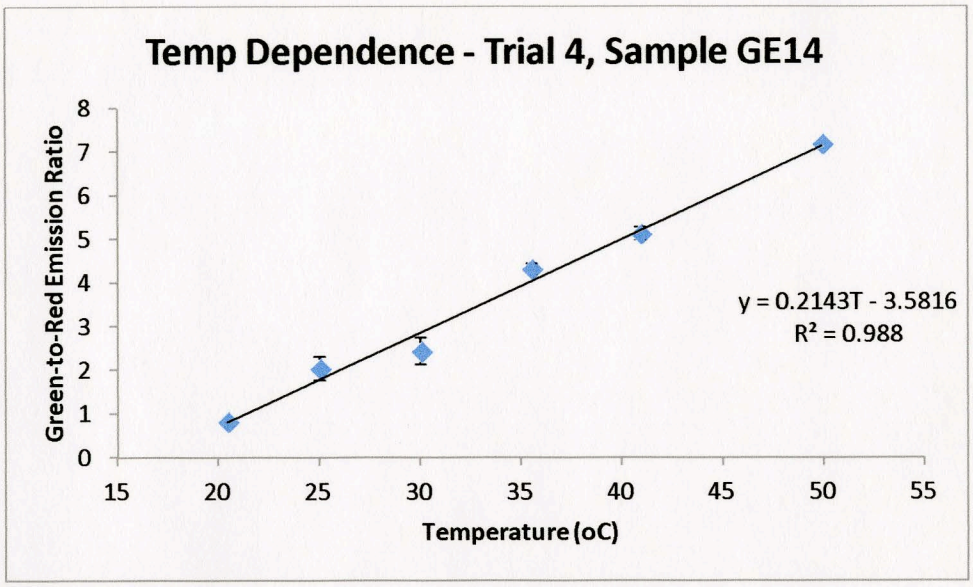

Figure 67. Experimental Trial to determine temperature dependence of coated glass surfaces that had initially been sand-blasted. Sample GE14 was used in this trial. This figure depicts the ratiometric temperature dependence of the green-to-red emission ratio from the nanoparticles on the glass surface.

When the Green-to-Red Emission ratio was constructed, there was a clear linear dependence shown. The ratio increases from 0.81 at 20.5°C to 7.17 at 50°C, for an overall ratio change of 6.36. The largest standard deviation was calculated to be 0.302 at 30.1°C, with a standard error of 0.123. A linear trend line fit to this data resulted in an R^2 value of 0.988, indicative of a linear relationship.

3.11 - Temperature Sensitivity Experiment 5 – Sample GE14

The fifth temperature sensitivity experiment was performed using Sample GE14, and the 980 nm diode laser. The laser beam was again directed to the sample using a fiber optic cable with attached lens, but the position of the lens had changed. The camera was triggered by the laser pulse, using a pulse width of 100 μs and 1350 mA intensity, so that the 980 nm excitation light would be at a minimum in the collected images. The

temperature of the slide was varied from 21.0°C to 45.2°C, with the aim of taking images at 5°C temperature intervals. For this trial, the 6 lowest emission intensities from the image sets were used from each of the green and red filter cubes for each temperature interval, using an exposure time of 10 seconds. Background subtraction was performed on all of the images to improve accuracy. An area of 6900 pixels was used to measure the average emission intensity from the upconverting glass at each temperature interval. The pixel area was adjusted to accommodate for the laser spot size since the fiber optic lens position had changed. Since the emission from the glass did not encompass the entire field of view, the pixel area used was positioned over a specific area of interest where the emission was present.

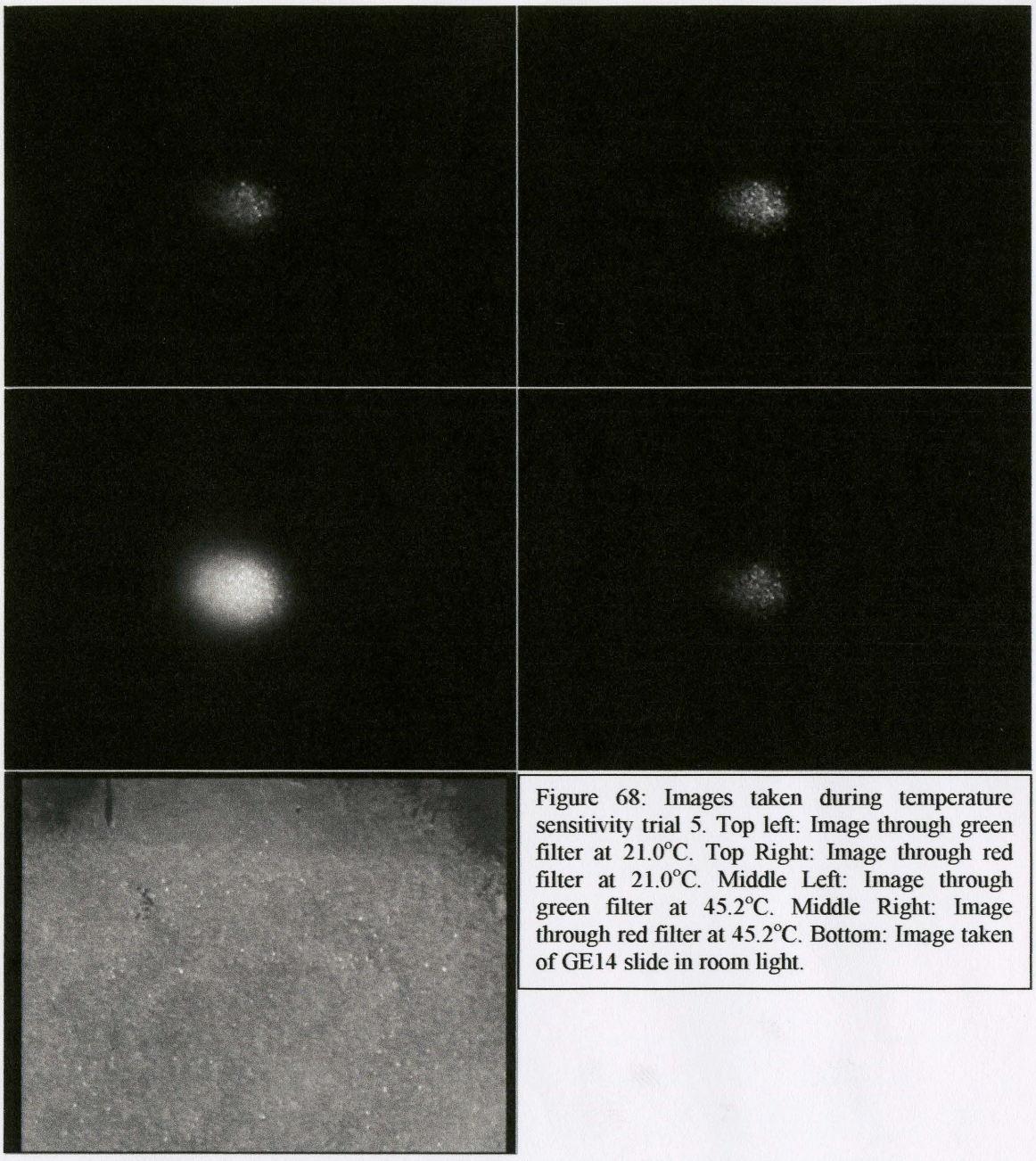

Figure 68: Images taken during temperature sensitivity trial 5. Top left: Image through green filter at 21.0°C. Top Right: Image through red filter at 21.0°C. Middle Left: Image through green filter at 45.2°C. Middle Right: Image through red filter at 45.2°C. Bottom: Image taken of GE14 slide in room light.

Figure 68 depicts some of the images that were obtained during the 5th temperature sensitivity trial. An image of sample GE14 under the microscope in room light conditions

was also taken, using no filter and a 1 second exposure time. The coating on the glass surface appears to be visually more uniform.

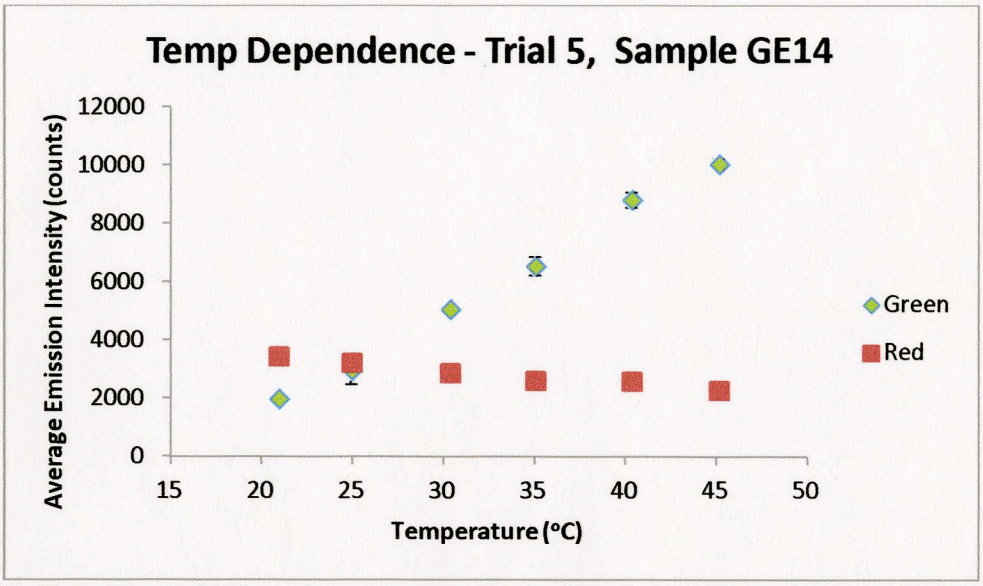

Figure 69. Experimental Trial to determine temperature dependence of coated glass surfaces that had initially been sand-blasted. Sample GE14 was used in this trial. This figure depicts average emission intensity from both green and red emission bands for each temperature interval.

Figure 69 depicts the average emission intensity of both the green and red emission from the sample with varying temperature. For the green emission, the average intensity increased over the entire range of temperatures, from 1963.5 counts at 21.0°C to 10034.3 counts at 45.2°C. The largest standard deviation was calculated to be 505.1 counts at 25.0°C, with a standard error of 206.2 counts. For the red emission, the average intensity decreased over the same temperature range, from 3406.2 counts at 21.0°C to 2251.7 counts at 45.2°C. The largest standard deviation was calculated to be 32.84 counts at 45.2°C, with a standard error of 13.41 counts.

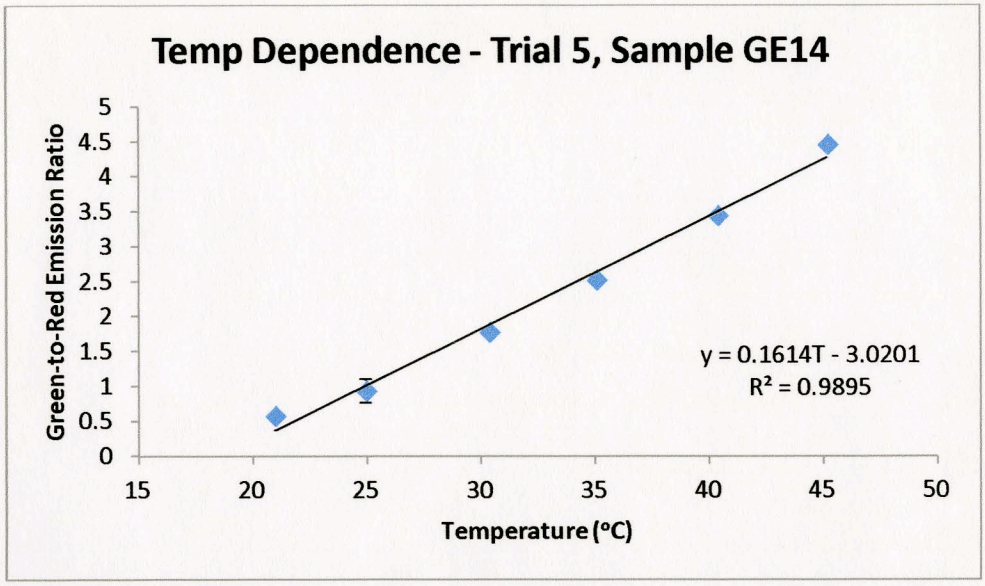

Figure 70. Experimental Trial to determine temperature dependence of coated glass surfaces that had initially been sand-blasted. Sample GE14 was used in this trial. This figure depicts the ratiometric temperature dependence of the green-to-red emission ratio from the nanoparticles on the glass surface.

When the Green-to-Red Emission ratio was constructed, there was a clear linear dependence shown. The ratio increases from 0.58 at 21.0°C to 4.46 at 45.2°C, for an overall ratio change of 3.88. The largest standard deviation was calculated to be 0.171 at 25.0°C, with a standard error of 0.0091. A linear trend line fit to this data resulted in an R^2 value of 0.9895, indicative of a linear relationship.

3.12 - Temperature Sensitivity Experiment 6 – OA-capped NPs on Glass

The sixth temperature sensitivity experiment was performed using the plain glass sample coated with oleate-capped $NaYF_4:Er^{3+},Yb^{3+}$ nanoparticles, and the 980 nm diode laser. The laser beam was again directed to the sample using a fiber optic cable with attached lens, but the position of the lens had changed. The camera was triggered by the laser pulse, using a pulse width of 100 µs and 1350 mA intensity, so that the 980 nm excitation

light would be at a minimum in the collected images. The temperature of the slide was varied from 20.6°C to 50.2°C, with the aim of taking images at 5°C temperature intervals. For this trial, the 6 lowest emission intensities from the image sets were used from each of the green and red filter cubes for each temperature interval, using an exposure time of 10 seconds. Background subtraction was performed on all of the images to improve accuracy. An area of 10625 pixels was used to measure the average emission intensity from the upconverting glass at each temperature interval. The pixel area was adjusted to accommodate for the laser spot size since the fiber optic lens position had changed. Since the emission from the glass did not encompass the entire field of view, the pixel area used was positioned over a specific area of interest where the emission was present.

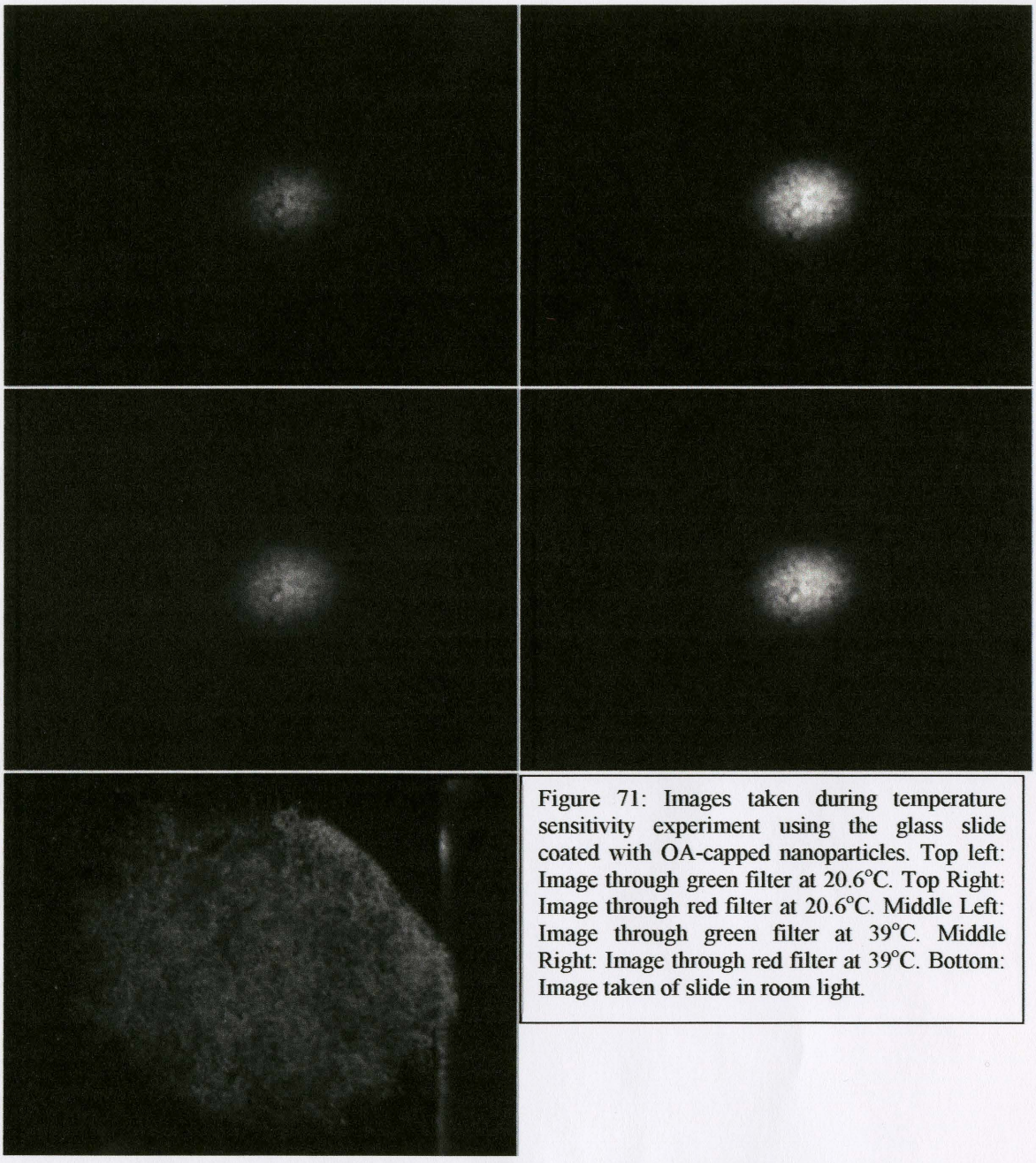

Figure 71: Images taken during temperature sensitivity experiment using the glass slide coated with OA-capped nanoparticles. Top left: Image through green filter at 20.6°C. Top Right: Image through red filter at 20.6°C. Middle Left: Image through green filter at 39°C. Middle Right: Image through red filter at 39°C. Bottom: Image taken of slide in room light.

Figure 71 depicts some of the images that were obtained during the 6th temperature sensitivity trial. An image of the sample under the microscope in room light conditions

was taken, using no filter and a 1 second exposure time. The coating on the glass surface appears to be visually non-uniform.

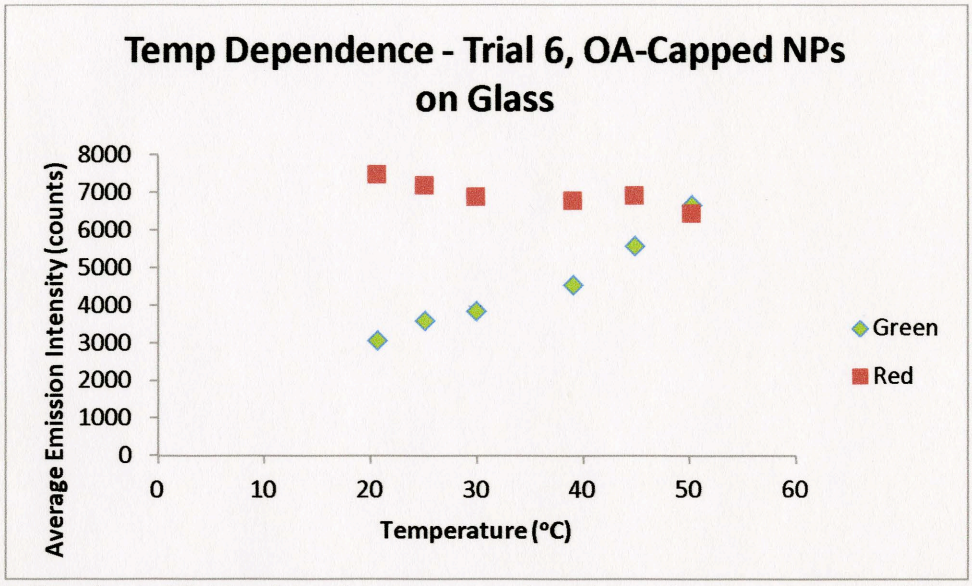

Figure 72: Experimental Trial to determine temperature dependence of coating comprised of oleate-capped nanoparticles on glass. This figure depicts average emission intensity from both green and red emission bands for each temperature interval.

Figure 72 depicts the average emission intensity of both the green and red emission from the sample with varying temperature. For the green emission, the average intensity increased over the entire range of temperatures, from 3076.0 counts at 20.6°C to 6666.5 counts at 50.2°C. The largest standard deviation was calculated to be 97.35 counts at 29.9°C, with a standard error of 39.74 counts. For the red emission, the average intensity decreased over the same temperature range, from 7474.2 counts at 20.6°C to 6430.2 counts at 50.2°C. The largest standard deviation was calculated to be 14.04 counts at 25.1°C, with a standard error of 5.73 counts.

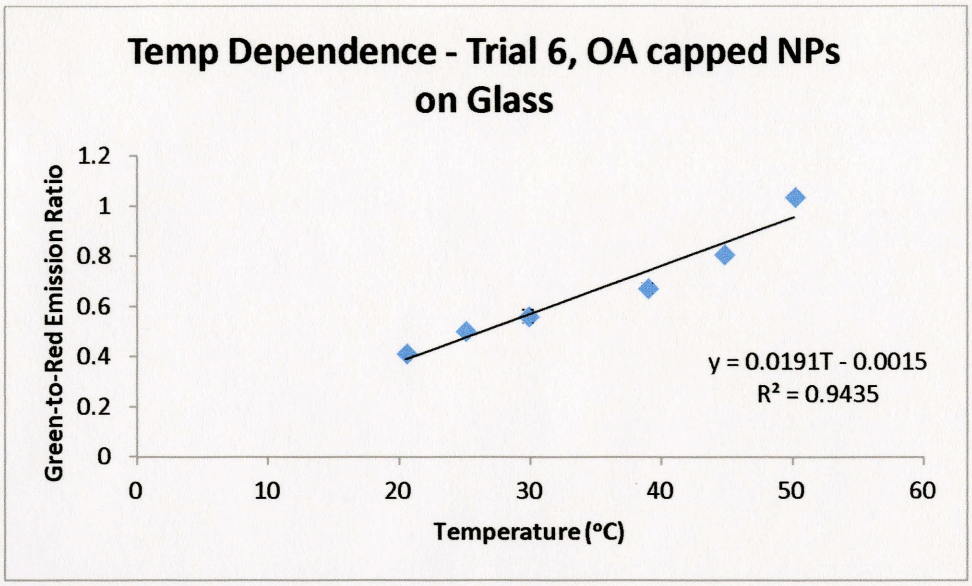

Figure 73. Experimental Trial to determine temperature dependence of coating comprised of oleate-capped nanoparticles on glass. This figure depicts the ratiometric temperature dependence of the green-to-red emission ratio from the nanoparticles on the glass surface.

When the Green-to-Red Emission ratio was constructed, there was a clear linear dependence shown. The ratio increases from 0.41 at 20.6°C to 1.04 at 50.2°C, for an overall ratio change of 0.63. The largest standard deviation was calculated to be 0.025 at 29.9°C, with a standard error of 0.0103. A linear trend line fit to this data resulted in an R^2 value of 0.9435, indicative of a linear relationship.

3.13 - Temperature Sensitivity Experiment 7 – Nanoparticle Coating on 25 mL Flask

The 7th temperature sensitivity experiment was performed using the coating of oleate-free nanoparticles that was created on a 25 mL flask. The coating was created by pipetting 200 µL of sample OAR10-12 onto the label on the flask, and then allowing it to dry overnight in the fume hood.

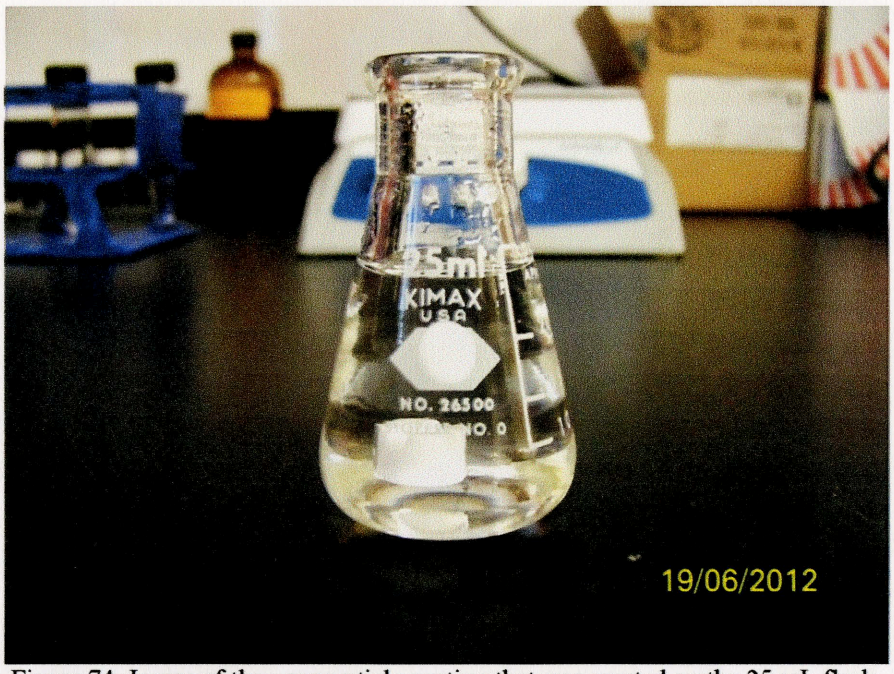

Figure 74: Image of the nanoparticle coating that was created on the 25 mL flask.

Figure 74 shows a picture of the coating that was created on the flask. The coating was circular in shape, with a diameter of about 6 mm.

The temperature sensitivity experiment utilizing the flask coating was performed in the same manner as the previous experiments using the coated glass slides. The laser beam from the 980 nm diode laser was again directed to the flask coating using a fiber optic cable with attached lens, but the position of the lens had changed. The camera was triggered by the laser pulse, using a pulse width of 100 μs and 1350 mA intensity, so that the 980 nm excitation light would be at a minimum in the collected images. The temperature of the slide was varied from 21.1°C to 48°C, with the aim of taking images at 5°C temperature intervals. For this trial, the 6 lowest emission intensities from the image sets were used from each of the green and red filter cubes for each temperature interval, using an exposure time of 3 seconds. Background subtraction was performed on all of the

images to improve accuracy. An area of 4484 pixels was used to measure the average emission intensity from the coating at each temperature interval. The pixel area was adjusted to accommodate for the laser spot size since the fiber optic lens position had changed. Since the emission from the coating did not encompass the entire field of view, the pixel area used was positioned over a specific area of interest where the emission was present.

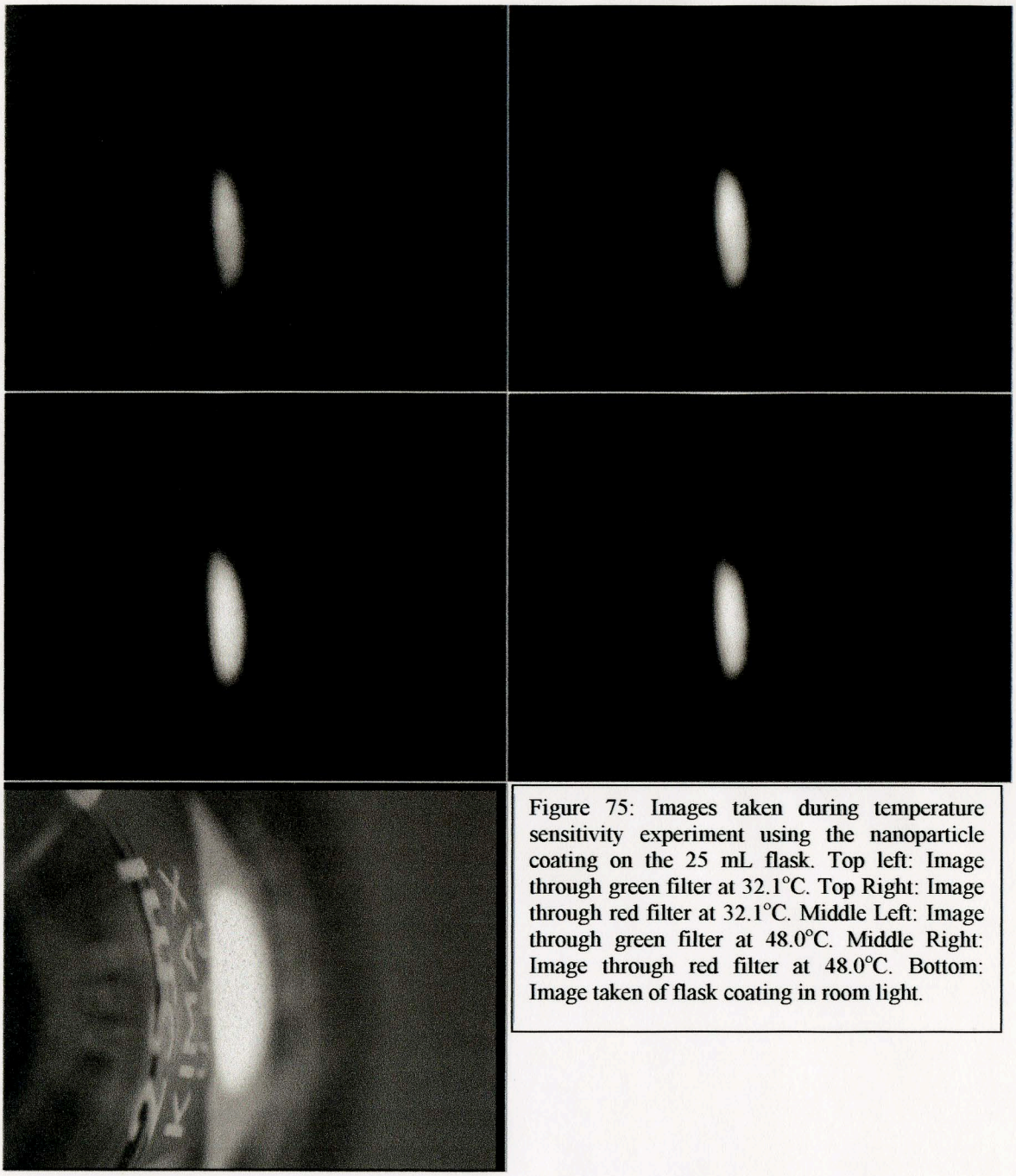

Figure 75: Images taken during temperature sensitivity experiment using the nanoparticle coating on the 25 mL flask. Top left: Image through green filter at 32.1°C. Top Right: Image through red filter at 32.1°C. Middle Left: Image through green filter at 48.0°C. Middle Right: Image through red filter at 48.0°C. Bottom: Image taken of flask coating in room light.

Figure 75 depicts some of the images that were obtained during the 7th temperature sensitivity trial. An image of the nanoparticle coating on the flask under the microscope

in room light conditions was taken, using no filter and a 1 second exposure time. The coating on the flask surface appears to be somewhat visually uniform.

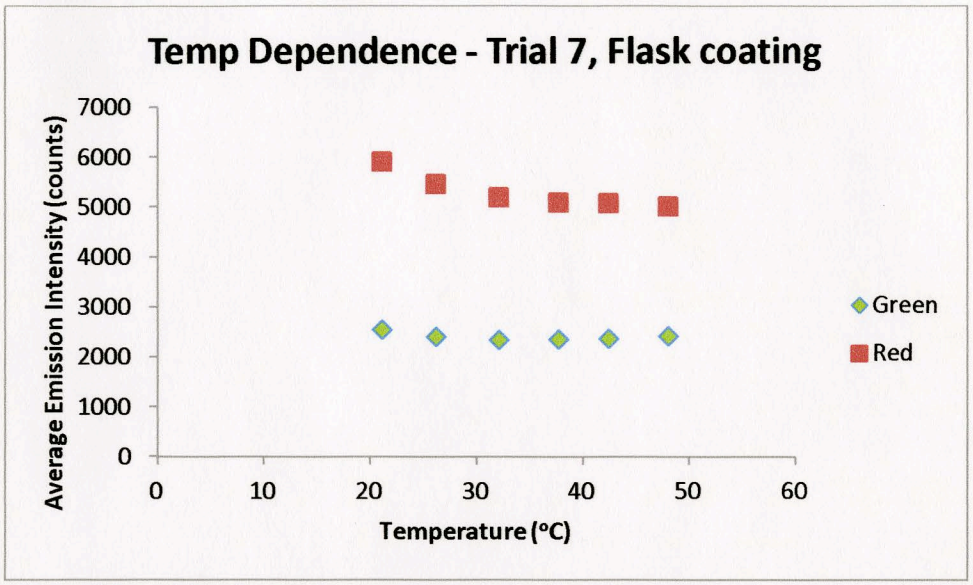

Figure 76: Experimental Trial to determine temperature dependence of coating comprised of oleate-free nanoparticles on the surface of 25mL flask. This figure depicts average emission intensity from both green and red emission bands for each temperature interval.

Figure 76 depicts the average emission intensity of both the green and red emission from the sample with varying temperature. For the green emission, the average intensity slightly decreased over the entire range of temperatures, from 2550.0 counts at 21.1°C to 2427.5 counts at 48.0°C. The largest standard deviation was calculated to be 15.76 counts at 21.1°C, with a standard error of 6.44 counts. For the red emission, the average intensity decreased over the same temperature range, from 5726.3 counts at 21.1°C to 4831.7 counts at 48.0°C. The largest standard deviation was calculated to be 26.2 counts at 42.4°C, with a standard error of 10.7 counts.

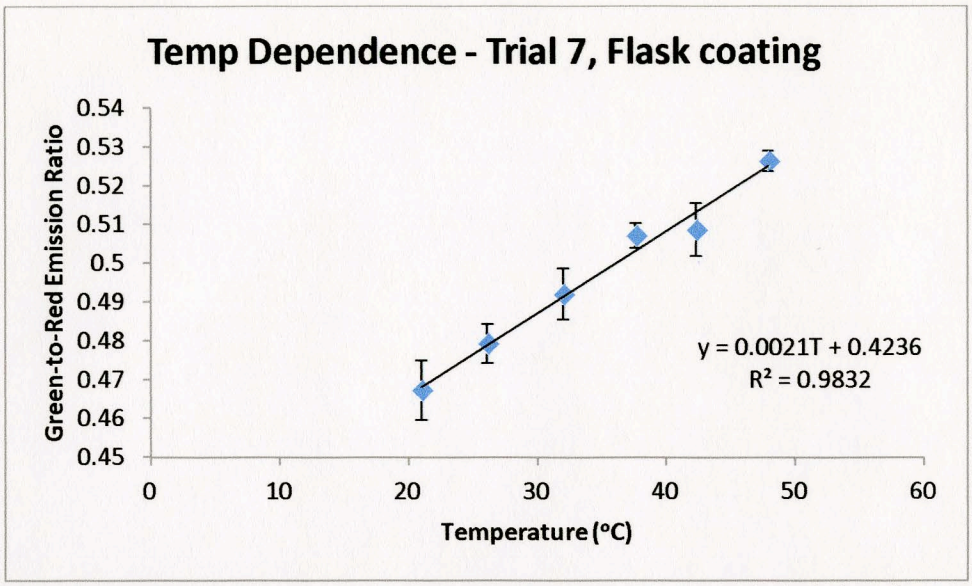

Figure 77: Experimental Trial to determine temperature dependence of coating comprised of oleate-free nanoparticles on the surface of 25mL flask. This figure depicts the ratiometric temperature dependence of the green-to-red emission ratio from the nanoparticles on the flask surface.

When the Green-to-Red Emission ratio was constructed, there was a clear linear dependence shown. The ratio increases from 0.47 at 21.1°C to 0.53 at 48.0°C, for an overall ratio change of 0.06. The largest standard deviation was calculated to be 0.0076 at 21.1°C, with a standard error of 0.0031. A linear trend line fit to this data resulted in an R^2 value of 0.9832, indicative of a linear relationship.

3.14 - Temperature Sensitivity Experimentation – Summary

Trial	Oleate	Temp Range (°C)	ΔT	GRR Range	ΔGRR	ΔGRR /ΔT	Exposure Time	Pixel area	R^2 value
521/668	Yes	11-48.1	37.1	0.334-0.562	0.228	0.0061	45s	n/a	0.9912
541/668	Yes	11-48.1	37.1	1.676-1.848	0.172	0.0046	45s	n/a	0.6740
1 - GE10	No	20-45	25	2.688-5.290	2.602	0.1041	60s	10625	0.0023
2 - GE10	No	20.8-60	39.2	1.534-4.101	2.567	0.0655	20s	10625	0.9650
3 - GE10	No	20.6-50	29.4	1.334-2.315	0.981	0.0334	30s	16906	0.9685
4 - GE14	No	20.5-50	29.5	0.81-7.17	6.36	0.2156	10s	10625	0.9880
5 - GE14	No	21-45.2	24.2	0.58-4.46	3.88	0.1603	10s	6900	0.9895
6 - OA-cap NP	Yes	20.6-50.2	29.6	0.41-1.04	0.63	0.0213	10s	10625	0.9435
7 - Flask Coating	No	21.1-48	26.9	0.47-0.53	0.06	0.0021	3s	4484	0.9832

Table 6: Green-to-Red Emission Ratio results from all temperature sensitivity trials

Table 6 outlines the key data from all of the above mentioned temperature sensitivity experiments. While the range of temperatures did vary slightly, most of the temperature experiments cover the temperature range from 20-50°C.

For the constructed emission ratios using the oleate-capped $NaYF_4:Er^{3+},Yb^{3+}$ nanoparticles in chloroform, the ΔGRR are 0.228 and 0.172 for the 521/668 and 541/668 ratios respectively. Trial 6 where the experiment involved oleate-capped nanoparticles on

a plain glass slide, the ΔGRR is 0.63. So for all 3 trials utilizing oleate-capped nanoparticles, the largest ΔGRR was 0.228.

For Trial 1 which involved sample GE10, oleate-free nanoparticles on carboxylated glass, the ΔGRR was 2.602, but since the R^2 value indicates no linear dependence of the plotted data points, this trial data can be omitted. For Trials 2 & 3 which utilized the same sample GE10, the ΔGRR was 2.567 and 0.981 respectively. For Trials 4 & 5 which utilized sample GE14, oleate-free nanoparticles on carboxylated sand-blasted slides, the ΔGRR was 6.36 and 3.88 respectively. The outlier for the temperature experiments utilizing oleate-free particles was the flask coating experiment, which had a ΔGRR of only 0.06. If the data from the flask coating experiment is set aside, the largest ΔGRR observed when using oleate-free nanoparticles was 0.981, approximately 5 times larger than the ΔGRR observed with oleate-capped nanoparticles. It is also important to note that besides data for the temperature sensitivity trial 1 and the 541/668 emission ratio, that the 521/668 emission ratio and the other temperature sensitivity trials all exhibited good linear relationships between the Green-to-Red emission ratio and temperature, with the R^2 values ranging between 0.9435 and 0.9912. The R^2 value for the 541/668 emission ratio was only 0.6740, much lower than for the rest of the trials, but still indicative of a somewhat linear relationship.

3.15 – Stability of Nanoparticle Coatings on Glass Surfaces

For the two nanoparticle-coated glass surfaces that were used in the temperature sensitivity experiments (GE10 & GE14), it was important to investigate the stability of

the nanoparticle coating. As mentioned previously in section 3.4, many of the early attempts to form a coating of oleate-free nanoparticles onto glass surfaces were very unstable, and the coating could be easily washed off with water delivered via pipette onto the glass. After temperature experimentation with both samples GE10 and GE14 had concluded, both glass samples were washed twice with nanopure water delivered via pipette, and were allowed to dry in the fume hood.

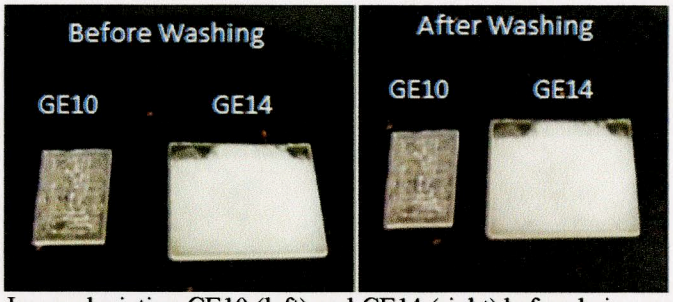

Figure 78: Left panel: Image depicting GE10 (left) and GE14 (right) before being washed with H_2O. Right panel: Image depicting the same samples after being washed with H_2O delivered via pipette 2 times and dried in the fume hood.

Figure 78 above shows images of both glass samples before and after the 2 washes with nanopure water.

While this visual confirmation of the coating stability was a good sign, the upconversion luminescence signal produced by the glass is of much higher importance than the visual appearance of the glass, and the effect of the washing on the signal was investigated.

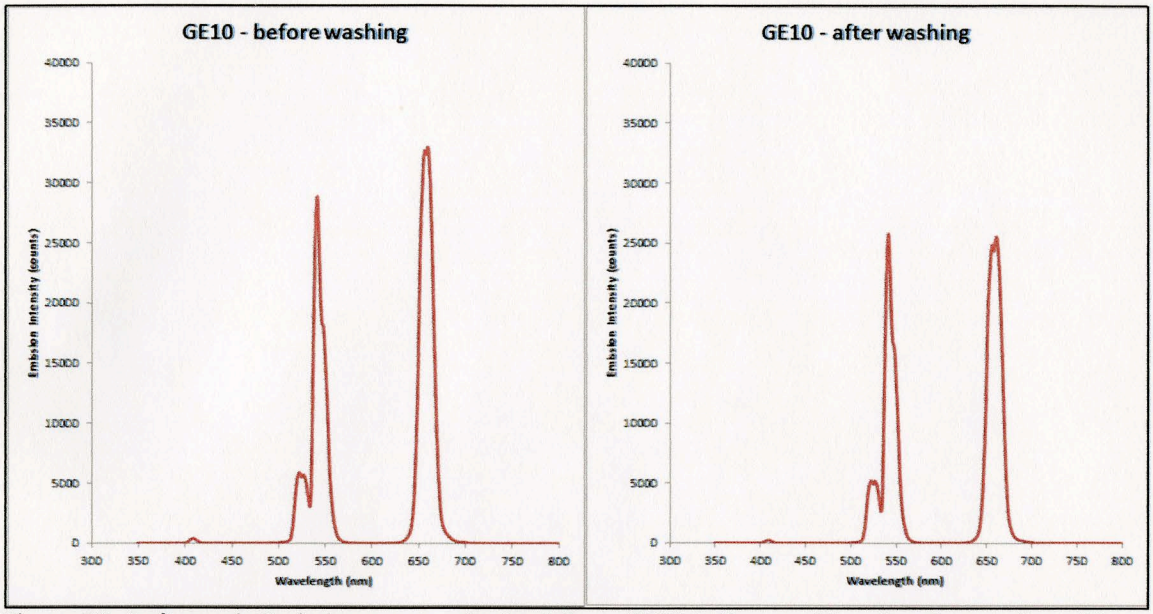

Figure 79: Left panel: Emission spectra obtained from GE10 before washing the glass surface, 10 sec. integration time. Right panel: Emission spectra obtained from GE10 after washing the glass surface, 10 second integration time.

Figure 79 above shows emission spectral data that was obtained for sample GE10 before and after washing the glass surface. To obtain each spectra, a pulse width of 100 μs, 10.00% duty cycle, 1350 mA intensity, and a 10 second integration time was used.

Emission Peak	Emission Intensity - before wash	Emission Intensity - after wash	% Intensity Decrease
523 nm	5893	5243	11.03
541 nm	28888	25796	10.70
660 nm	32976	25171	23.67

Table 7: Emission peak intensity values for GE10 before and after washing the glass surface

Both spectral data sets show well defined emission peaks in the 523nm, 541nm, and 660nm emission regions. Before washing, the intensity for the 523nm emission was 5893 counts, the intensity for the 541nm emission was 28888 counts, and the intensity for the 660nm emission was 32976 counts. After washing, the intensity for the 523nm emission

was 5243 counts, the intensity for the 541nm emission was 25796 counts, and the intensity for the 660nm emission was 25171 counts. After washing, there was an 11.03% intensity decrease for the 523nm emission peak, a 10.70% intensity decrease for the 541nm emission peak, and a 23.67% intensity decrease for the 660nm emission peak.

3.16 – Temperature Sensitivity Experiment 8 – 2D Temperature Distribution Map

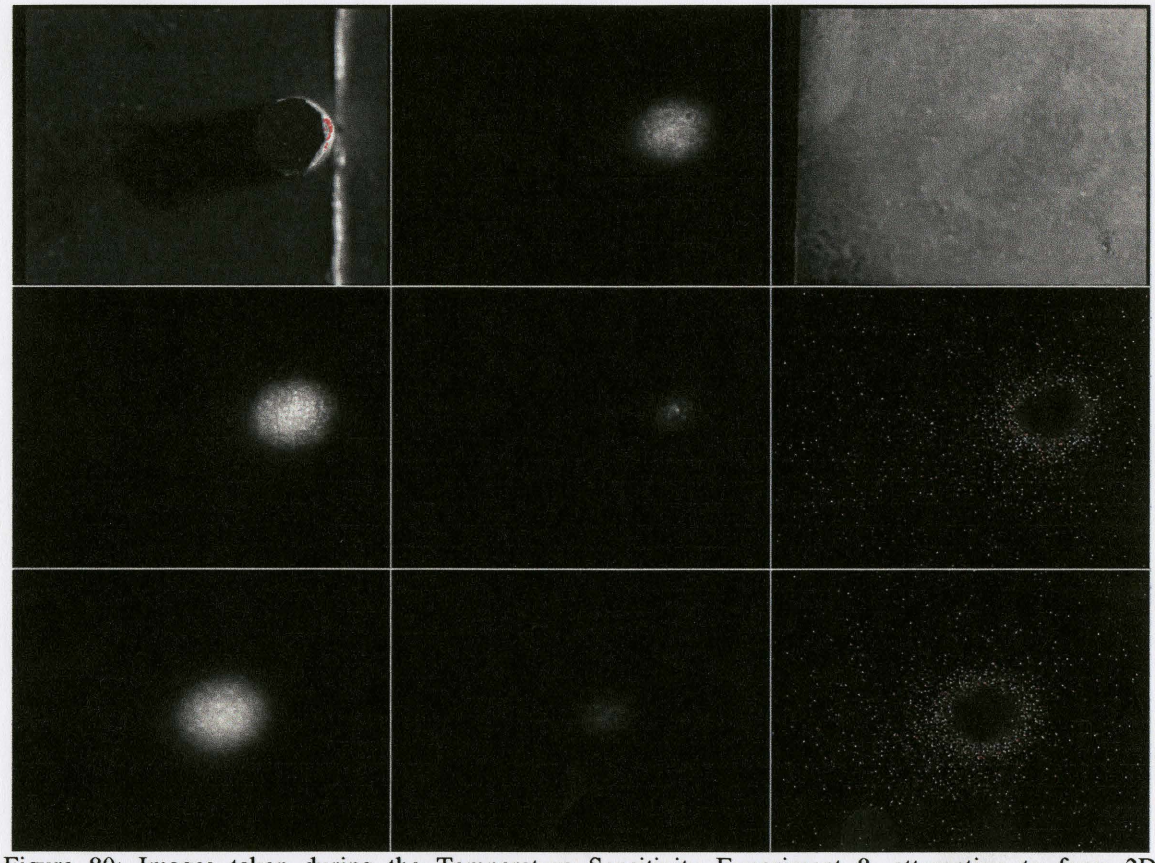

Figure 80: Images taken during the Temperature Sensitivity Experiment 8, attempting to form 2D Temperature Distribution map. Top left: Position of cylinder Top middle: 980 nm diode laser spot location. Top right: Picture of GE14 slide on top of cylinder, imaged in room light. Middle left: Green emission from GE14 slide atop cylinder at 37°C. Middle panel: Red emission from GE14 slide atop cylinder at 37°C. Middle right: Constructed Green-to-Red ratio map for GE14 on cylinder, by dividing green emission image and red emission image. Bottom left: Green emission from GE14 slide on hot plate at 37°C. Bottom middle: Red emission from GE14 slide on hot plate at 37°C. Bottom right: Constructed Green-to-Red ratio map for GE14 on hot plate, by dividing green emission image and red emission image.

Figure 80 depicts the images and constructed Green-to-Red emission maps produced during the 2D temperature distribution experiment. The top left image shows the position of the aluminum cylinder, while the top middle image shows the position of the laser spot. The laser spot size and the aluminum cylinder are well aligned. The top right image shows the GE14 sample resting on top of the aluminum cylinder.

The middle set of images were used to create the Green-to-Red emission map when the sample was on the aluminum cylinder. The left image shows the green emission from the sample while the middle image shows the red emission from the sample. When these images were divided using the ImageX 2012 software, the resulting Green-to-Red emission map on the right was created.

The bottom set of images were used to create the Green-to-Red emission map when the sample was resting on the hot plate itself. The left image shows the green emission from the sample while the middle image shows the red emission from the sample. When these images were divided using the ImageX 2012 software, the resulting Green-to-Red emission map on the bottom right panel of figure 80 was created.

Section 4

Discussion

4.1 – Synthesis & Characterization of Lanthanide-doped Nanoparticles

The initial synthesis of α-phase $NaYF_4$ nanoparticles proved to be much more difficult than had been initially reported by the Capobianco group[19]. The majority of the synthetic procedure was kept constant besides a few variances. One major difference was the use of a lyophilization step between the formation of the lanthanide trifluoroacetate precursors and the secondary synthetic reaction where those precursors were then used to form the nanoparticles. The Capobianco group instead used a "one-pot" synthesis, in which the solution from the first synthetic reaction was heated under vacuum to remove any excess water and oxygen. Efforts to replicate this vacuum induced heating did not dry the nanoparticle precursors adequately, whereas the use of a lyophilization process yielded dry powders that could be easily used for the secondary reaction.

As can be noted from Table 1, there was a large number of nanoparticle samples that were synthesized in order to demonstrate reproducibility of this synthesis. While at first, the nanoparticle samples that were synthesized had the desired size characteristics (<30 nm diameter) and formed clear solutions when dispersed in chloroform, repeated synthetic attempts showed that there was considerable size and dispersion variability from repeated synthetic trials with the same protocol. After careful review of the synthetic procedure, certain control parameters were introduced to limit this variability.

One concern centered around the oleic acid that was being used for the nanoparticle syntheses, and that possible oxidation of the oleic acid was contributing to the coloration of the dispersed nanoparticle samples. To combat this, the ultraviolet light was kept off for the entirety of the secondary synthetic reaction, when oleic acid was in use, and the two additional argon purges that were performed before the reaction started were added to try and remove any residual water and oxygen before thermocycling began. A new batch of oleic acid was also ordered for fear of possible contamination of the source, and was stored in the refrigerator under argon atmosphere when not in use.

Another concern regarded the vacuum grease that was used in the experimental setup to seal together glassware components. Despite its heat rating, when cleaning the glassware after certain syntheses, it could be seen that the vacuum grease had become extremely viscous, and could have gotten mixed into the solution media that the nanoparticles were forming in at critical high temperatures (300°C). It was also interesting to note that in syntheses where vacuum grease was used in conjunction with the glass adapters that were used for the thermometer, argon and vacuum lines, that if nanoparticles were formed during the synthesis, that the resulting particle mass was lower than syntheses where rubber adapters and no vacuum grease was used. For this reason, for the later syntheses no vacuum grease was used in the experimental setup, specifically at the interface between the reflux column and the round bottom flask.

A final concern with the original synthetic protocol dealt with the rubber adapters that were used for the thermometer and vacuum and argon lines. The original rubber adapters

that were used were orange in color, and it became apparent that after multiple uses, these adapters were degrading and that coloration was clearly apparent in the resulting nanoparticle dispersions. White rubber adapters were then used in the setup, and were replaced at the first sign of any sort of discoloration. While some samples synthesized using the white adapters in the setup did exhibit some light yellow/orange coloration, this was dramatically decreased by the change in adapter type.

With all of these controls in place, the effect on the quality of synthesized nanoparticles was clearly apparent. As shown in Figure 26, about 85% of the nanoparticle samples synthesized after synthetic controls were implemented had particle diameters below the desired 30 nm threshold. Figure 27 shows that cumulatively, most of the samples that were prepared all fell within a specific range of having particle diameters below 40 nm with the peak widths below 11.0 nm, although most of those samples in that distribution were synthesized after experimental controls were implemented.

The images displayed in section 3.1 clearly show the difference in quality between dispersed nanoparticle samples created before and after experimental controls were implemented. Samples produced before the controls were implemented have significant coloration and light scattering, and as would be expected, the samples with darker coloration and increased scattering correspond to nanoparticle samples with larger particle diameters. After controls were implemented, while there still is light yellow coloration of dispersed samples, the light scattering is significantly decreased. A side by side comparison of these two sets of samples in Figure 30 illustrates this clear difference

in synthetic quality. That is not to say that samples of high synthetic quality and desirable size characteristics were not produced at all before the experimental controls were implemented, as shown in Figure 31; simply that those samples were synthesized with relative ease once controls were introduced.

The two samples that were sent for XRD characterization both exhibit well defined peaks at locations that are consistent with the calculated line-pattern for α-phase $NaYF_4$ (Figures 21-22). For comparison, the calculated line pattern from JCPDS card No. 77-2042 was used. The peaks shown at two-theta values of 28.24, 32.72, 46.94, 55.69, 58.40, 68.57, 75.73, 78.07, 87.24 degrees (Figure 23) are all shown in the line patterns for both $NaYF_4:Er^{3+},Yb^{3+}$ and $NaYF_4:Tm^{3+},Yb^{3+}$ nanoparticles that were analyzed.

Upconversion luminescence exhibited by the nanoparticles varied considerably from sample to sample. Figures 24-25 show both $NaYF_4:Er^{3+},Yb^{3+}$ and $NaYF_4:Tm^{3+},Yb^{3+}$ samples that exhibit very bright upconversion luminescence through clear dispersions of the nanoparticles in chloroform, and represent the highest quality samples that were able to be produced during the course of this research. As for the emission spectral data that corresponds to the erbium-doped nanoparticles that were synthesized, although the emission peaks in the green and red spectral regions were not exactly where they were expected, all of those peaks are represented in their relative positions in the spectral data for the 3 nanoparticle samples shown (Figures 17-19). The emission intensity varies greatly between the samples, despite some differences in the integration times used to collect the spectral data. For samples 68C (Figure 17) and 77A (Figure 18), both spectral

data sets were collected using integration times of 60 seconds, however sample 77A had peak emission intensities roughly 3 times larger than sample 68C. The spectra for sample 85A (Figure 19) was collected using only a 1 second integration time, but the peak emission intensities are on par with the intensities seen in the spectra for sample 77A, where a 60 second integration time is used. That would indicate that there is still some variability of the efficiency of the upconversion process from sample to sample, that could relate back to intricacies in the synthetic method. The spectral data for one of the thulium-doped nanoparticle samples (Figure 20) shows all emission peaks in their relative positions with the exception of the peak at 800 nm, which is usually of great interest. This is unfortunately due to the 700nm shortpass excitation filter that was used to block out the 980nm excitation light in the spectra. Even with the filter, the spectral data indicates that significant excitation light was being transmitted through the filter. Given the decreased range of sample diameters, absence of coloration and light scattering, and upconversion luminescence exhibited from samples created after the experimental controls were implemented, it is safe to conclude that the first objective of this research of demonstrating a reproducible and controlled synthesis of α-phase $NaYF_4:Er^{3+},Yb^{3+}$ and α-phase $NaYF_4:Tm^{3+},Yb^{3+}$ nanoparticles was met.

4.2 – Oleic Acid Removal Experiments

The main rationale behind the oleic acid removal experimentation was to create charged nanoparticles that would enable binding through electrostatic interactions in the subsequent carboxylated glass experimentation and electrophoretic deposition

experiments. Since the oleate ligand that initially coats the nanoparticles after synthesis is initially bound through coordination between the carboxyl group on the oleic acid and the lanthanide ions on the surface of the nanoparticle, it stands to reason that if the oleate ligand is dissociated from the nanoparticle surface as oleic acid, that the nanoparticle surfaces would be charged, and could bind to carboxyl functionalization created on glass surfaces. However, in contrast with the original synthesis of oleate-capped $NaYF_4:Er^{3+},Yb^{3+}$ nanoparticles, the creation of oleate-free nanoparticles from the originally synthesized samples had many issues with sample consistency and reproducibility.

The procedure to remove the oleate ligand from the nanoparticle surfaces was originally proposed by the Capobianco research group, and utilizes a simple acid treatment of the nanoparticles to protonate and release the oleate ligand from the surface.[31] To the best of our knowledge this research represents one of the first attempts to reproduce the results published by the Capobianco group. As details of the synthetic procedure were not disclosed in full, modifications to the published synthetic method were made in order to try and reproduce the results. For the first few oleate removal experiments (OAR1-OAR5) the procedure was still being optimized in terms of pH changes, extraction solvent, reaction times, etc. but after that the procedure was kept constant. Oleate-capped nanoparticles were dried via lyophilization and were dispersed in 20 mL of nanopure water in 100 mg amounts per synthesis. The pH of the solution was then adjusted to 3.5 using a 0.1M HCl solution, and the reaction was stirred for a period exceeding 12 hours,

and then underwent liquid-liquid extraction with hexane three times to remove the oleic acid in solution. The hexane extractions were each performed for a period over 12 hours, to allow the maximum amount of time for the oleic acid to move into the hexane layer.

Table 2 lists all the nanoparticle samples that underwent the oleate removal process during the course of this research. It can be easily seen that there is an unexpected increase in particle size between the original oleate-capped nanoparticles and their oleate-free counterparts. The particle diameters of the original oleate-capped nanoparticles range between 12.66-54.61nm, while the particle diameters of the nanoparticles that have undergone the oleate removal process range between 86.44-545.3nm. Even for sample OAR4 which had the closest particle diameter (147.9nm) to that of the original oleate-capped nanoparticle (54.61nm), there is still a 170% increase in particle diameter between the original nanoparticle sample and the resulting sample. Sample OAR7, which had the smallest particle diameter (86.44 d.nm), still represents a 583% particle diameter increase over the original oleate-capped sample (12.66 nm).

As shown in Figure 33, there are large particle diameter variations between the samples that underwent the oleate removal process. While the figure does seem to show a trend of increasing particle diameter as the oleate removal process was refined, the accuracy of the particle sizing results have to be scrutinized. One major justification for this is that when multiple particle sizing measurements were taken of the same sample either consecutively or at a later date, there were sometimes significant variation between sizing measurements of the same sample. That is because for the most part, the nanoparticles

that underwent the oleate removal procedure did not form colloidal solutions when dispersed, and very often had to be sonicated and vigorously shaken in order for particle sizing measurements to be made. Evidence of this can be clearly seen in Figures 36-39. In Figure 36, an image of sample OAR7 immediately after sonication is shown, and then an image of the same sample 10 minutes later. The time lapsed image distinictly shows particle aggregation at the bottom of the vial, indicating that a large majority of those particles have fallen out of solution. Some of the samples seemed to be disperse given enough sonication time (Figures 37-38), however, given enough time at rest without agitation, the particles would settle at the bottom of the vial again (Figure 39). This is not extremely surprising given the large particle sizes that approach half a micron. For many solutions, in the time it took to remove the sample from the sonicator and prepare it for a particle sizing measurement, many of the larger particles or aggregates would have already fallen out of solution, skewing the resulting measurement. This theory was supported by testing many of the supernatants of the oleate-free samples with the NIR diode laser. Under 980nm excitation, the supernatants exhibited little to no upconversion luminescence in spectral data; however when the particle aggregates on the bottom of the glass vials were held up to the laser, there was visible upconversion luminescence that could be observed.

A good example of this is shown in Figure 40, where a relationship between particle size and sample pH was being investigated for sample OAR6. For the first trial, the pH was varied between 2.5 and 8.0. The particle size ranges between 31.22-150.2 nm diameters,

with the particle size appearing to increase at basic pH values. However, a previous sizing measurement put the particle diameter of OAR6 at pH 4.0 at 163.8nm, whereas the trial data shows particle diameters in that pH range under 100nm. During the second trial, the pH was varied between 3.35-6.65 with 2 sizing measurements taken at each pH interval. In this trial, it appears that the particle diameter is decreasing with increasing pH, but there were also large inconsistencies between many of the two sizing measurements performed at each pH interval. Given the fact that these two experimental trials of the same sample yielded completely opposite trends, it is safe to assume that the particle sizing data for the nanoparticle samples that underwent the oleate-removal process is skewed, as the samples could not form stable colloidal solutions even during the course of a particle sizing measurement.

For that same sample OAR6, the relationship between zeta potential and solution pH was also investigated, shown in Figure 41. The Capobianco group reports being able to "tune" the surface charge of the nanoparticles after the oleate ligand has been removed using varying pH. Their justification is that in acidic conditions, the oleate ligand is protonated and leaves a positively charged surface, that could be either a surface ion pair $Ln(III)^{+}Cl^{-}$ or a coordinated $[Ln^{III}OH_2^{+}]\cdots Cl^{-}$, while in basic conditions the surface is deprotonated resulting in a negatively charged surface, and $[LnO^{-}]\cdots H_3O^{+}$ coordination.[31] Their zeta potential results appear to support their claims, showing +23 mV zeta potential at pH 4.0, and -45 mV zeta potential at pH 7.4. For sample OAR6, two trials were done to investigate this potential relationship. In Trial 1, the zeta potential varies between

+49.4mV and +28.2 mV in the pH range from 2.5-8.0, and for Trial 2, the zeta potential varies between +37.2 mV and +29.2 mV in the pH range from 3.65-6.65. The results of both trials depict this trend of decreasing zeta potential with increasing pH, but the surface charge cannot be tuned into the negative range. From this data, it seems to suggest that for sample OAR6, the nanoparticle surface can be partially deprotonated to result in lowering the positive surface charge, but cannot be fully deprotonated to result in a negatively charged surface.

The relationship between zeta potential and pH was also investigated for sample OAR10-12, which was used in subsequent nanoparticle coating experiments. (Figure 42) Sample OAR10-12 was actually a combination of samples OAR10, OAR11, and OAR12, which were all synthesized concurrently, using the same original oleate-capped nanoparticle sample, and the same procedure. The idea was to simply combine the samples and disperse it in 20 mL of nanopure water, so that there would be one sample that had a higher concentration of 15 g nanoparticle/L (0.3 g/20 mL), compared to the standard 5 g nanoparticle/L (0.1 g/20 mL). For sample OAR10-12, the zeta potential varied between +31.1 mV and -10.1 mV in the pH range from 3.95-7.75. This trend was also very linear with an R^2 value of 0.9576. The data from this trial depicts the same trend as the previous results, of decreasing zeta potential with increasing solution pH. However, these results show that the zeta potential, and thus the surface charge of the nanoparticle can be driven into the negative range at very basic pH levels. From this data, it seems to suggest that for sample OAR10-12, the nanoparticle surface can be fully deprotonated to result in a

negative surface charge, but this only occurs at basic pH values around 7.0 and up. In fact, this data exhibits an isoelectric point at pH 6.78, where the Capobianco results show an isoelectric point at 5.8.[31]

FTIR characterization of one of the nanoparticle samples that underwent the oleate removal process (Figure 35) supports the claim that the oleic acid was removed from the nanoparticle surfaces during this procedure. The sample was analyzed via FTIR before the oleate removal process was started, and at each hexane extraction stage, after the process was completed. The FTIR data for the original oleate-capped nanoparticles exhibit two well defined peaks at 2853 cm^{-1} and 2924 cm^{-1}, which represent CH_2 bond stretching and are indicative of the oleic acid on the nanoparticle surfaces. However, it can be seen that these peaks are absent even after the first hexane extraction. If the FTIR data is magnified to the position of the peaks for the data corresponding to all 3 hexane extractions, at very high magnifications the peaks can be seen, indicating there is some minute amount of oleate ligand still on the nanoparticle surfaces. However, by comparing the FTIR peak intensity values before the oleate removal process had started and after the 3rd hexane extraction, we can state that over 99% of the oleate ligand is removed from the nanoparticle surfaces. While this characterization was only performed for one sample, it does lend support to the notion that the oleate removal process does remove a majority of the ligand from the nanoparticle surfaces.

As the Capobianco group reported an unchanged particle size after the oleate removal process, no agglomeration, and the ability to tune the zeta potential of the particles in a

wide range using pH changes, the findings of this research study are in direct contrast to their results. Regardless of the inconsistencies in the particle sizing measurements, there is no question that the particle diameters of the nanoparticle samples that have underwent the oleate-removal procedure are much larger than the particle diameters of the original oleate-capped nanoparticle samples. Given that the oleate removal process only removes the oleate ligand from the nanoparticle surfaces, and does not affect the crystal structure of the nanoparticles, it can be assumed that this drastic increase in particle diameter can be attributed to agglomeration. After careful consideration of what could be causing this agglomeration, the process of drying the nanoparticles prior to the oleate removal process was called into question. Synthesized nanoparticle samples that were to be used in the oleate removal experiments had to first be precipitated out of solution using acetone, and then were isolated via centrifugation. After being washed with ethanol 2 times and isolated again via centrifugation, the supernatant was pipetted off. The sample was then frozen in a dry ice/acetone bath and placed in a freeze dryer to attempt to remove any remaining moisture, very similar to the lyophilization process after the 1st synthetic reaction to make the lanthanide trifluoroacetate precursors (section 2.1). However, once the nanoparticle sample was dried, the precipitate was broken up manually before dispersion in H_2O for the oleate removal procedure, either by using a spatula or mechanical agitation. In some cases, the precipitate was sonicated shortly after being dispersed in nanopure H_2O, but large aggregates of nanoparticles were still present (Figure 32). As such, if the oleate removal process was performed on aggregated oleate-

capped nanoparticles, it may be possible that only the oleate ligands on the outside surfaces of the nanoparticle aggregates were removed. Upon being redispersed in H_2O after the procedure, the surface regions of the nanoparticles where the non-polar oleate ligands remained would be hydrophobic, so those nanoparticle aggregates would stay together, and could cause increased aggregation with other nanoparticles that had only partial removal of the oleate ligands. This would account for the dramatic increase in particle size, as well as provide a possible explanation for the newly dispersed "oleate-free" samples not forming colloidal dispersions in H_2O. While the FTIR characterization shown in Figure 35 seems to contradict this theory, the characterization was only performed on one sample, and may not accurately represent all the "oleate-free" nanoparticle samples that were made.

Another possible explanation for particle aggregation with respect to pH changes relates to this concept of having partial removal of the oleate ligands on some of the nanoparticles and full removal of the oleate ligands on others. As the zeta potential data for OAR6 and OAR10-12 has demonstrated, some of the "oleate-free" samples were able to be driven into the negative range at basic pH while others were only able to be partially deprotonated to result in decreased, but still positive zeta potential. It stands to reason that if at the same pH range there are nanoparticles within the same solution that have both positive and negative surface charge, that they may aggregate due to electrostatic interactions.

Despite the issues with particle aggregation and the absence of stable colloidal nanoparticle solutions, the nanoparticles in these samples still exhibited upconversion luminescence under 980nm excitation from the NIR diode laser, and were therefore used in the subsequent electrophoretic deposition experiments and carboxylated glass deposition experiments.

4.3 – Electrophoretic Deposition Experiments

For all types of electrophoretic deposition (EPD) processes, particles that are suspended within a dispersant move under the influence of an applied electric field and are deposited on the oppositely charged electrode. The procedure for the EPD experimentation was adapted from a previous report in the literature where phosphor particles were deposited onto indium tin oxide (ITO) glass under an applied electric field[41]. Given that the oleate-free nanoparticle solutions had positive zeta potentials, it was hypothesized that under an applied electric field, the particles would move towards the ITO slide that was acting as the negative cathode. Review of the original article saw that the optimal deposition conditions occurred when the power supply was run at 200 V for 120 seconds, with approximately 1 inch of spacing between the two ITO glass slides.[41] These conditions were therefore used as a starting point during the EPD experimentation.

For the first trial, sample OAR8 was dispersed in 80 mL H_2O for a solution concentration of 1.25 g/L (0.1 g nanoparticles / 80 mL). The pH was adjusted to 4.0 using 0.1M HCl, with a recorded zeta potential value of +30.5 mV at the time. However, a current could not be induced through the solution for this trial. Review of the original EPD article

showed that the phosphor particles were dispersed in an isopropyl alcohol solution, so for subsequent experiments the oleate-free nanoparticle samples were dispersed in IPA at the same concentration as the first trial. Even though pH could not be monitored in an IPA solution, small volumes of 0.1M HCl were added to the solutions to attempt to increase the zeta potential of the particles, and increase binding affinity to the ITO glass. For the 3 experiments (EPD Trial 2, 3, and 4) that were run in IPA solutions, the zeta potentials were recorded at +29.4 mV, + 29.4 mv, and +24.8 mV respectively (Table 3). A current was able to be induced through the solutions for EPD trials 2 and 3, but unfortunately not for trial 4. One possible reason for this is that since the same nanoparticle solution in IPA was used for EPD trials 2-4, perhaps a high concentration of the charged nanoparticles were deposited onto the ITO glass during the 2^{nd} and 3^{rd} trials, and there were not enough present to allow for an induced current during the 4^{th} trial.

For EPD trials 2 and 3, the power supply was run at 200 V for 120 seconds and 157 seconds respectively, and there is a visible deposition of material onto the ITO glass, as seen in Figure 43. It can be easily observed that the deposition on the glass was irregular and non-uniform. Given that the power supply was run at 200 V and the ITO slides were separated by a 1 inch (2.54 cm) spacer, the electric field strength produced during these experiments was 7874 V/m. However, because the ITO glass slides are finite surfaces, the electric field lines at the edges of the glass would not run perpendicular to both surfaces, and it would be expected that there would be more deposition in the middle of the ITO glass and less deposition at the edges. Surprisingly, that is exactly the opposite

effect that is visually observed; the ITO glass that is coated with nanoparticles appears to have more deposition on the edges of the glass, and less deposition at the center. This deposition behavior is difficult to explain, especially since the original article that this procedure was developed from reports very uniform deposition across the ITO glass surfaces.

When the ITO glasses that were coated in EPD trials 2 and 3 were held up to the NIR diode laser, both slides did exhibit upconversion luminescence (Figure 43). However, in comparison to the coated carboxylated glass slides, that were being produced concurrently, the observed luminescence was dim and of a lower quality. As one final test, both coated ITO slides were imaged using the final laser/microscope setup that was being used for the temperature sensitivity experiments, however there was little to no observed luminescence from either slide through either green or red filter cubes. This could be simply because of the lower concentration of nanoparticles in the IPA solution, compared to the nanoparticle solutions used to coat the carboxylated glass slides. In any case, while the coated ITO slides did exhibit upconversion luminescence which indicated the presence of nanoparticles on its surface, the focus of this research was shifted to the carboxylated glass experiments.

4.4 – Carboxylated Glass Deposition Experiments

The deposition of nanoparticles onto carboxylated glass had many challenges not unlike the other aspects of this research endeavor. The creation of the carboxyl functionalization on SiO_2 glass surfaces was performed by Pablo Mancheno, who followed a protocol

developed from the literature. All the glass surfaces were washed and cleaned prior to the carboxylation procedure, although the surface characteristics of those surfaces were varied for this research. There were three main glass surfaces that were used: 1) glass slides that had been simply cleaned and underwent the carboxylation procedure (unscratched) 2) glass slides that had been scratched with a diamond tipped pen to create a cross-hatch pattern, cleaned, and then underwent the procedure (scratched) 3) glass slides that had been sand blasted, cleaned, and then underwent the procedure (sand blasted). All three types of functionalized surfaces had varying degrees of success in the creation of the nanoparticle coatings.

Table 4 lists all of the glass surfaces that were created during the course of this experimentation. For many of the coatings, the dispersed nanoparticle sample was simply pipetted onto the functionalized surface in specified volumes. Nanoparticles were typically dispersed in volumes of 20 mL, yielding a solution concentration of 5 g nanoparticles / L (0.100 g / 20 mL).

Initial experimentation was performed using oleate-free nanoparticle samples and glass that had not underwent the carboxylation procedure. While these glasses did exhibit upconversion luminescence under 980 nm excitation from the diode laser, these coatings could be easily washed off with H_2O delivered via pipette to the glass surface. This was to be expected as there were no functional groups on the glass surfaces for the particles to associate with. Subsequent coatings were made on glass surfaces that had been

carboxylated, with some surfaces being scratched and some unscratched. The oleate-free samples were also dispersed in 3 different solvents; H_2O, acetone and isopropyl alcohol. The initial signs of success were seen with the creation of samples GE4 and GE5, coated with sample OAR6 in acetone. In both these trials, an excess volume of the nanoparticle solution was pipetted onto both unscratched and scratched glass surfaces, and was allowed to dry in the fume hood. Since sample OAR6 was dispersed in acetone, the resulting nanoparticle coating on the surface was non-uniform and irregular, which could be attributed to the fast evaporation of the acetone solution. When checked with the NIR diode laser, there was a visible upconversion luminescence signal. However, when these glasses underwent washes with H_2O, the coating was still being removed from portions of the glass. An upconversion signal could still be observed from the areas where the coating visibly appeared to be removed, but the signal intensity had significantly decreased. It is important to note that for the nanoparticles that deposited onto the glass surface in areas that had been scratched with the diamond tipped pen, for the most part those particles stayed in place despite repeated washes. This is expected given that more defects on the glass surface would promote attachment of the nanoparticles to the glass surface. If the assumption is made that for the unscratched glass, the carboxyl groups are for the most part vertically oriented away from the glass surface, there is very small contact area proportional to the total surface area of the nanoparticle where there can be interaction with the carboxyl groups. This problem is amplified even more when the size

of the oleate-free nanoparticle samples is taken into consideration, with particle diameters on the range of hundreds of nanometers.

To illustrate this point, a sample calculation can be performed for the contact area between a spherical nanoparticle and a flat surface if we assume the surface is an elastic half-space. The contact area of radius between the sphere and the surface follows the equation,

$$R = \sqrt{NR * D}$$

where R is the radius of the contact area, NR is the radius of the sphere, and D is the indentation depth. For the calculation, there is an assumed spherical nanoparticle diameter of 300 nm, which is on par with the nanoparticle diameters measured for many of the oleate-free nanoparticle samples, and an assumed surface indentation depth of 30nm, 10% of the nanoparticle diameter. In this case the radius of the contact area would be 67nm, for an effective contact area of 14137 nm^2. When compared to the total surface area of the nanoparticle, which is calculated to be 282743 nm^2, the contact area of the nanoparticle represents roughly 5% of the total surface area of the particle.

While certain assumptions were made in the calculation shown above, it can be assumed that for carboxylated surfaces that are unscratched, there will be relatively small contact areas between the charged nanoparticle surfaces and the carboxyl functionalization on the glass surfaces. However, if the glass surfaces are irregular and grooved, then the carboxyl groups will not all be vertically oriented, and some may be oriented at different angles. This in turn could help drive interaction between the particle surface and the carboxyl

groups, if the particles are located within the grooved areas. This helps explain the adhesion of nanoparticles within the scratched areas of the carboxylated glasses, even after H_2O washing.

Figure 44 shows images of some of the carboxylated glass surfaces that were able to be produced during the course of this experimentation. Sample GE10 is shown on the left, which was coated using a sample of oleate-free nanoparticles dispersed in IPA. As can be expected the coating is irregular and non-uniform, but shows nanoparticle adhesion within the grooved areas of the glass surface. Samples GE11 and GE12 were both created using oleate-free nanoparticles that were dispersed in H_2O, a larger sample volume was pipetted onto the proportionally larger glass surface. The coatings on these glass surfaces visually appear to be more uniform, although areas of higher and lower particle concentration can clearly be seen. Sample GE12 also shows nanoparticle adhesion within the grooved areas of the glass surface.

Many of the carboxylated glass surfaces that were both scratched and unscratched exhibited upconversion luminescence when held under the 980nm diode laser. In general, glasses that were coated using a higher concentration of nanoparticles obviously had better emission characteristics (stronger luminescence intensities). Figure 45 shows the emission spectra for sample GE10, which is consistent with the spectral data for the original $NaYF_4:Er^{3+},Yb^{3+}$ nanoparticles. Figure 46 shows the emission spectra for sample GE8 and the accompanying image of the glass exhibiting upconversion luminescence when held in front of the 980nm diode laser. However, while these glasses did exhibit

desirable upconversion luminescence properties, steps were still taken to form nanoparticle coatings that were more homogenous uniform.

The desire to create a more homogenous and uniform nanoparticle coating was the reasoning behind the use of sand blasted glass for carboxyl functionalization. The fact that the glass surfaces were sand blasted would essentially mean there would be more surface defects on the glass surface, which could only help nanoparticle adhesion once that surface was carboxylated. Using glass surfaces that had been uniformly sand blasted was also much more preferable to creating cross-hatch groove patterns in glass surfaces by hand, prior to the carboxylation procedure. Figure 48 depicts images of some of the coatings on sand blasted slides that were produced in the course of this research. All of the samples GE13, GE14, and GE15 were created by pipetting 200μL of sample OAR10-12 solution onto the functionalized glass surface. However, for the coating produced on sample GE14, the nanoparticles in the OAR10-12 solution were allowed to settle to the bottom of the vial before being pipetted onto the surface, whereas for GE13 and GE15, the nanoparticle solution was sonicated and was pipetted onto the glass surfaces. Therefore for GE14 there should be a substantially higher concentration of particles on the surface than for the other two samples. Upon visual inspection, the coatings on these sand blasted glasses appear to be more homogeneous, and the coated slides all exhibiting varying degrees of upconverison luminescence under 980nm excitation.

For a few of the glass surfaces, the nanoparticle coating on the functionalized glass surface were attempted to be created through a type of "dipping method", in which the

glass sample was dipped into the nanoparticle solution in hopes of creating a self-assembled layer of particles on the glass. This type of self-assembly was inspired by previous reports in the literature by a research group that had formed patterns of $NaYF_4:Er^{3+},Yb^{3+}$ onto patterned hydrophobic/hydrophilic surfaces by dipping the surfaces in solutions of the nanoparticles.[39] While that self-assembly method was driven by the affinity of the oleylamine capped nanoparticles to the hydrophobic surface regions, it was hypothesized that the charged nanoparticles in solution could also "self-assemble" onto the functionalized glass surfaces. Early attempts to try this dip coating with oleate-free nanoparticle samples in water (GE2) and oleate-capped nanoparticles in chloroform (GE3) did not appear to create coatings, and the slides did not exhibit any upconversion luminescence. This concept was again approached with the sand blasted slides that underwent carboxylation. A series of the glasses (GE16-GE19) were dipped into the sample OAR8 nanoparticle solution, that was lightly stirred to maintain a dispersed solution. Each glass was introduced to the solution for a different length of time; for GE16-19, the dipping time was 10 seconds, 1 minute, 2 minutes, and 48 hours respectively. However, for all the glasses that underwent the "dipping method", none of them exhibited observable upconversion luminescence signal under the 980nm diode laser, or the final laser/microscope setup. One possible reason for the absence of nanoparticle binding could be again the small contact area present between the nanoparticles and the surfaces. Therefore, these glasses were not used in the subsequent temperature sensitivity experiments.

Of the 19 samples that were created during this experimentation, only 2 samples, GE10 and GE14, were eventually used for the temperature sensitivity experimentation. Samples GE1-3 were created on surfaces that had not been carboxylated and the coatings were easily washed off, and samples GE16-19 were created using the dip method and exhibited no upconversion luminescence. There were many factors that went into this decision. Pipetting the nanoparticle solutions onto the glass surfaces, while sufficient to produce luminescent nanoparticle coatings, created coatings that were highly irregular and non-uniform. It would have been preferable to create uniform nanoparticle coatings via the dipping method, but this was not possible. Also many of the glass samples, while exhibiting good upconversion luminescence properties under the 980nm diode laser excitation source, did not produce images that could be analyzed in the final laser/microscope setup. This was the single greatest factor in choosing coated glass samples to use for the temperature sensitivity experimentation. For the carboxylated glasses that were not sand blasted, sample GE10 produced the best upconversion luminescence images in conjunction with the laser/microscope setup. For the sand blasted slides, GE14 produced the best images with the final laser/microscope setup. For GE14, this is most likely due to a much higher concentration of particles on the surface than the other sand blasted slides that were produced.

4.5 – Experimental Setup for Temperature Sensitivity Trials

As was true with the synthesis of upconverting nanoparticles and the oleate removal process, there were many challenges that had to be addressed with the experimental setup

for the temperature sensitivity trials. As was noted in section 2.1, the laser and microscope setup that was used for the temperature sensitivity experiments underwent numerous changes before a final and optimal setup was eventually obtained. Originally, the 980nm laser excitation was provided using a tunable optical parametric oscillator (OPO) pumped by a Nd:YAG laser. Since the MVX10 microscope was at this point simply resting on the optical table, the beam was directed to the stage plate of the microscope using 2 mirrors, as shown in figure 9. This initial setup had two very specific problems that led to its modification. First, given the position of the OPO laser, the microscope, and the 2 mirrors to direct the beam path, the laser beam itself was directed onto the microscope stage at an extremely wide angle. The resulting laser "spot" on the stage plate was essentially not a spot at all, and was more of a streak pattern that was highly non-uniform. Secondly, this original setup had no way of inducing temperature changes to the coated glass surfaces that were on the stage plate.

These issues led to the first major changes to the laser/microscope setup. The microscope itself was bolted to the optical table by using a modified base plate, and the microscope stage itself was replaced with a VWR hotplate/stirrer. To create a more well-defined laser spot on the microscope stage, now the hotplate, a dichroic mirror with a 45 degree angle of incidence was placed between the microscope objective lens and the hotplate, to direct the laser beam directly onto the hotplate and avoid this streak pattern. The extra dichroic mirror would also help block NIR excitation from being collected in the resulting luminescence images (Figure 10). However when this setup was used for the 1st

temperature sensitivity trial, significant problems arose. First, the power supply to the OPO laser could not be held constant and had significant fluctuations. To be able to demonstrate the ratiometric emission changes of the nanoparticles on the glass surfaces, the laser power and intensity had to be constant; otherwise there would be large variability in the nanoparticles' emission in the images collected through both the green and red filter cubes. This was clearly demonstrated in the temperature sensitivity trial 1, where essentially no relationship between the green-to-red emission ratio and temperature could be demonstrated (section 3.7). Secondly, because the dichroic mirror was positioned between the microscope objective lens and the hotplate, it impeded the ability to focus the microscope itself. This can clearly be seen in the images collected during the 1st temperature sensitivity trial that appear blurry and out of focus (Figure 56).

After careful consideration of the problems with the experimental setup that came to light during the 1st temperature sensitivity trial, a complete overhaul of the laser/microscope setup was performed. The decision was made to replace the OPO laser, mirrors, and dichroic mirror with the 980nm diode laser and accompanying power supply. The NIR excitation beam would be directed to the hotplate using a fiber optic with attached lens, to create a well-defined laser spot. There were certain tradeoffs with using the diode laser instead of the OPO laser. The laser power and intensity for the diode laser was much lower than the OPO, and the laser spot that was created with the diode laser was smaller than that created using the former setup. However, this eliminated the use of mirrors, which restored the ability to properly focus the microscope, and provided a stable

excitation source, which was crucial for these experiments. The oil bath that was used in the original setup for temperature feedback was also completely removed, and the hotplate thermometer was set to rest on the surface of the plate directly. This led to a final experimental setup where the user had much more control over experimental conditions, and which could provide a consistent, stable excitation source to the coated glass surfaces being imaged. For example, when the OPO laser and the mirrors were being used, any small adjustment to the laser spot position required changing the positions of all 3 mirrors, which was extremely time consuming and tedious. With the new setup, adjustment of the laser spot position required only changing the position of the lens on the end of the fiber optic cable, which could be performed with ease. Figures 12-13 show multiple views of the final experimental setup that was used for the subsequent temperature sensitivity experimentation.

The final aspect of the experimental setup for the temperature sensitivity trials that had to be addressed was the filter cubes that were assembled to isolate both the green and red emission bands of the upconverting nanoparticles on the glass surfaces. The objective was to isolate the 521nm and 668nm emission bands to create the green-to-red emission ratio. For both filter cubes, excitation filters were not necessary as the laser was not being directed through the microscope in a typical epifluorescence microscope setup. A 900DCSP dichroic mirror was chosen for both filter cubes to attenuate the 980nm excitation light, and its transmission data showed that it would still allow transmission of the emission bands of interest (Figure 53). For the red filter cube, the D655/40m emission

filter was used to isolate the emission around 668nm. Even with the previously observed small fluctuations in the red emission peak location (Figures 17-19), the transmission range between 636-673nm would allow for the isolation of the red emission in its entirety, while limiting the transmission of the 980nm excitation light.

For the green filter cube, the ET525/50m emission filter was used to isolate the 521nm emission range. The use of this emission filter had significant drawbacks. First, the transmission range for the filter allowed for 80% transmission between 501-547nm, which means that the 521nm emission peak would not be completely separated from the 541nm emission peak (Figure 55). This would hinder accuracy and precision of the calculated green-to-red emission ratios. Of even more concern was the fact that the filter transmits light in the range from 800nm-1000nm, with 2.84% transmission at 980nm. This increased transmission of the NIR excitation light could overwhelm the much weaker luminescence signal from the nanoparticles and could also hinder accuracy and precision when calculating the green-to-red emission ratio. There was only one main reason why the ET525/50m excitation filter was used, and that was because the procurement of an excitation filter designed for this specific experiment would have required a custom fabrication that would be extremely expensive and time consuming. Unfortunately, the U-MF/XL filter cube that works in conjunction with the Olympus MVX10 microscope only takes excitation filters of 32mm radius, which is much less common and more expensive than the standard 25mm radius excitation filters that are used in other microscopes. On top of this, a specific excitation filter could not be

purchased through any vendor that transmitted in the desired range of the green emission while also adequately blocking out the 980nm excitation range. A custom order placed with a microscope filter vendor for such a filter was going to be extremely costly, take about 1-2 months to fabricate, and even then could not be guaranteed to attenuate the 980nm excitation light. For these reasons, the ET525/50m excitation filter was eventually used for the green filter cube, and steps were taken to correct for its deficiencies.

The emission intensity data shown in Table 5 shows the emission intensity variability of the green emission in comparison to the red emission for a set of 16 images. For the green emission, the measured emission intensity ranges between 7441-12338 counts, while the emission intensity values for the red emission ranges between 3788-4103 counts. In order to correct for the deficiencies of the green filter cube, only the six smallest measured emission intensity values for both the green and red emission were used from any data set. As demonstrated through the calculations in section 3.6, this has little impact on the average emission intensity calculated for the red emission, but decreases the standard deviation and standard error of the average emission intensity for the green emission drastically.

4.6 – Temperature Sensitivity Experiments

The experimentation with the nanoparticle coated glass slides on their temperature dependent upconversion emission represented the culmination of this research study. A summary of the key data obtained from all of the temperature sensitivity experiments is shown in Table 6. The first experiment to be undertaken dealt with establishing emission

ratio curves for oleate-capped nanoparticles dispersed in chloroform, based on the collected spectral data. It should be noted that when the cuvette containing the nanoparticle dispersion in chloroform was heated using cuvette holder with the attached water circulator, that some of the chloroform did evaporate off. However, since ratiometric emission measurements were being taken, that compensated for any increase in nanoparticle concentration in the solution of chloroform during the experiment. When the emission ratios were constructed, the 521 nm/541 nm and 521 nm/668 nm ratios exhibited very linear dependences with respect to temperature (Figure 51). The 541 nm/668 nm ratio did exhibit a dependence on increasing temperature, but this dependence was not very linear, with an R^2 value of 0.674 (Figure 52). Between the 521 nm/541 nm and 521 nm/668 nm emission ratios, the focus for the subsequent temperature sensitivity experimentation was centered on the 521 nm/668 nm emission ratio. One reason for this is that the 521 nm/668 nm emission ratio could be tuned throughout a larger range (overall ratio change of 0.228) while the 521 nm/668 nm only had an overall ratio change of 0.105. Another reason was that it would be extremely difficult to isolate the 521 nm and 541 nm emission from the nanoparticles to pursue the other emission ratio, and would probably require the use of expensive, custom filters, which was to be avoided if at all possible (section 4.5). The reason that the data for the 521 nm/668 nm ratio and 541 nm/668 nm ratio is shown in Table 6 is because given the excitation filter used in the green filter cube and the fact that the 521 nm and 541 nm emission peaks were not

completely separated, the resulting overall green-to-red emission ratio will be some combination of these two calculated ratios.

Overall there were 7 temperature sensitivity experiments that were performed; 3 trials using scratched carboxylated sample GE10, 2 trials using sand blasted carboxylated sample GE14, 1 trial using a glass slide coated with oleate-capped nanoparticles in chloroform, and 1 trial where a coating of oleate-free nanoparticles was created on the surface of a 25 mL flask. The data from the first trial using GE10 can be completely omitted because that trial was conducted using one of the earlier laser/microscope setups that had multiple issues (section 4.5). A major concern was that the power supply for the OPO laser could not be held constant during the experiment, and this certainly affected the emission intensity from the nanoparticles at the various temperature intervals. Secondly, the dichroic mirror that was used to create a more uniform laser spot on the hotplate impeded the movement of the microscope objective lens. The resulting images could not be adequately focused and were unclear, and this too would have affected the accuracy and precision of the temperature measurement from the constructed GRR ratio. It is therefore not surprising that the results from this first temperature sensitivity trial demonstrate no linear relationship from the acquired data. For the remaining 6 trials, while the temperature range that the coated glasses were cycled through did vary slightly, most covered the temperature range from 20-50°C (Table 6). For trials 2 & 3 which involved scratched, carboxylated sample GE10, the ΔGRR was 2.567 and 0.981 respectively. When this was calculated with respect to the temperature range the sample

was subjected to for each trial, the ΔGRR/ΔT was 0.0655 and 0.0334 respectively. In both trials 2 & 3 the calculated green-to-red emission ratio exhibited very linear dependences with respect to increasing temperature, with R^2 values of 0.9650 and 0.9685 respectively. For trials 4 & 5 which involved sand blasted, carboxylated sample GE14, the ΔGRR was 6.36 and 3.88 respectively, and the calculated ΔGRR/ΔT for both trials were 0.2156 and 0.1603 respectively. In both trials 4 & 5 the calculated green-to-red emission ratio exhibited very linear dependences with respect to increasing temperature, with R^2 values of 0.9980 and 0.9895 respectively. For trial 6, which involved the oleate-capped nanoparticles deposited onto a plain glass slide, the ΔGRR was 0.63, the calculated ΔGRR/ΔT was 0.0213, and the R^2 value for the linear trend line was 0.9435. Finally, for trial 7, which involved the nanoparticle coating created on the flask label, the ΔGRR was 0.06, the calculated ΔGRR/ΔT was 0.0022, and the R^2 value for the linear trend line was 0.9832.

The values for the ΔGRR/ΔT performance metric varied drastically between the temperature sensitivity trials. While there were differences in exposure time and the temperature range that each of the coated glass surfaces were subjected to, because the constructed GRR value is a ratiometric measurement, and the ΔGRR/ΔT takes into account the overall change in temperature, these experimental variables should not drastically vary the ΔGRR/ΔT performance metric. There were also significant differences in the ΔGRR/ΔT of repeated trials using the same glass sample (Trials 2-3, Trials 4-5). After review of the data, one possible cause of this inconsistency between

repeated trials is the pixel area that was used to measure average emission intensities for each trial. Often times between trials the position of the fiber optic and lens had changed in relation to the microscope stage, so the resulting laser spot size that was created on the coated glass surfaces were varied. As a result, the pixel area that was then used to calculate the average emission intensity from the gathered images was then adjusted to accommodate the laser spot size.

Take for example the data from temperature sensitivity trials 2 and 3. Pixel areas of 10625 pixels and 16906 pixels were used to analyze the data for trials 2 and 3 respectively. It would have been ideal to use the same pixel area to measure average emission intensity between the two trials. However, the position of the fiber optic and attached lens had been changed, which resulted in a larger laser spot size on the coated glass surface, and therefore a larger pixel area used to analyze the images from the 3rd trial. Figures 59 and 62 corresponding to images taken during trials 2 and 3 respectively, show significant areas of darkness (low intensity values) even within the area created by the laser spot size. The increased pixel area used to calculate the average emission intensity in the trial 3 data could have incorporated proportionally more dark space into the emission intensity measurement, decreasing the respective emission intensity measurements for the green and red emission, and skewing the calculated values for ΔGRR and ΔGRR/ΔT. Despite the differences between the two sets of data, both trials show good linear dependence of the green-to-red emission ratio on increasing temperature for sample GE10.

The same can be said for the data from temperature sensitivity trials 4 and 5. In this case the exposure time used to collect the images were the same and the temperature range that the coated glass samples was subjected to for each trial were comparable. However for trial 4 a pixel area of 10625 pixels was used to measure the average emission intensity from the collected images, and for trial 5, a pixel area of 6900 was used, as the fiber optic and lens had been moved closer to the sample, creating a smaller laser spot size. Figures 65 and 68 corresponding to images taken during trials 4 & 5 respectively, again show significant areas of darkness (low intensity values). The difference in pixel areas used to calculate average emission intensities could again account for the differences seen in the $\Delta GRR/\Delta T$ performance metric. But again, despite the differences between the two sets of data, both trials show good linear dependence of the green-to-red emission ratio on increasing temperature for sample GE14.

To directly compare the $\Delta GRR/\Delta T$ performance metric to see which type of coated glass performed better and produced the desired temperature sensitivity characteristics, trial data must be selected where the pixel area used to calculate the average emission intensities was kept constant. To do this, data for trials 2 (GE10), 4 (GE14), and 6 (oleate-capped nanoparticles) will be scrutinized, all of which used 10625 pixels to calculate emission intensity data. For GE10, the scratched, carboxylated slide, the $\Delta GRR/\Delta T$ was 0.1041; for GE14, the sand blasted, carboxylated slide, the $\Delta GRR/\Delta T$ was 0.2156; and for trial 6 which utilized oleate-capped nanoparticles on plain glass, the $\Delta GRR/\Delta T$ was 0.0213. It should be noted that even though the same volume of

nanoparticle solutions were pipetted onto each glass slide, the relative concentrations of nanoparticles in those solutions were not identical. The oleate-capped nanoparticles that were deposited on the plain glass slide were at the highest original concentration, of about 0.4 g/6 mL chloroform, whereas GE10 was coated using sample OAR9 at a concentration of 0.1 g/20 mL IPA, and GE14 was coated using sample OAR10-12 at a concentration of 0.3 g/20 mL H_2O. Despite this variation in concentration, from this data, it would appear that the best candidate for a coated glass surface for use as a temperature sensor would be the sand blasted glasses that were later carboxylated. One trend that was interesting to note was that for the experimental trials involving oleate-capped nanoparticles (521 nm/668 nm emission ratio, 541 nm/668 nm emission ratio, trial 6), the ΔGRR and ΔGRR/ΔT values are much lower than that for the experimental trials involving coatings produced with nanoparticles that underwent the oleate-removal process. For trials involving oleate-capped nanoparticles, the ΔGRR and ΔGRR/ΔT values ranged between 0.63-0.228 and 0.0046-0.0213 respectively. For the trials involving oleate-free nanoparticles (trials 2-5), the ΔGRR and ΔGRR/ΔT values ranged between 0.981-6.36 and 0.0334-2156 respectively. This indicates that the presence of the oleate ligand on the surface of the nanoparticles had an effect on the average emission intensity with respect to temperature and therefore overall temperature sensitivity of the nanoparticles. The Capobianco group does report this trend as well, stating that the removal of the oleate ligands from the nanoparticle surfaces has an effect on the red-to-green emission ratio, as well as increasing upconversion luminescence

intensities.[31] Absence of the oleate ligand from the nanoparticle surfaces may affect the non-radiative relaxation of the excited photons in the Er^{3+} ions, decreasing population of both the green and red emission pathways.

In contrast to the other nanoparticle coatings that were constructed using nanoparticles that had undergone the oleate removal process, the nanoparticle coating created on the label of the 25 mL flask exhibited small changes in the ΔGRR and ΔGRR/ΔT values. The coating created on the flask label formed a well-defined spot (Figure 74), and the calculated green-to-red emission ratio showed a linear dependence on temperature with an R^2 value of 0.9832 (Figure 77). However, the ΔGRR was only 0.06, ranging between 0.47-0.53, and the ΔGRR/ΔT was calculated to be 0.0022. These values are even lower than those exhibited by the coatings made with oleate-capped nanoparticles, and are not consistent with the expected ΔGRR range and ΔGRR/ΔT values for a coating constructed using oleate-free nanoparticles. Compared to the other coated glass samples, the green upconversion luminescence signal was drastically reduced. As there was no difference in the type of nanoparticles used in this experiment than those used in temperature sensitivity trials 4 and 5, it can be assumed that the discrepancies in this experiment are due to the experimental conditions. First, this nanoparticle coating was not created on bare glass that had been modified (sand blasted) and then carboxylated. The decision was made to pipette the nanoparticle solution over the flask label in order to help adhesion of the solution to that particular spot, instead of having it run down the length of the flask. Since the flask level is mad of a durable white ceramic paint material, there could be

some interaction occurring between the ceramic paint and the nanoparticle coating that is quenching the green upconversion luminescence. Also, the imaging of this flask was performed in such a way that the nanoparticle coating was not exactly perpendicular to the microscope objective lens as was the case in the previous experiments. The flask had to be positioned upright so the 1-octadecene solution that was being heated was kept in the flask. As can be seen in the images in figure 75, the nanoparticle coating is being imaged at an angle, which could have had an effect on the luminescence intensity that was exhibited by the coating. Finally, because the coating was imaged at an angle, the pixel area that was needed to measure the average emission intensity from the entire coating on the flask label was only 4484 pixels, smaller than any of the other pixel areas used in these experiments. Given the earlier discussion about how the pixel area can skew the green-to-red emission ratio results, that could also be the case in this trial. Nevertheless, while the flask coating did not exhibit a large ΔGRR or ΔGRR/ΔT, a linear dependence with respect to temperature was demonstrated, with an R^2 value of 0.9832. With regard to the specific aims set forth for the temperature sensitivity experiments, it was difficult to set expectations for the ΔGRR and ΔGRR/ΔT values as reports in the literature are often varied. It can be stated that for all temperature sensitivity trials, excluding the 1st trial using the OPO laser, that well defined linear relationships with R^2 values approaching 1.0 were demonstrated over the approximate physiological temperature range from 20-50°C. Unfortunately, for the 2 sets of repeated trials, using GE10 and GE14, the same temperature dependence could not be reproduced, and the

ΔGRR and ΔGRR/ΔT values were varied. However this may in fact be due to experimental conditions (pixel area) not being kept constant, and subsequent experiments with those two coated glass samples under the same conditions may demonstrate the same temperature dependence.

4.7 – Stability of Nanoparticle coating on glass

It was reported in section 3.4 that many of the nanoparticle coatings that were created on the carboxylated glass surfaces could be easily washed off with H_2O delivered via pipette. Due to this, the stability of the nanoparticle coating created on the two functionalized glasses that were used in the temperature sensitivity experimentation was investigated. For both samples GE10 and GE14, 2 washes with nanopure H_2O delivered via pipette were performed, and the samples were allowed to dry in the fume hood. Figure 78 shows images of the two glass samples before and after the H_2O washes. Upon visual inspection, it appeared that the coatings on both GE10 and GE14 had not been adversely affected by the washes. Both samples still exhibited bright upconversion luminescence properties when held in front of the 980nm diode laser. However, while a visual inspection of the coatings was a good start, more definitive proof was needed that the nanoparticle coating on the functionalized glasses was stable.

Figure 79 shows spectral data obtained from sample GE10 before and after the H_2O washes, using the exact same experimental conditions. Both the emission spectra exhibit well defined emission pekas in the 532nm, 541nm, and 660nm emission regions, consistent with the NaYF4:Er^{3+},Yb^{3+} nanoparticles. However, after the washing stage,

there is a marked intensity decrease of all of the emission peaks from the nanoparticles across the board. After washing, the 523nm peak intensity decreased by 11.03%, the 541nm peak intensity decreased by 10.70%, and the 660nm peak intensity decreased by 23.67% (Table 7). This intensity decrease observed in all of the emission peaks after washing the surface of GE10 indicates that while the majority of the nanoparticles on the glass surface remained after the washing, that there was a significant amount of the particles that were washed off as well. This again relates back to the discussion on the contact area between the large nanoparticle aggregates and the flat glass surfaces. If only a small percentage of the nanoparticle surface area is interacting with the carboxyl groups on the glass surface, it may be relatively easy to wash those large aggregates off of the surface with H_2O. Unfortunately with the current setup in the laboratory, it was not possible to obtain spectral data from the sample GE14 slide. Given that washing the GE10 sample with water caused a decreased mark in emission intensity, it cannot be claimed that the specific aim of creating a coating with a stable adhesion to the glass surface was achieved.

4.8 – 2D Temperature Distribution Map

The creation of a 2D temperature distribution map from the microscope images collected during the temperature sensitivity experimentation was always a secondary objective during the course of this research. Figure 80 shows the images that were collected during the 8^{th} temperature sensitivity trial, where those images were then used to try and create the 2D temperature map.

The top set of images in figure 80 depict the location of the aluminum cylinder, the laser spot being well aligned with said cylinder, and sample GE14 resting atop the cylinder. The rationale behind this experiment was to transfer heat to the GE14 glass sample through the aluminum cylinder that had a high thermal conductivity, and visualize the temperature distribution on the glass slide through construction of the Green-to-Red emission ratio across the sample. If successful, a temperature distribution similar to a point spread function could be observed, with a point of high temperature corresponding to the location of the middle of the aluminum cylinder, with the temperature slowly dissipating radially outwards. The slide was allowed to reach 37°C, and then images were taken through both the green and red filter cubes. Once background subtraction was performed, the images were themselves divided using the ImageX software, to provide a green-to-red emission profile across the entire glass sample. That 2D temperature distribution map is shown in the middle right panel of figure 80. While it does appear that the emission map does show some temperature distribution within the area corresponding to the diode laser excitation spot, this distribution is not well defined. It can also be observed that at the fringe of the laser excitation spot, there are edge effects that are occurring, most likely arising from areas of the image where an intensity value of the green emission is being divided by an even smaller or absent intensity value from the red emission which creates a sort of laser speckling pattern.

When this experiment was attempted again with sample GE14 resting directly on the hotplate, the emission map created looks similar, if not identical, to the map created in the

previous trial. Since the sample is now resting directly on the hot plate, the temperature distribution should be more uniform, resulting in a more uniform Green-to-Red emission map, at least within the confines of the laser spot size. However, this temperature distribution is again not well defined, and speckling patterns can again be observed at the edges of the laser excitation spot. The fact that the two emission maps created under the same experimental conditions appear to be so similar leads to the theory that this temperature distribution that is being seen is less of a result of the actual temperature distribution on the sample itself, and more of a result of the diode laser spot size and distribution of the excitation light from the fiber optic and the lens. This is reinforced by the fact that if the temperature distribution maps are compared to the image of the laser spot taken without an excitation filter, shown in the top middle panel of figure 80, the images look very similar. Therefore while the current laser/microscope setup that was used for experimentation can be used to make cumulative temperature measurements for a spot on a nanoparticle coated slide, trying to determine a temperature distribution along the slide is beyond the detection limits of the current system.

Section 5

FUTURE WORK

5.1 – Synthesis of Lanthanide Doped Nanoparticles

While the synthesis of lanthanide doped nanoparticles was in the end shown to be reproducible in terms of particle size, clear sample dispersions, and luminescence quality, there are still areas in which the synthesis process can be improved. Most of these improvements deal with the secondary synthesis reaction in which the lanthanide trifluoroacetate precursors are used to form the nanoparticles in the presence of 1-octadecene and oleic acid. Before the lanthanide trifluoroacetate precursors are used in the secondary synthesis reaction, they could undergo more drying stages to ensure the removal of all traces of water. The precursors could be dried over phosphorus pentoxide (P_2O_5), calcium hydride (CaH_2), or a variety of other dessicants. This could be done after the lyophilization step, while the precursors are being stored to be used in the secondary synthesis reaction, to ensure dryness even after the lyophilization process has been complted. This could also be done after the precursors have been introduced to the three neck flask, by purging the glass with argon, and flaming. In the experimental setup for the secondary synthesis reaction, it would be extremely beneficial to have an adapter with a valve, to switch between the alternating vacuum and argon lines during argon purging, such as a schlenk line. The current method involved physical removal of the adapter that had the argon line and replacement with the vacuum line, and vice versa during argon purging. This constant switching between adapters hinders the removal of all traces of

oxygen in the reaction flask, which is of the utmost concern with this synthesis. Secondly, the heating jacket with accompanying Glas-Col PowerTrol temperature controller that was used for thermocycling during the secondary synthetic reaction (Figure 5) could be replaced by a heating method that allows for more precise control of the temperature. This synthetic method that was used to synthesize lanthanide-doped nanoparticles requires precise temperature adjustments and thermocycling; this deals with the need to have two well defined nucleation and growth phases to form the nanoparticle crystal structure. Working with this heating setup, it took many syntheses to determine the correct power settings to achieve the desired temperatures and heating rates (10°C/min), and even then there was a certain amount of variability between syntheses. For example, if the temperature controller power setting was adjusted down only when the flask temperature reached the desired temperature, say 300°C, the flask would continue being heated up to around 320°C. Using a trial and error method, it was determined that if the temperature control was adjusted down around 285-290°C, then the temperature would settle in the 300-310°C range. Even small changes in the temperature of the reaction could affect the growth stage of the particles, and could contribute to the large particle diameters that were observed in some sample, as well as decreased luminescence intensities. Therefore for future syntheses, a heating jacket with a temperature controller that has much more effective temperature feedback, or that could perhaps be programmed with specific thermocycling steps, would be extremely useful.

With regard to nanoparticle sample consistency, more characterization of a wider range of samples could be performed. The XRD characterization shown in Figures 21-22 did confirm the α-phase $NaYF_4$ crystal structure, but this was only performed on a small fraction of the total number of samples synthesized (Table 1). It would be interesting to perform XRD characterization on a wider range of sample, and see if there was a possible correlation between the quality of the crystal structure and particle diameter or luminescence quality. Using the same rationale, it would be beneficial to collect either transmission electron microscopy (TEM) or scanning electron microscopy (SEM) images of the particles themselves. This was one area of particle characterization that was planned, but due to time constraints could not be performed. Either type of electron microscopy images that can be gathered could be used to validate the particle sizing measurements gathered via dynamic light scattering (Table 1), and could also be used to validate the cubic-phase crystal structure that is expected.

As has been mentioned previously, during the course of this research there were a large number of nanoparticle samples that were synthesized, and many were never used in subsequent experiments due to factors such as coloration of dispersed samples, large particle diameters, and undesirable luminescence quality. It would be beneficial to work with these existing nanoparticle samples to see if these samples can be refined through repeated precipitation and centrifugation, multiple washing stages, or filtration through nanopore filters. Any post-synthesis experimental steps that can be performed to improve the quality of the dispersed nanoparticle samples may enable the next researcher to not

have to synthesize such a large quantity of samples, and pick and choose which samples to use for subsequent procedures.

5.2 – Oleate Removal Procedure

It is clear from the results shown for the oleate removal process, that more investigation is necessary in order to optimize and perfect this procedure. The final procedure that was settled on for this research vastly differed from the original procedure outlined by the Capobianco group[31]. It may be beneficial to attempt the oleate removal process again, using experimental conditions kept as close as possible to the original synthesis method. Details of the extraction method for removing the oleic acid after the process has taken place are still unclear. In this research, hexane was chosen for the liquid-liquid extraction after initial extraction with diethyl ether did not produce good results, and was chosen for its abundance, safety concerns, and the fact that oleic acid has good affinity for hexane. Performing the extraction with diethyl ether and experimenting with various extraction times may yield a more optimal method for removing oleic acid from the solution once the oleate is stripped from the nanoparticle surfaces. Experimentation with other extraction techniques could also lead to a more optimal oleate removal process. A soxhlet extractor could be used as an alternative method of removing the hexane layer. While this apparatus was originally designed to extract lipids from solid material, it can be used to extract the oleate in this process. In a soxhlet extractor, the nanoparticles would be placed in a filter trap, and hexane is continually distilled and condensed over the trap. The oleic acid would move into the hexane layer as it moves through the filter trap, and would not

be present when the hexane was later condensed over the filter trap again. In this manner, the nanoparticles can be repeatedly filtered using pure hexane, which may aid in the oleic acid extraction. Yet another possibility is to use an anion exchange column to try and remove the oleate ligands from the nanoparticle surfaces, by separating the charged nanoparticles from the oleate ligands. This technique will work even though the nanoparticles are insoluble with the oleate ligands on their surfaces, as Dowex resins allow large particles to pass through the exchange column.

Nanoparticle diameters were again of a huge concern with this stage of the research, and there are obvious inconsistencies between particle diameters of originally synthesized oleate-capped nanoparticles and then those same nanoparticles after the oleate removal process has occurred. As with the originally synthesized nanoparticles, obtaining TEM/SEM images would allow for a direct comparison of particle size. This would allow determination of whether the larger particle size is due to aggregation of the smaller particles, or if after the oleate removal process these are actually larger, discrete particles. FTIR characterization could also be performed on a wider range of samples, to ensure that the removal of the oleate from the nanoparticle surfaces is being performed successfully on a sample to sample basis.

As was noted in the discussion (section 4.2), a better method of drying the nanoparticles could also lead to a decrease in particle diameters of the nanoparticles that undergo the oleate removal process. The current method of drying the nanoparticles resulting in a dry precipitate of nanoparticles that had to be broken up via mechanical methods. Recently, a

member of our research group that does similar work with nanoparticles, Chris Gainer, has found a more efficient way of drying nanoparticles that does not result in this aggregation. By dispersing the nanoparticles in tert-butanol and then undergoing a lyophilization process, similar to the lyophilization stage after the initial synthesis reaction in this research, the resulting dried nanoparticles are more evenly dispersed in a powder form, instead of as a dried precipitate. This is similar to methods used to dry lipids in a uniform manner. It goes without saying that if the nanoparticles are more evenly dispersed before the oleate-removal process is performed, there should be less aggregation, and more oleate removal from the nanoparticle surfaces overall.

The eventual end goal should be to create oleate-free nanoparticles that have relatively the same particle diameters as the original oleate-capped nanoparticles themselves, and that form stable colloidal dispersions in water. Dispersed nanoparticle samples should come to a point where two consecutive particle sizing measurements can be performed without much variation in the measured particle diameters between the two trials. If colloidal dispersions can be obtained, then a good next step would be to gather emission spectral data from those dispersions, and see if the spectral emission matches up closely with the original oleate-capped nanoparticles. The emission 521 nm/668 nm and 541 nm/668 nm emission ratios could also be constructed using this data, and the temperature dependence of the oleate-capped nanoparticles in solution could be demonstrated.

Finally, with these colloidally stable oleate-free nanoparticles, the relationship between

zetapotential and pH should be investigated more thoroughly, as there was significant variation with the results gathered during the course of this research.

5.3 – Carboxylated Glass Experiments

The method of creating nanoparticle-coated carboxylated glass surfaces in this research was sufficient in being able to test the temperature sensitivity of those created coatings, but this process could be optimized significantly. Delivering the nanoparticle solutions to the surfaces via pipette was a good starting point, but there is an obvious lack of control regarding the deposition of the nanoparticles onto the glass; where the particles are located when the solvent dries on the glass is where the particles will stay. Eventually it would be preferable to have a single layer or a controlled layer of nanoparticles on the functionalized glass surfaces. Ideally, some form of self-assembly of the particles onto the functionalized glass would be desirable. To this extent, the dipping method of coating the glasses should be revisited, and performed using oleate-free nanoparticle samples that are tuned via pH to have highly positive zeta potentials, indicating high surface charge. Smaller particle sizes will also potentially improve the deposition process, as a larger contact area proportional to total nanoparticle surface area (Section 4.4) will be available to interact with the carboxyl groups on the glass surface. Since the sand blasted slides that were functionalized and coated seemed to produce coatings that had optimal temperature responsiveness, these are the glass surfaces that should be used at least initially in future experimentation. Additional experimentation could also be performed to determine whether the SiO_2 glass surfaces could be functionalized with different functional groups

of compounds. For example, a chelating complex on the glass surface could also allow for attachment of the lanthanide-doped nanoparticles. 1,4,7,10-tetraazacyclododecane-1,4,7,10-tetraacetic acid or DOTA as it is commonly known, is an organic compound that is commonly used as a chelator complex for lanthanide ions. It very well may be possible to use a similar complex that is larger to bind the lanthanide-doped nanoparticles.

5.4 – Electrophoretic Deposition Experiments

The experimentation with electrophoretic deposition of the charged oleate-free nanoparticles onto ITO glass could and should be revisited in the future. The results that were produced during this research did indicate that coatings of nanoparticles were produced onto the ITO glass. It was simply because these coatings were highly irregular, and the fact that the upconversion luminescence intensity from the glasses was much lower in comparison to the carboxylated glasses, that this research endeavor was halted. Future experiments could vary the concentration of nanoparticles dispersed in the IPA solution, as well as vary the applied voltage, plate distance, and deposition time.

5.5 – Stability of the Nanoparticle Coatings on Glass Surfaces

For nanoparticle coated glasses created by both the carboxylated glass and electrophoretic deposition methods, greater stability of the coating on the glass needs to be demonstrated. An experimental setup should be constructed where the emission spectra data from the surface of glass sample GE14 can be obtained. For future glass surfaces that are coated, TEM and SEM images of those surfaces before and after washing could also shed some light on the stability of the nanoparticle coatings. A final

thought would be to wash the glass surfaces not just with nanopure water but with buffer solutions in the acidic and basic pH ranges, to test the resiliency of the coating. If the oleate-free nanoparticles can have their zeta potential tuned between the positive and negative ranges, then using acidic or basic buffer solutions to wash the nanoparticle coatings may result in detachment of the particles from the glass surface, if those buffer solutions can protonate or deprotonate the particle surfaces.

5.6 – Laser/Microscope Experimental Setup

The capabilities of the laser and microscope setup in this research really set the limits for what could be performed regarding the temperature sensitivity experimentation. Improvements to the existing setup could drastically increase its capabilities. Instead of using a fiber optic cable and a lens to create a laser spot on the microscope stage, the use of more optics could allow for wide field illumination using collimated light. If the entire field of view of the camera can be illuminated with NIR excitation light, this would do two things. First, there would no longer have to be a decision on what pixel area to use to analyze the green and red emission images. Many times during the temperature sensitivity experiments, the fiber optic and lens was moved or disconnected due to the diode laser power supply being a high use item in the laboratory. When this was done, the lens position changed slightly and had to be readjusted, but this almost invariably changed the laser spot size. When the laser spot size changed, the pixel area used to analyze the emission from that spot also had to be corrected. If wide field illumination could be employed, then this problem would be completely resolved. Secondly, using

wide field illumination it may then be possible to construct the 2D temperature distribution map across coated glass slides, instead of taking average emission intensities across an area of the slide to determine one temperature value. Perhaps the NIR beam could be directed through the microscope as in a standard epifluorescence setup, as the Olympus MVX10 microscope is set up for. This would allow for the excitation light to be directed vertically downwards onto the microscope stage to provide widefield illumination using collimated light, and would avoid problems such as streaking effects and irregular laser spot sizes, resulting from having the excitation light delivered at an angle to the stage plate.

Another improvement that can and should be made to the experimental setup is replacing the ET525/50m excitation filter that was used in the green filter cube. While this would be costly and time consuming to have such a filter fabricated for the specific needs of this experiment (isolating the 521 nm emission while completely blocking the 980 nm excitation light), this would eliminate the high degree of variability in emission intensity between consecutive images taken through the green filter cube. This would also eliminate the need to manually correct for the deficiencies of the filter by choosing the lowest 6 emission values for both the green and red emission when calculating the green-to-red emission ratio (Section 3.6).

Finally, a better method for varying the temperature of the coated glass samples could be introduced. The VWR hotplate/stirrer provided adequate control for this initial study, but could really only be tuned in 1-2°C increments at a time. This hindered the ability to

determine the true detection limit of what temperature change could be actually detected using the glass slides. A more sensitive and stable temperature control method would allow for the investigation of the true sensitivity of the temperature sensing capabilities of the upconverting glass slides.

5.7 - Temperature Sensitivity Experiments

For future experimentation regarding the temperature sensitivity of the upconverting glass slides, the improvements to the existing laser/microscope setup will allow for better temperature sensitivity experimentation to be performed. Using wide field illumination and utilizing the entire field of view of the CCD camera will allow for green and red emission data to be collected over the entire coated glass area. However, factors such as temperature range and exposure times for collecting images should be standardized for repeated experiments, so that those results can be directly compared (Section 4.6). In addition to this, it would be beneficial to monitor the emission spectral data from the nanoparticles on the glass surface during subsequent temperature sensitivity experiments. In doing so, the GRR ratio constructed through the intensity measurements from the collected images can be compared to the 521 nm/668 nm GRR ratio constructed from the spectral data, and checked for any discrepancies. The 521 nm/541 nm emission ratio could also be monitored in addition to this, to help improve the precision and accuracy of the temperature measurements. As for the nanoparticle coating created on the flask, attempts should be made to form a spot of the coating on an area of the 25mL flask that is

not originally coated with the white ceramic material, to see if that has an effect on the $\Delta GRR/\Delta T$ of this new coating on the flask.

Appendix A

Abbreviations

OA – oleate

OAR – oleic acid removal

GE – glass experimentation

EPD – electrophoretic deposition

GRR – green-to-red emission ratio

ΔGRR – change in green-to-red emission ratio

ΔGRR/ΔT – change in the green-to-red emission ratio with respect to change in temperature

NIR – near-infrared

NP – nanoparticle

COOH – carboxyl group

References

1. Auzel, F. (2004). Upconversion and anti-Stokes processes with f and d ions in solids. *Chemical reviews*, *104*(1), 139-73.
2. S.G. Grubb, K.W. Bennett, R. S. C. and W. F. H. (1992). CW Room-temperature blue upconversion fibre laser. *Electronic Letters*, *28*(13), 1243-1244.
3. Silversmith, a. J., Lenth, W., & Macfarlane, R. M. (1987). Green infrared-pumped erbium upconversion laser. *Applied Physics Letters*, *51*(24), 1977.
4. Gamelin, D. R., & Gu, H. U. (1998). Two-Photon Spectroscopy of d 3 Transition Metals: Near-IR-to-Visible Upconversion Luminescence by Re 4+ and Mo 3+, (8), 12143-12144.
5. Vennerberg, D., & Lin, Z. (2011). Upconversion Nanocrystals: Synthesis, Properties, Assembly and Applications. *Science of Advanced Materials*, *3*(1), 26-40.
6. Auzel, F. (1990). Upconversion Processes in Coupled Ion Systems. *Journal of Luminescence*, *45*, 341-345.
7. Aebischer, A., Hostettler, M., Hauser, J., Krämer, K., Weber, T., Güdel, H. U., & Bürgi, H.-B. (2006). Structural and spectroscopic characterization of active sites in a family of light-emitting sodium lanthanide tetrafluorides. *Angewandte Chemie (International ed. in English)*, *45*(17), 2802-6.
8. Aebischer, A., Heer, S., Biner, D., Krämer, K., Haase, M., & Güdel, H. U. (2005). Visible light emission upon near-infrared excitation in a transparent solution of

nanocrystalline β-NaGdF4: Yb3+, Er3+. *Chemical Physics Letters*, *407*(1-3), 124-128.

9. Haase, M., & Schäfer, H. (2011). Upconverting nanoparticles. *Angewandte Chemie (International ed. in English)*, *50*(26), 5808-29.
10. Suyver, J. F., Grimm, J., van Veen, M. K., Biner, D., Krämer, K. W., & Güdel, H. U. (2006). Upconversion spectroscopy and properties of NaYF4 doped with Er3+,Tm3+ and/or Yb3+. *Journal of Luminescence*, *117*(1), 1-12.
11. Menyuk, N. (1972). NaYF4 : Yb,Er—an efficient upconversion phosphor. *Applied Physics Letters*, *21*(4), 159.
12. T. Kano, T. Suzuki, A. Suzuki, S. Minagawa, J. Electrochem. Soc. 1973, 120, C87
13. van der Ende, B. M., Aarts, L., & Meijerink, A. (2009). Lanthanide ions as spectral converters for solar cells. *Physical chemistry chemical physics : PCCP*, *11*(47), 11081-95.
14. Fischer, L. H., Harms, G. S., & Wolfbeis, O. S. (2011). Upconverting nanoparticles for nanoscale thermometry. *Angewandte Chemie (International ed. in English)*, *50*(20), 4546-51.
15. Singh, S. K., Kumar, K., & Rai, S. B. (2009). Er3+/Yb3+ codoped Gd2O3 nano-phosphor for optical thermometry. *Sensors and Actuators A: Physical*, *149*(1), 16-20.

16. Vetrone, F., Naccache, R., Zamarrón, A., Juarranz de la Fuente, A., Sanz-Rodríguez, F., Martinez Maestro, L., Martín Rodriguez, E., et al. (2010). Temperature sensing using fluorescent nanothermometers. *ACS nano*, *4*(6), 3254-8.

17. Santos, P. V., Araujo, M. T. D., Neto, J. A. M., & Sombra, A. S. B. (1999). Optical Thermometry Through Infrared Excited Upconversion Fluorescence Emission in Er - and Er – Yb -doped Chalcogenide Glasses, *35*(2), 395-399.

18. Yu, X., Song, F., Zou, C., Luo, L., Ming, C., Wang, W., Cheng, Z., et al. (2009). Temperature dependence of luminescence behavior in Er3+/Yb3+ co-doped transparent phosphate glass ceramics. *Optical Materials*, *31*(11), 1645-1649. Elsevier B.V.

19. Boyer, J.-C., Vetrone, F., Cuccia, L. a, & Capobianco, J. a. (2006). Synthesis of colloidal upconverting NaYF4 nanocrystals doped with Er3+, Yb3+ and Tm3+, Yb3+ via thermal decomposition of lanthanide trifluoroacetate precursors. *Journal of the American Chemical Society*, *128*(23), 7444-5.

20. Gainer, C. F., Joshua, G. S., De Silva, C. R., & Romanowski, M. (2011). Control of green and red upconversion in NaYF4:Yb3+,Er3+ nanoparticles by excitation modulation. *Journal of Materials Chemistry*, *21*(46), 18530.

21. Ostrowski, A. D., Chan, E. M., Gargas, D. J., Katz, E. M., Han, G., Schuck, P. J., Milliron, D. J., et al. (2012). Controlled Synthesis and Single-Particle Imaging of Bright , Sub-10 nm Lanthanide-, (3), 2686-2692.

22. Li, Z., & Zhang, Y. (2008). An efficient and user-friendly method for the synthesis of hexagonal-phase NaYF(4):Yb, Er/Tm nanocrystals with controllable shape and upconversion fluorescence. *Nanotechnology*, *19*(34), 345606.

23. Liu, Q., Li, C., Yang, T., Yi, T., & Li, F. (2010). "Drawing" upconversion nanophosphors into water through host-guest interaction. *Chemical communications (Cambridge, England)*, *46*(30), 5551-3.

24. Wang, Y., Wong, J. F., Teng, X., & Lin, X. Z. (2003). Pulling Nanoparticles into Water : Phase Transfer of Oleic Acid Stabilized Monodisperse Nanoparticles into Aqueous Solutions of r-Cyclodextrin. *Nano*.

25. Johnson, N. J. J., Sangeetha, N. M., Boyer, J.-C., & van Veggel, F. C. J. M. (2010). Facile ligand-exchange with polyvinylpyrrolidone and subsequent silica coating of hydrophobic upconverting beta-NaYF(4):Yb(3+)/Er(3+) nanoparticles. *Nanoscale*, *2*(5), 771-7.

26. Boyer, J.-C., Manseau, M.-P., Murray, J. I., & van Veggel, F. C. J. M. (2010). Surface modification of upconverting NaYF4 nanoparticles with PEG-phosphate ligands for NIR (800 nm) biolabeling within the biological window. *Langmuir : the ACS journal of surfaces and colloids*, *26*(2), 1157-64.

27. Sivakumar, S., Diamente, P. R., & van Veggel, F. C. J. M. (2006). Silica-coated Ln3+-Doped LaF3 nanoparticles as robust down- and upconverting biolabels. *Chemistry (Weinheim an der Bergstrasse, Germany)*, *12*(22), 5878-84.

28. Abdul Jalil, R., & Zhang, Y. (2008). Biocompatibility of silica coated NaYF(4) upconversion fluorescent nanocrystals. *Biomaterials*, *29*(30), 4122-8.

29. Shan, J., Chen, J., Meng, J., Collins, J., Soboyejo, W., Friedberg, J. S., & Ju, Y. (2008). Biofunctionalization, cytotoxicity, and cell uptake of lanthanide doped hydrophobically ligated NaYF[sub 4] upconversion nanophosphors. *Journal of Applied Physics*, *104*(9), 094308.

30. Ptacek, P., Ko, K., & Haase, M. (2007). Lanthanide-Doped NaYF 4 Nanocrystals in Aqueous Solution Displaying Strong Up-Conversion Emission, (24), 1396-1400.

31. Bogdan, N., Vetrone, F., Ozin, G. a, & Capobianco, J. a. (2011). Synthesis of ligand-free colloidally stable water dispersible brightly luminescent lanthanide-doped upconverting nanoparticles. *Nano letters*, *11*(2), 835-40.

32. Rillings, K. W., & Roberts, J. E. (1974). A thermal study of the trifluoroacetates and pentafluoropropionates of praseodymium, samarium, and erbium. *Thermochiica Acta*, *10*, 285-298.

33. Russel, C. (1993). A pyrolytic route to fluoride glasses. I. Preparation and thermal decomposition of metal trifluoroacetates. *Journal of Non-Crystalline Solids*, *152*, 161-166.

34. Zeng, J.-H., Su, J., Li, Z.-H., Yan, R.-X., & Li, Y.-D. (2005). Synthesis and Upconversion Luminescence of Hexagonal-Phase NaYF4:Yb,Er3+ Phosphors of Controlled Size and Morphology. *Advanced Materials*, *17*, 2119-2123.

35. Zhang, Y.-W., Sun, X., Si, R., You, L.-P., & Yan, C.-H. (2005). Single-crystalline and monodisperse LaF3 triangular nanoplates from a single-source precursor. *Journal of the American Chemical Society*, *127*(10), 3260-1.

36. Sivakumar, S., van Veggel, F. C. J. M., & Raudsepp, M. (2005). Bright white light through up-conversion of a single NIR source from sol-gel-derived thin film made with Ln3+-doped LaF3 nanoparticles. *Journal of the American Chemical Society*, *127*(36), 12464-5.

37. Huang, W., Lu, C., Jiang, C., Wang, W., Song, J., Ni, Y., & Xu, Z. (2012). Controlled synthesis of NaYF4 nanoparticles and upconversion properties of NaYF4:Yb, Er (Tm)/FC transparent nanocomposite thin films. *Journal of colloid and interface science*, *376*(1), 34-9. Elsevier Inc.

38. Liu, F., Ma, E., Chen, D., Yu, Y., & Wang, Y. (2006). Tunable red-green upconversion luminescence in novel transparent glass ceramics containing Er: NaYF4 nanocrystals. *The journal of physical chemistry. B*, *110*(42), 20843-6.

39. Si, H.-Y., Yuan, D., Chen, J.-S., Chow, G.-M., & Zhang, H.-L. (2011). Facile patterning of upconversion NaYF4:Yb,Er nanoparticles. *Journal of colloid and interface science*, *353*(2), 569-73.

40. Zhou, H.-P., Zhang, C., & Yan, C.-H. (2009). Controllable assembly of diverse rare-earth nanocrystals via the Langmuir-Blodgett technique and the underlying size- and symmetry-dependent assembly kinetics. *Langmuir : the ACS journal of surfaces and colloids*, *25*(22), 12914-25.

41. Yum, J.-ho, Choi, K.-hyouk, & Sung, Y.-E. (2003). Adhesion Improvement of Phosphor Layer by Combining Electrophoretic Deposition and UV Curing. *Journal of The Electrochemical Society*, *150*(2), H43.

42. Wasserman, S. R., Tao, Y. T., & Whitesides, G. M. (1989). Structure and reactivity of alkylsiloxane monolayers formed by reaction of alkyltrichlorosilanes on silicon substrates. *Langmuir*, *5*(4), 1074-1087.

43. Popat, K. C., Johnson, R. W., & Desai, T. A. (2002). Characterization of vapor deposited thin silane films on silicon substrates for biomedical microdevices, *154*, 253-261.